INAUGURAL - DISSERTATION

zur

Erlangung der Doktorwürde

der

Naturwissenschaftlich-Mathematischen Gesamtfakultät

der

Ruprecht-Karls-Universität

Heidelberg

vorgelegt von

ACHIM FALKENROTH

aus Müllheim

Tag der mündlichen Prüfung: 27. Juli 2007

Visualisierung von
Sauerstoff-Profilen
in der wasserseitigen Grenzschicht

Gutachter:

Prof. Dr. JÜRGEN WOLFRUM
Prof. Dr. BERND JÄHNE

Dissertation
submitted for the degree of Doctor of Natural Sciences to
the Combined Faculties for Natural Sciences and for Mathematics
of the

Ruperto–Carola
University of Heidelberg
Germany

Visualisation of Oxygen Concentration Profiles

in the Aqueous Boundary Layer

presented by
Dipl. Chem. ACHIM FALKENROTH
born in Müllheim

Institute of Environmental Physics
Group: Digital Image Processing and Waves

Referees: day of oral exam: 27. July 2007

Prof. Dr. JÜRGEN WOLFRUM
Prof. Dr. BERND JÄHNE

Abstract

In environment studies as well as for technical application, the study of air–water gas exchange is crucial. For process studies, a novel visualisation technique of oxygen concentrations in water was realised with high spatial resolution. To resolve turbulent processes in water, also the temporal resolution was pushed to the limit of a imaging frame rate of 185 Hz. For this purpose, the well-established method of laser-induced fluorescence (LIF) was extended introducing in this type of studies a new phosphorescent ruthenium dye that is more than 15 times more sensitive to oxygen than the previously used indicator dye. The chemical synthesis of this metal–ligand complex MLC was adapted to a preparation without intermediate steps.

The challenge of this imaging technique for small-scale interactions was to resolve a very thin boundary layer extending less than a millimetre below the water surface. An image processing algorithm was developed that allow the automatic detection of the exact location of the air–water phase boundary within the resolution of 25 µm/pixel. Only by this step, an accurate direct determination of an important parameter for gas-exchange studies, the boundary-layer thickness, is feasible.

The developed methods were applied to systematic gas-transfer measurements mostly with surfactants, conducted in a range of wind speeds between 0.8–7 m/s in a circular wind–wave facility. The measured gas-transfer velocities compared extremely well to exchange rates derived from mass-balance methods. The novel visualisation technique drastically increased the poor signal quality inherent to standard LIF techniques. This enabled accurate measurements of gas-transfer velocities from aqueous concentration profiles for the first time.

Kurzfassung (German)

In den Umweltwissenschaften ebenso wie in technischen Anwendungen ist die Untersuchung des Gasaustausches grundlegend. Für mechanistische Studien wurde eine neuartige Visualisierungstechnik für Sauerstoffkonzentrationen in Wasser mit einer hohen räumlichen Auflösung realisiert. Um turbulente Prozesse im Wasser sichtbar zu machen, wurde eine Bildrate am Limit der zeitliche Auflösung von 185 Hz verwendet. Für diesen Zweck, wurde die bereits etablierte Methode der Laser induzierten Fluoreszenz (LIF) erweitert und ein neuer phosphoreszenter Farbstoff verwendet, der eine mehr als 15-fach stärkere Sauerstoffempfindlichkeit aufwies verglichen mit dem zuvor verwendeten Farbstoff. Die chemische Synthese des Farbstoffs wurde auf eine Darstellung ohne Aufarbeitung angepasst.

Die Herausforderung dieses bildgebenden Verfahrens für kleinskalige Wechselwirkungen ist, eine sehr dünne Grenzschicht aufzulösen, die sich weniger als einen Millimeter unter die Wasseroberfläche erstreckt. Ein Bildverarbeitungsalgorithmus wurde entwickelt, der eine automatische Erkennung der exakten Position der Luft–Wasser-Phasengrenze innerhalb der Auflösung von 25 µm/Pixel erlaubt. Dieser Schritt ermöglicht die genaue Bestimmung eines wichtigen Parameters von Gasaustauschstudien, die Grenzschichtdicke.

Die entwickelten Methoden wurden auf gezielte Gasaustauschmessungen vornehmlich mit einem Oberflächenfilm angewendet, die mit Windstärken zwischen 0.8–7 m/s in einem zirkulären Wind–Wellen-Kanal durchgeführt wurden. Die gemessenen Gas-Transfergeschwindigkeiten stimmten äußerst gut mit Austauschraten überein, die aus Massenbilanzverfahren bestimmt wurden. Die neue Visualisierungstechnik erhöhte die Signalqualität von Standard-LIF-Techniken drastisch. Dies ermöglichte erstmals genaue Messungen der Gas-Transfergeschwindigkeiten aus wasserseitigen Konzentrationsfeldern.

Table of Contents

Part I

Introduction and Theory

Chapter 1

Introducing the Topic

1.1   Motivation: Fields of Application

Exchange processes between air and water play an important role in natural environments and technical applications. Their study can deepen our understanding of fundamental physics of turbulent processes in fluid dynamics.

The efficient transfer of chemical species between a gas phase and a liquid phase is optimised in industrial plants using falling films, spray chambers or bubble columns. Substances are absorbed by solvents or stripped from them. Facilities extract H_2S from water to improve the quality of drinking water. The treatment of water form sources near the soil surface include the stripping of carbonic acid in gas-exchange installations. The aeration of waste water is essential in the biological treatment where micro-organisms decompose undesired contents in sewage. The re-aeration of lakes and rivers across the water surface is a critical process for the ecology of these environments, especially if they show high biological activity.

Gas transfer between the atmosphere and the oceans is an important actor in the theatre of global climate change. Due to the use of fossil hydrocarbons as a source of energy, the concentration of the important greenhouse gas in the atmosphere carbon dioxide CO_2 increased from a pre-industrial value of about 280 ppm to 383 ppm in 2007 as seen in Fig. 1.1. The actual annual increase is about 1.9 ppm as a mean of the last decade.

The International Panel on Climate Change (IPCC [2007]) reports that the present atmospheric concentration of carbon dioxide exceeds by far the natural range over the last 650,000 years (180–300 ppm) as determined from ice cores. Nobody seriously doubts that the increase of carbon dioxide in the atmosphere is caused by anthropogenic fossil fuel consumption.

The oceans are capable of storing atmospheric gases. A considerable sink of these gases are deep water formations. An estimation by SIEGENTHALER

Atmospheric CO₂ at Mauna Loa Observatory
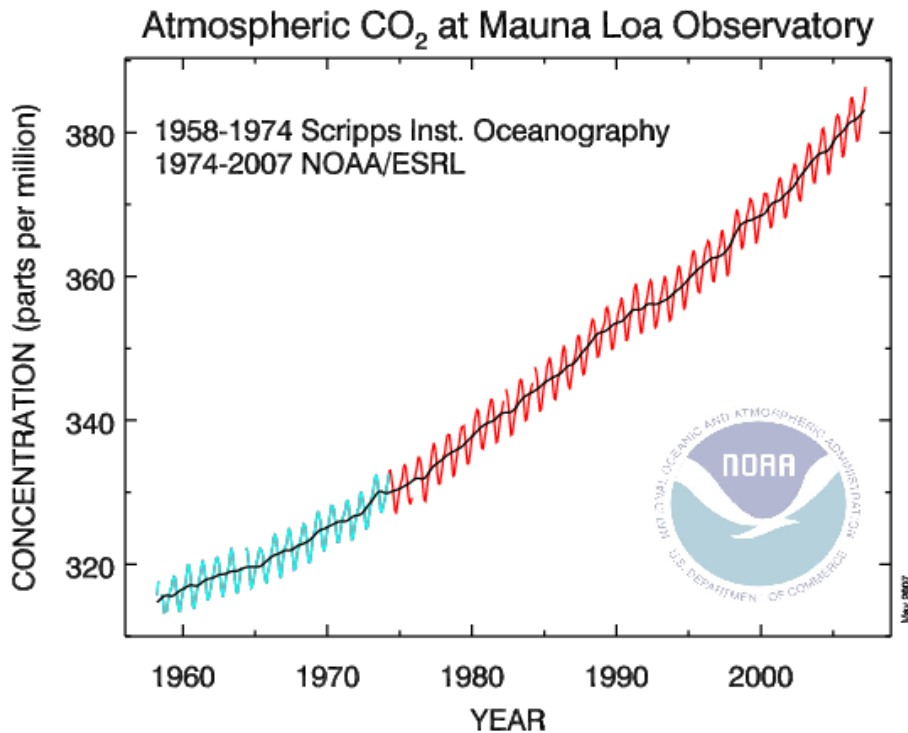
Figure 1.1: Measured concentration increase of CO_2 in the atmosphere during the last 50 years. This curve is named after C.D. Keeling. The mean concentration increases continuously. The periodical variation of the concentration is due to seasonal biological activity (Courtesy of Dr. P. Tans, NOAA/ESRL, www.esrl.noaa.gov/gmd/ccgg/trends)

and SARMIENTO [1993] assumes that the uptake of CO_2 by the oceans is about a third of the anthropogenic emission.

Oxygen can be used as an environment tracer to determine the extend of the role of the ocean as a sink. The burning of hydrocarbons consumes atmospheric oxygen. When carbon dioxide is transformed into biomass, oxygen is released again. By taking the difference of the expected atmospheric N_2/O_2 ratio after the consumption of the known amount of fossil fuels in the last years and the actual oxygen concentration found in the atmosphere, the part that ended up in the oceans can be calculated to be approximately 30% as documented by the IPCC [2001]. Sensitive measurements were carried out by KEELING et al. [1996] and MANNING [2001] and taken as a basis for global gas-exchange modelling by e.g. KEELING et al. [1998].

The enhancement of air–water gas exchange by waves is striking. Several authors (WANNINKHOF [1992], NAEGLER et al. [2006], HO et al. [2006b] to cite only a few) introduced different parametrisation of the gas-transfer velocity with the wind speed with significant uncertainties regarding the measured data and the underlying theoretical assumptions.

TAKAHASHI et al. [2002] assembled a world map of approximate local CO_2 fluxes through the ocean surface. A version that was included in the IPCC report [2007] is shown in Fig. 1.2. In the annual mean, the warm tropospheric regions of the ocean act as a source of CO_2 whereas sinks are found in polar regions. This is because the solubility of this gas decreases with higher water temperature. The locally resolved information for this map are temperature informations and the estimation of the wind speed computed from satellite microwave backscattering. The latter is a measure of the sea-surface roughness. On his web site referenced in the bibliography, TAKAHASHI et al. states that estimated fluxes change by 30% when the wind speed is computed from two different parametrisations. Similar uncertainties are expected when the assumed dependence of the gas-exchange rate from wind is changed.

The IPCC [2007] comments Fig. 1.2: "The annual flux of CO_2 for 1995 with 10 m winds is –1.6 GtC/yr, with an approximate uncertainty of ± 1 GtC/yr, mainly due to uncertainty in the gas-exchange velocity and limited data coverage." The quadratic relation between wind speed and gas-transfer velocity proposed by WANNINKHOF [1992] was taken to calculate the exchange rate. The factor of proportionality in this parametrisation is not well known. Moreover, also a cubic [WANNINKHOF and MCGILLIS, 1999] or linear [KRAKAUER et al., 2006] dependence has been proposed.
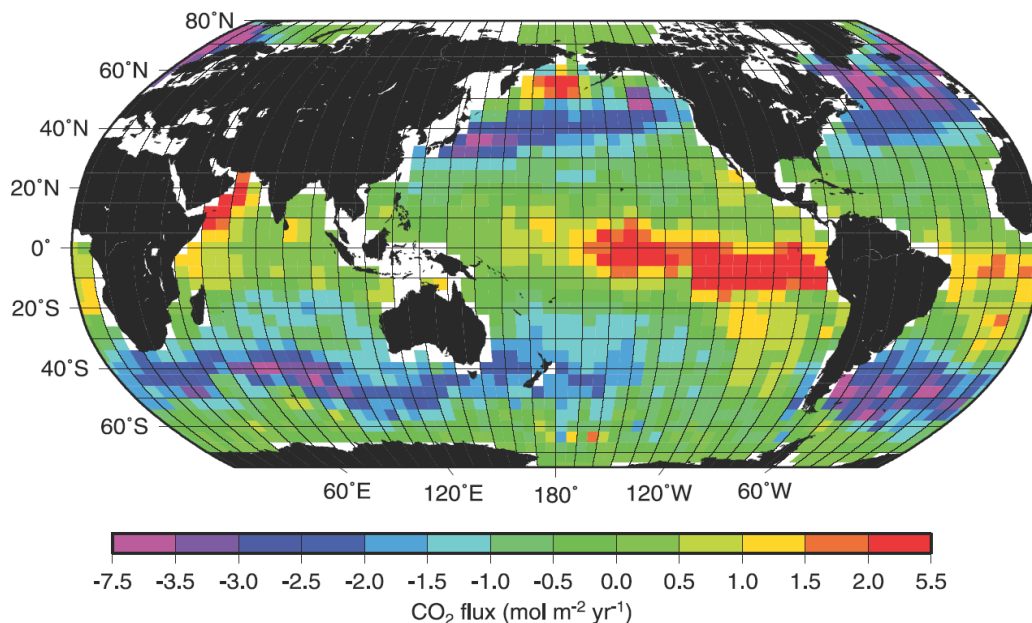

Figure 1.2: World map of global mean sea-to-air flux of CO_2. A significant part of the large error in this modelling is due to the uncertain behaviour of the gas-exchange velocity (From IPCC [2007])

Wanninkhof [2007] demonstrated that the gas transfer from the atmosphere into the ocean is one bottleneck besides the slow transport of gases into deep water. He demonstrated that the influence of gas exchange variables is decisive for the results of global climate models. The improvement of the reliability of these models is important to convince policy makers of the need to change the employment of energy.

The interaction between ocean and the atmosphere is complex as summarised graphically in Fig. 1.3. Besides the exchange of heat and momentum, the transfer of chemical species takes a central part in this system. A profound knowledge of mechanisms in this system and its interdependencies is the basis of understanding influences on effects such as climate change. The surface ocean lower atmosphere study (SOLAS) tries to link the different aspects of air–sea interaction.

Waves amplify the gas exchange but they can be generated by light winds only if the surface is clean and free of any kind of surface active substances. A special case in the system shown in Fig. 1.3 is the gas transfer through the air–sea interface covered by a surface film. Surfactants decrease the surface tension and the different parts of the surface are hindered in their mobility. This has a strong impact on the hydro dynamics in the boundary layer, effectively damping waves and suppressing turbulences close to the interface. This leads the focus on natural surfactants having a considerable influence on air–sea interactions [Frew et al., 1990].

All these uncertainties demonstrate the need for a more substantial knowledge about small-scale processes. The gas exchange between the atmosphere and the ocean is controlled by a thin sub-millimetre aqueous boundary layer. Because of limited experimental techniques, the details of the mechanisms and the structure of the turbulence near the phase boundary are not studied enough. Meanwhile some new well-engineered imaging techniques are matured that give direct insight into the transfer processes and promise fundamental progress. Some of these techniques will be documented in the following.

1.2   Aims and Corresponding Methods

The objectives of this study are:

● *Visualisation of concentrations in water.* Concentration fields are visualised in water by applying the idea of laser-induced fluorescence LIF. Indicator dyes are sensitive to dissolved gases and the intensity of luminescent emission varies with the concentration. A fast digital camera with 640×480 pixel and a resolution of 25 µm/pixel looks at a laser-light sheet with a frame rate of
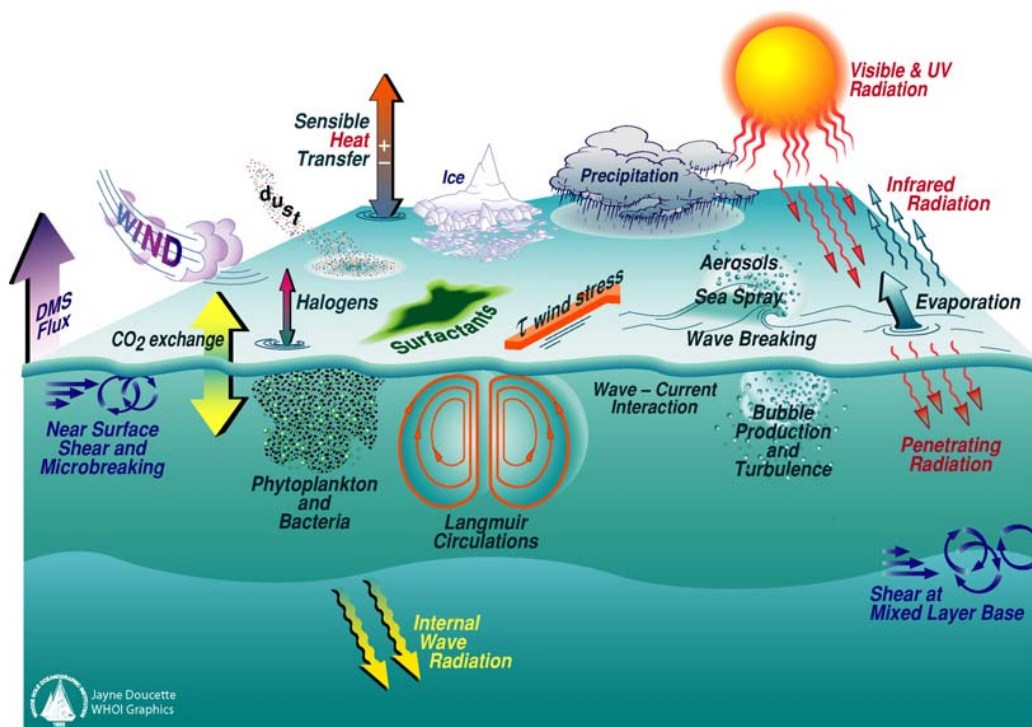
Figure 1.3: The forms of interaction between the ocean and the atmosphere are manifold. The SOLAS programme coordinates research on these very different topics that are depicted in the chart (From [SOLAS])

185 Hz. A high imaging rate is important to resolve the turbulence processes. After calibration the concentration is calculated from the light emitted by the luminescent dye at every location.

- *LIF with a novel class of phosphorescent dyes.* The established oxygen indicator, a pyrene derivative, has some drawbacks, e.g. the low sensitivity and small quantum yield. These lead to a poor signal-to-noise ratio. A type of ruthenium metal–ligand complexes MLC shows better properties regarding the requirements of LIF applications in water. Oxygen quenches efficiently the phosphorescence of this dye. As the quenching process is fast compared to mass fluxes, the concentration of the quencher O_2 is evaluated reliably at any point.

- *Study of concentration fields in gas-exchange experiments.* In laboratory experiments the gas exchange is studied under a range of different reproducible conditions. In a wind–wave facility of the Aeolotron laboratory at the University of Heidelberg, these conditions are fully controllable. The wind speed can be varied accurately in the range between 0.8–7 m/s. A surfactant film on the water surface suppresses the generation of wind waves even at high shear stress. A disequilibrium of concentration induces a invasion flux of oxygen from ambient air into the degassed water bulk across the

air–water interface.

• *Extraction of concentration profiles.* The difficulty in studying the mechanisms of air–water gas exchange is due to the small thickness (30–800 µm) of the aqueous mass-boundary layer at a free interface. This thin skin of the water body dominates the gas exchange through the surface. Accurate measurements of the intensity profile near the phase boundary are a premise for a further analysis. By image processing steps the surface position is detected in every image row for image registration. Further evaluations produce a mean concentration profile for the determination of the boundary-layer thickness.

• *Comparison of calculated transfer velocities with reference measurements.* The boundary-layer thickness of every concentration profile depends on the gas flux at this position. The computed transfer velocity is compared with mean gas-exchange rates of trace gases at the same wind conditions. They are measured simultaneously with a mass-balance method during the evasion of these gases.

• *Comparison of the profile shape with model predictions.* Theoretical models predict the concentration profile based on hydrodynamic assumptions for certain conditions. They express the physical mechanism of turbulent transport across the diffusive boundary layer. Different gas-exchange concepts introduced in Sec. 2.2 cohabit in the literature. Classical mass-balance methods can not distinguish between the different theoretical concepts considering that they measure the mean flux averaged over the whole interface. Only techniques that visualise localised concentration fields of the dissolved gases give direct insight into the turbulence close to the phase boundary because the descriptions differ significantly only in the concentration distribution within this thin layer. The comparison of the shape of the theoretical profiles with the measured data reveal the dominant mechanism for the selected condition.

1.3   Outline of this Thesis

In a first part, the characteristic quantities are defined and the fundamental concepts of gas exchange are discussed in Chap. 2. Here the theoretical description of the mean concentration profile in the mass-boundary layer are developed.

For laser-induced fluorescence, a suitable dye is needed and thus a ruthenium complex is presented and characterised in the next part in Chap. 3. Fundamentals of luminescence and its quenching are introduced aside specific absorption and emission spectra of the phosphorescent luminophore. Also the chemical synthesis of the organo-metallic compound is described.

Gas-exchange experiments were carried out in a water flume under a range of different wind speed conditions. The equipment is illustrated in Chap. 4. The properties of the instrumentation and of the optical set-up are explained. The need of resolving areas in the scale of $100\,\mu\text{m}$ in the water leads to an optical blurring of the images. The influence of this blurring on the final measurement is detailed in this chapter.

To extract concentration profiles and measurable gas-exchange parameters from grey-value image sequences, some steps of image processing are needed that are the subject of Chap. 5. For the calculation of the boundary-layer thickness, two approaches will be described, a commonly used method of extrapolation of the highest gradient and a newly developed method considering the blurring in a model function.

In Chap. 6 the results are exposed and the good performance of the novel imaging technique is demonstrated. Concentration profiles are compared to the theoretical ones, and gas transfer velocities are shown together with reference measurements from a mass-balance method. The behaviour of the concentration field in different gas-exchange experiments with varying conditions is presented. The findings in experiments with a smooth surface are analysed. A side product was the generation of bulk turbulence that could be analysed with the same techniques as the data measured under wind stress.

Finally the results are evaluated and summarised in Chap. 7. At the end, a summary of this work is found in Chap. 8 where also an outlook on further studies and future research is suggested.

Chapter 2

Theory and Literature Review: Gas Exchange on Small Scales

In this chapter the basic relationships of physical parameters and properties are presented that describe the gas transfer through the interface between air and water. In general, the transfer between two phases is driven by a difference of any transportable physical quantity such as gases, momentum or heat. Nonetheless, the description will be limited here to the exchange processes of gases.

2.1 Characteristic Quantities of Gas Exchange

When gases are transferred from the air into the water or vice versa, the mass flux through the surface area A defines a flux density j that can be determined by monitoring the development of the concentration with time in a water volume V assuming that the concentration change is only due to gas exchange and not to chemical reaction:

$$j = \frac{1}{A}\frac{\mathrm{d}m}{\mathrm{d}t} = \frac{V}{A}\frac{\mathrm{d}c}{\mathrm{d}t} \tag{2.1}$$

In the case of equilibrium the mass flux from one phase into the other is as high as in the inverse direction so that the net flux and the concentration gradient is zero. Thus, Eq. 2.1 defines the net flux j. Generally a flux of gases in both directions is characterised by the transfer velocity k. The transfer velocity is defined as the constant of proportionality between the mass flux density j and the difference in concentration Δc across the aqueous boundary layer.

$$j = k\Delta c \tag{2.2}$$

The transfer velocity k is also called the piston velocity. This quantity can be taken as the velocity of an imaginary syringe piston that presses the concentration into the water.

The solubility of a substance is usually not the same in both phases. Thus, the concentrations reach an equilibrium with a certain concentration difference at the interface. To correct for this, one of the concentrations can be scaled by the OSTWALD solubility α. With this the flux through an interface is:

$$j = k(c_{\mathrm{bulk}} - \alpha c_{\mathrm{air}})$$

with the dimensionless solubility

$$\alpha = c_{\mathrm{eq,bulk}}/c_{\mathrm{eq,air}}$$

One way to determine αc_{air} in an experiment where $c_{\mathrm{air}} = c_{\mathrm{eq,air}}$ is kept constant is to measure the concentration in the water bulk c_{bulk} in the state of equilibrium. It is advantageous to use the same measurement technique for determining c_{bulk} and αc_{air} because some errors of the measurement cancel out and an additional uncertainty from the value of solubility is avoided.

The underlying assumption is that the water concentration directly at the surface is always in equilibrium with the air concentration. This is to say that the solving process for the transition between the phases is sufficiently fast compared to the mass transport near the interface by mere diffusion to neglect the influence on these equations. This implies also that there is no resistance to mass transfer in the air.

Combining Eq. 2.1 with Eq. 2.2 yields the mass-balance method for measuring the transfer velocity k with the knowledge of the mixing height $h = V/A$:

$$h\frac{\mathrm{d}c}{\mathrm{d}t} = k\Delta c \tag{2.3}$$

The flux density $\vec{j}$ due to diffusion can be calculated from the gradient of concentration by FICK's law and is caused by random thermal motion of the particles:

$$\vec{j} = -D\vec{\nabla}c \tag{2.4}$$

The factor D is called diffusivity and has the common units of $[\mathrm{cm/s}^2]$. This diffusion constant is a specific quantity of a substance in a given medium. For all gases the diffusivity is much higher in air than in water. This is also a reason why for most gases the resistance to mass transfer in air can

be neglected compared to the resistance in water. For our application the diffusivity of oxygen in water is important. The temperature dependence is given by MAYER [1995] from data in JÄHNE [1980].

The minus sign in Eq. 2.4 reflects the observation that mass flux is in the direction towards lower concentration. At the interface this relation holds also in presence of turbulence, given that here the vertical mass flux is only due to diffusion because the surface can not be penetrated by flows or eddies. Thus, j_z can be taken from the gradient of concentration at the surface that forces the gas into the bulk of the water. In this text the coordinate z is the depth from the water surface.

The gradient of the concentration c can change in time t due to the mass transport by diffusion or by transport in streams with the velocity $\vec{u}$ of the fluid. The resulting relation is called FICK's 2nd law:

$$\frac{dc}{dt} = \frac{\partial c}{\partial t} + \vec{u}\,\vec{\nabla}c = -\vec{\nabla}\vec{j} = D\vec{\nabla}^2 c \qquad (2.5)$$

Therefore, also the transfer velocity k depends on the diffusivity D of the transported species. If the transfer velocities of different gases A and B are compared under the same conditions, a relation between them is revealed [e.g. in JÄHNE, 1980]:

$$k \propto D^{+n} \Rightarrow \frac{k_A}{k_B} = \frac{D_A^{+n}}{D_B^{+n}} = \frac{Sc_A^{-n}}{Sc_B^{-n}} \quad \text{with} \quad Sc_i = \frac{\nu}{D_i} \qquad (2.6)$$

The SCHMIDT number Sc was introduced in the literature to describe the relation of diffusivity to the momentum transport expressed in the quantity of the kinematic viscosity of water $\nu = \mu/\varrho$ where μ is the dynamic viscosity and ϱ is the density of the medium. For gases dissolved in water the dimensionless SCHMIDT-number ranges between 100–2000. The SCHMIDT-number exponent n depends on the forcing conditions of the gas exchange. For wind driven gas exchange it was shown that the exponent is $^2/_3$ for a smooth rigid interface and $^1/_2$ for the free surface [JÄHNE and HAUSSECKER, 1998; DEGREIF, 2006].

In field studies the development of the single concentrations are not as easily accessible as other quantities. A parametrisation for the gas exchange with these parameters is needed. In most ocean gas-exchange studies the wind speed u_{10} in the height of $10\,m$ above the water surface is used as a parameter [WANNINKHOF, 1992; NAEGLER et al., 2006]. The relation adopts the following form:

$$k = \frac{Sc^{-n}}{\beta}\,u_{10}{}^\chi \qquad (2.7)$$

The coefficient β is estimated empirically with a high variability by measuring tracer gases like He and SF_6 [HO et al., 2006a; McGILLIS et al., 2001;

Nightingale et al., 2000]. Mostly a quadratic dependence ($\chi = 2$) from wind speed is assumed but also cubic [Wanninkhof and McGillis, 1999] or linear [Krakauer et al., 2006] dependencies are found.

A parameter, that takes the condition like surfactants or roughness of the water surface into account, is the mean wave slope $\bar{\sigma}_\mathrm{w}$ [Jähne, 1985; Degreif, 2006]. In global modelling the wind fields are taken as a parameter and they are computed from a measure of the surface roughness determined by satellites via radar backscattering. The friction velocity $u_\star$ as a measurable quantity includes more influences on momentum transfer from wind into water.

To characterise the gas exchange, some other quantities are important in this work. Dividing the diffusivity D by the transfer velocity k, a quantity $z_\star$ with the unity of a distance is calculated that is called boundary-layer thickness. Using Eq. 2.2 and Eq. 2.4 this spatial scale is geometrically given as the interception of the vertical gradient of the concentration at the surface with the bulk concentration level as seen in Fig. 2.1:

$$z_\star = \frac{D}{k} = D\frac{\Delta c}{j_z} = \frac{\Delta c}{-\frac{\partial c}{\partial z}\big|_{z=0}} \tag{2.8}$$
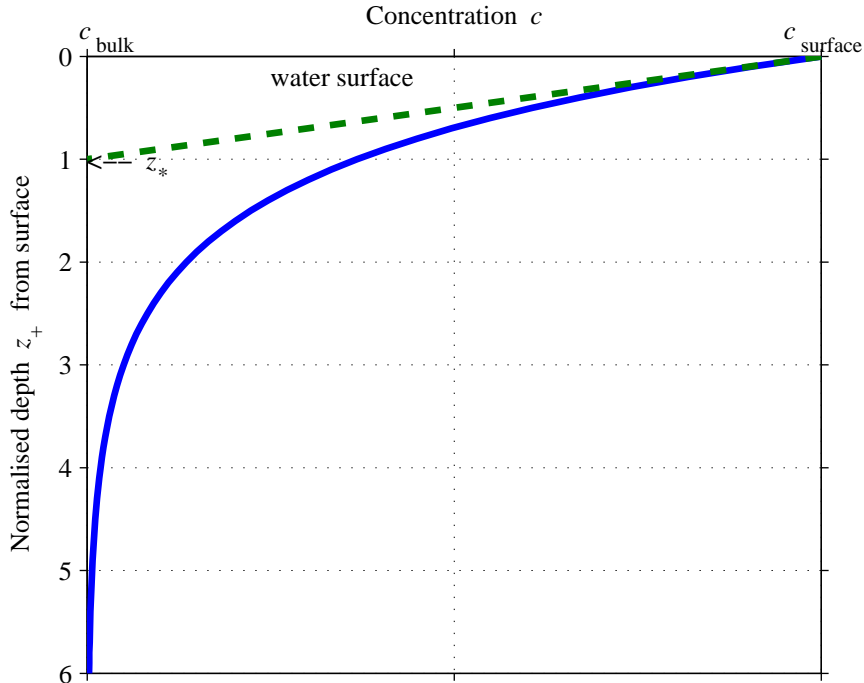

Figure 2.1: Definition of the boundary-layer thickness $z_\star$ in a concentration profile $c(z_+)$ (*solid line*) derived from the gradient of the concentration $\partial c/\partial z_+$ at the surface $z_+ = 0$ (*broken line*) with $z_+ = z/z_\star$

The sole assumption for this is that at the water surface the molecular diffusion is the only process driving the balancing of the gas concentrations towards the equilibrium. All the transport by flows and eddies is dumped by viscosity and buoyancy near the interface.

Another quantity is derived by the ratio of $z_\star$ and k giving the time scale $t_\star$ of the gas-exchange process. This is the time that is needed for a particle to pass through a distance $z_\star$ driven by molecular diffusion. Using Eq. 2.8 makes clear that only one of the three parameters $t_\star, z_\star$ or k is needed to characterise the gas exchange:

$$t_\star = \frac{z_\star}{k} = \frac{D}{k^2} \tag{2.9}$$

The value of this number can be given by taking typical values of the transfer velocity $k = 3.6\,\mathrm{cm/h} = 10^{-3}\,\mathrm{cm/s}$ and the diffusion coefficient of oxygen in water $D = 2.4\ 10^{-5}\,\mathrm{cm^2/s}$ at 25°C.

$$z_\star = \frac{D}{k} = 0.24\,\mathrm{mm}$$
$$t_\star = \frac{z_\star}{k} = 24\,\mathrm{s}$$

In this work the boundary-layer thickness $z_\star$ is the key parameter to measure. Even with the knowledge of the profile close to the surface, the value of $z_\star$ can not be measured as a distance for all cases because it depends on the transport process below the surface and thus from the turbulence structure.

Diffusion is dominating only near the surface. In the case that no mean flow exists close to the surface, only turbulence adds to the diffusion. The character of the turbulence alters the form of the vertical concentration profile and with this the level of concentration where $z_\star$ is reached. In the next section different models are summarised describing the mechanism of transport that add to the diffusion.

2.2 Conceptual Description of Gas Exchange

With increasing distance from the surface, turbulence adds to the molecular diffusion as a mass-transport mechanism. There are different theories about the description of the turbulence processes. They all yield in different concentration profiles in the boundary layer that can be visualised with the presented LIF technique.

2.2.1   Stagnant Film Model

A very simplistic model is the model that assumes only diffusion up to a certain distance from the surface and at a certain point the turbulence is the only gas transporting force. To adapt this stagnant film model, first published by LEWIS and WHITMAN [1924], to a given transfer velocity, the diffusion layer thickness can be adjusted and is the same as $z_\star$. For the concentration profile this model predicts a linear line like the *broken line* in Fig. 2.1. In this model, the SCHMIDT-number exponent is $n = 1$.

$$k \propto \mathrm{Sc}^{-1} \tag{2.10}$$

The idea of a sudden change from diffusion to turbulence at a certain depth is not physically reasonable and the implication of the dependence of the gas exchange rate from the SCHMIDT-number exponent of $n = 1$ is not found in gas-exchange experiments. As it underestimates the transfer velocity k, the value calculated using this simple model can be taken as a lower limit.

2.2.2 K-Model

Turbulence eddies can not penetrate the surface and only diffusion is present exactly at the surface. In this picture the eddy size has to decrease towards the surface. This is why the model is also called small-eddy model. This effect happens everywhere and is statistically independent from time. This means that a turbulence effect is simply added to the molecular diffusion but increases with depth from zero to get dominant beyond the boundary layer. The diffusivity is now the sum of the molecular diffusion coefficient D and a turbulent diffusion coefficient K_t that gave this concept also the name K-model. Considering the turbulence in Eq. 2.5 with Eq. 2.4 yields:

$$\frac{\partial \bar{c}(t, z)}{\partial t} = \frac{\partial}{\partial z}\left((D + K_\mathrm{t}(z)) \frac{\partial \bar{c}(t, z)}{\partial z} \right) \tag{2.11}$$

The characterisation of the turbulence structure by a turbulent diffusivity K_t includes some temporal or spatial averaging and describes the mean concentration profiles $\bar{c}(t, z)$.

COANTIC [1986] deduces a cubic relationship between the turbulent diffusivity and the depth for a smooth rigid wall using some assumptions about a limited mobility of the surface water. For a free surface he yielded an increase as a square of the distance to the interface and COANTIC cited some authors [DAVIES, 1972; BRUTSAERT and JIRKA, 1984] that observed this increase.

The concentration depth profile can be computed from the differential equation if the depth dependence of the turbulent diffusivity K_t is expressed according to a power law in the way JÄHNE et al. [1989] did:

$$K_t(z) \;=\; \alpha_m\, z^m \quad \text{with} \ \ m \geqslant 2 \tag{2.12}$$

In the case of stationary conditions the concentration does not change with time t, and the partial derivatives of Eq. 2.11 become an ordinary differential quotient:

$$0 \;=\; \frac{\mathrm{d}}{\mathrm{d}z_+}\left((1 + \alpha_{m+}\, z_+{}^m)\, \frac{\mathrm{d}\bar{c}(z_+)}{\mathrm{d}z_+} \right) \tag{2.13}$$

In the latter equation a transition to dimensionless variables was made where the variables are scaled by constants describing the flux:

$$z_+ = \frac{z}{z_\star} \quad \text{and} \ \ \alpha_{m+} = \frac{\alpha_m\, z_\star{}^m}{D} \tag{2.14}$$

The second-order ordinary differential equation in Eq. 2.13 can be solved by substitution of $\mathrm{d}\bar{c}/\mathrm{d}z_+ := y$. The resulting first order differential equation is solved by separation of the variable and integration:

$$\frac{\mathrm{d}y(z_+)}{\mathrm{d}z_+} \;=\; -\frac{\alpha_{m+}\, m\, z_+{}^{m-1}}{1 + \alpha_{m+}\, z_+{}^m}\, y(z_+) \tag{2.15}$$

$$\int \frac{1}{y}\mathrm{d}y \;=\; -\int \frac{\alpha_{m+}\, m\, z_+{}^{m-1}}{1 + \alpha_{m+}\, z_+{}^m}\, \mathrm{d}z_+$$

$$\ln(y(z_+)) \;=\; -\ln(1 + \alpha_{m+}\, z_+{}^m) + \check{c}2$$

$$\Rightarrow y(z_+) \;=\; \frac{c2}{1 + \alpha_{m+}\, z_+{}^m} \tag{2.16}$$

The function ln denominates the natural logarithm. The integration constant $c2 = \exp(\check{c}2) = -1$ can be given under consideration of the boundary condition $y(0) = \mathrm{d}\bar{c}/\mathrm{d}z_+|_{z_+=0} = -1$ what is the one dimensional FICK's law of Eq. 2.4 in the dimensionless version with the assumption that molecular diffusion is the only transport process at the surface.

Inverting the substitution, the depth dependent function of the concentration $\bar{c}(z_+)$ is found:

$$\bar{c}(z_+) \;=\; \int y(z_+)\,\mathrm{d}z_+ = c1 - \int_0^{z_+} \frac{1}{1 + \alpha_{m+}\, \check{z}_+{}^m}\, \mathrm{d}\check{z}_+ \tag{2.17}$$
$$\text{with} \ \ m > 0$$

Again the integration constant $c1 = 1$ is determined by a boundary condition: $\bar{c}(0) = 1$. According to the definition of the relative concentration $\bar{c}$

between 0–1, this concentration has to vanish at large distances. Using this boundary condition, an expression for α_{m+} can be given:

$$\lim_{z_+ \to \infty} \bar{c}(z_+) = 1 - \int_0^\infty \frac{1}{1 + \alpha_{m+} \; \check{z}_+{}^m} \, d\check{z}_+ = 0 \tag{2.18}$$

$$\Rightarrow \alpha_{m+} = \left(\int_0^\infty \frac{1}{1 + \check{z}_+{}^m} \, d\check{z}_+ \right)^m = \left(\frac{\pi}{m \sin(\pi/m)} \right)^m \tag{2.19}$$

$$\text{with } \; m \in \mathbb{N} > 1$$

For the special cases of a free surface ($m = 2$) and a smooth rigid wall ($m = 3$ or 4), specific functions can be written as:

$$m = 2 \Rightarrow \; \bar{c}(z_+) = \; 1 - \frac{\pi}{2} \arctan\left(\frac{\pi}{2} z_+ \right) = \frac{\pi}{2} \operatorname{arccot}\left(\frac{\pi}{2} z_+ \right) \tag{2.20}$$

$$\text{with } \; \alpha_{2+} = \frac{\pi^2}{4}$$

$$m = 3 \Rightarrow \; \bar{c}(z_+) = \; \frac{3}{4} + \frac{3}{2\pi} \arctan\left(\frac{1}{\sqrt{3}} - \frac{4\pi}{9} z_+ \right) - \frac{\sqrt{3}}{2\pi} \ln\left(9 + 2\sqrt{3}\pi z_+ \right)$$

$$+ \frac{\sqrt{3}}{4\pi} \ln\left(81 - 18\sqrt{3}\pi z_+ + 12\pi^2 \, z_+{}^2 \right) \tag{2.21}$$

$$\text{with } \; \alpha_{3+} = \frac{8\pi^3}{81\sqrt{3}}$$

$$m = 4 \Rightarrow \; \bar{c}(z_+) = \; 1 + \frac{1}{\pi} \arctan\left(1 - \frac{\pi}{2} z_+ \right) - \frac{1}{\pi} \arctan\left(1 + \frac{\pi}{2} z_+ \right) \tag{2.22}$$

$$+ \frac{1}{2\pi} \ln\left(8 - 4\pi z_+ + \pi^2 z_+{}^2 \right) - \frac{1}{2\pi} \ln\left(8 + 4\pi z_+ + \pi^2 z_+{}^2 \right)$$

$$\text{with } \; \alpha_{4+} = \frac{\pi^4}{64}$$

For $m = 2$ or 3 this is a similar result as found by MÜNSTERER [1996]. A detailed derivation of these equations using the algebra programme Mathematica can be found in Appendix B. The transformation in Eq. 2.20 from $\arctan(x)$ to $\operatorname{arccot}(x)$ has to be treated with caution because different definition ranges for x are encountered leading to different results for $x \leqslant 0$. The corresponding graphs are shown in Fig. 2.2 where the normalised concentration c_+ is defined between the concentration at the surface c_{surface} and the bulk concentration c_{bulk}.

$$c_+ = \frac{c - c_{\text{bulk}}}{c_{\text{surface}} - c_{\text{bulk}}} \tag{2.23}$$

With increasing m, K_t decreases for values lower than $z = z_\star$ or $z_+ = 1$, and K_t gets more and more dominant for values $z \geqslant z_\star$. Hence, with increasing m, the curves approach the linear curve predicted by the stagnant film model. The SCHMIDT-number exponent n was derived theoretically by
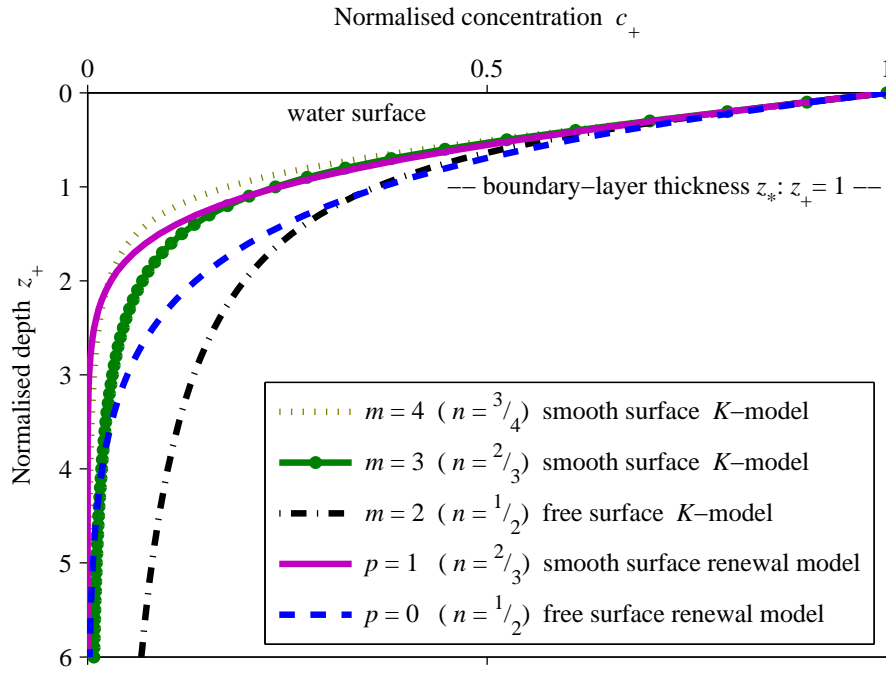
Figure 2.2: Model functions for the cases of a free surface and a smooth rigid surface assuming the K-model (= small-eddy model) or the surface-renewal model

COANTIC [1986] as $n = \frac{2}{3}$ and $\frac{1}{2}$ for a smooth rigid surface ($m = 3$) and a free surface ($m = 2$) respectively. This leads to the relation with m of the power law of Eq. 2.12 as:

$$n = 1 - \frac{1}{m} \tag{2.24}$$

The third mentioned possibility in Eq. 2.22 is $m = 4$ what makes $n = \frac{3}{4}$. There are experiments like in a convection tank in JÄHNE [1980] that suggest such a SCHIMDT number dependence.

2.2.3 Surface-Renewal Model

DANCKWERTS [1951, 1970] proposed an event based model in which large eddies dominate the transport. These eddies reach the phase boundary replacing the surface water with bulk water. Simultaneously they drag the surface water with concentrations that are in equilibrium with the air phase, deeper in the water bulk. A modelling parameter here is the time constant of the renewal rate. DANCKWERTS used the mathematical formulation that HIGBIE [1935] developed to describe the gas exchange in a stage column. In this film column a periodicity was given by the distance of the stages. In

Higbie's set-up it was not turbulence that renewed a surface but the water was exposed only for a certain time to the air.

In analogy, Danckwerts claimed that the different patches of the surface are exposed to the air for a certain time before they are renewed statistically in events with a renewal rate λ characteristic for the gas-exchange conditions. These events are called sometimes large eddies giving this name also to the model. Using this assumption, Eq. 2.5 can be extended by a renewal term in the following form:

$$\frac{\partial \bar{c}(t, z)}{\partial t} \;=\; D\frac{\partial^2}{\partial z^2}\,\bar{c}(t, z) - \lambda(z)\,\bar{c} \tag{2.25}$$

Again, for stationary conditions this equation can be solved as an ordinary differential equation. In the dimensionless form the solution is quite obvious considering the boundary conditions:

$$0 \;=\; \frac{\mathrm{d}^2}{\mathrm{d}z_+{}^2}\,\bar{c}(z_+) - \lambda_+\,\bar{c}(z_+) \;\;\text{with}\;\; \lambda_+ = \lambda\,t_\star \tag{2.26}$$

$$\bar{c}(0) = 1 \;\;\text{and}\;\; \left.\frac{\mathrm{d}\bar{c}(z_+)}{\mathrm{d}z_+}\right|_{z_+=0} = -1 \;\;\text{and}\;\; \lim_{z_+\to\infty}\bar{c}(z_+) = 0 \;\;\Rightarrow\;\; \lambda_+ = 1$$

$$\Rightarrow\;\; \bar{c}(z_+) \;=\; \mathrm{e}^{-z_+} \tag{2.27}$$

So the boundary condition $\lim_{z_+\to\infty}\bar{c}(z_+) = 0$ confines the renewal rate λ to be the inverse of the time constant $t_\star{}^{-1}$ defined in Eq. 2.9. For comparison the exponential function is also plotted in Fig. 2.2.

Harriott [1962] stated that the eddies can not reach the surface but they can come very close to it. This satisfies the hydrodynamic condition that only molecular diffusion is present at the surface. This is especially the case for smooth rigid surfaces. In this penetration model the distance of the eddies from the surface is another parameter for the gas transfer velocity. The closer the surface gets the fewer eddies reach that distance. Gulliver [1991] framed this concept in a conceptual sketch of the size of $z_\star$ depending on the renewal eddies as displayed in Fig. 2.3.

In analogy to Eq. 2.12 the depth dependence of λ is assumed as a general power law as it was done by Jähne et al. [1989]:

$$\lambda \;=\; \gamma_p\,z^p \;\;\text{with}\;\; p \geqslant 0 \tag{2.28}$$

In this equation the classical view of Danckwerts [1970] is represented by the case of $p = 0$ where the renewal is only at the surface and not depth dependent. With the power law for the renewal rate, Eq. 2.25 turns into the following form:

$$0 \;=\; \frac{\mathrm{d}^2}{\mathrm{d}z_+{}^2}\,\bar{c}(z_+) - \gamma_{+p}\,z_+{}^p\,\bar{c}(z_+) \;\;\text{with}\;\; \gamma_{p+} = \gamma_p\,z_\star{}^p\,t_\star \tag{2.29}$$
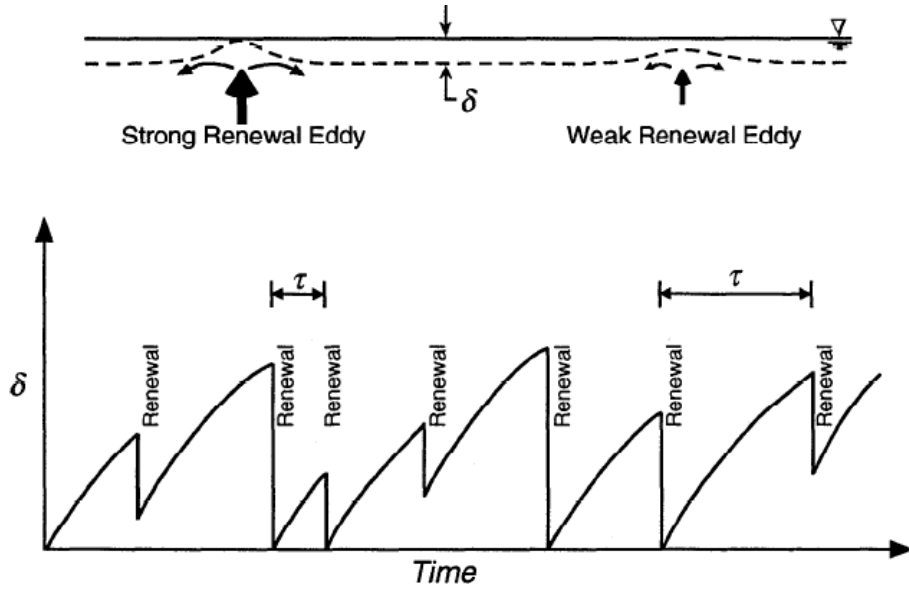
Figure 2.3: Variation of the boundary-layer thickness due to surface-renewal events. N.B.: δ is identical to $z_\star$ of Eq. 2.8 (Adapted from GULLIVER [1991])

For $p = 1$ this equation is the Airy differential equation and the solution for $\bar{c}(z_+)$ is an Airy function:

$$\frac{\mathrm{d}^2}{\mathrm{d}z_+{}^2}\,\bar{c}(z_+) \quad = \quad \gamma_{+1}\,z_+\,\bar{c}(z_+) \tag{2.30}$$

$$\bar{c}(0) = 1 \quad \text{and} \quad \left.\frac{\mathrm{d}\bar{c}(z_+)}{\mathrm{d}z_+}\right|_{z_+=0} = -1 \quad \text{and} \quad \lim_{z_+\to\infty}\bar{c}(z_+) = 0 \quad \Rightarrow \quad \gamma_{+1} \approx 2.58$$

$$\Rightarrow \quad \bar{c}(z_+) \quad = \quad \frac{1}{\mathrm{Ai}(0)}\,\mathrm{Ai}\left(-\frac{\mathrm{Ai}(0)}{\mathrm{Ai}'(0)}\,z_+\right) \approx 2.82\,\mathrm{Ai}\,(1.37\,z_+) \tag{2.31}$$

In Fig. 2.2 the form of this function is compared to the results of the other models.

For the surface-renewal model, CSANADY [1990] calculated the dependence of the SCHMIDT-number exponent to be the same as in the K-model with $\frac{2}{3}$ and $\frac{1}{2}$ for a smooth rigid surface ($p = 1$) and a free surface ($p = 0$) respectively yielding the following relation:

$$n = 1 - \frac{1}{p+2} \tag{2.32}$$

This means that at a free surface it is assumed that every renewal event reaches the phase boundary. Thus, when a mean concentration profile follows the prediction of the surface-renewal model, a concentration fluctuation at the phase boundary is expected while the other presented models do not predict fluctuations directly at the surface.

2.3   Gas-Exchange Parameters from Depth Profiles

From the form of the depth profile like in Fig. 2.1 there are two ways of accessing the transfer velocity k: one is the calculation of the gradient at the surface using Eq. 2.8. This method is independent of the structure of turbulence because turbulence can be neglected at the surface:

$$k = \frac{-D \left.\frac{\partial c}{\partial z}\right|_{z=0}}{\Delta c} \qquad (2.33)$$

The other method measures a depth dependent on the assumed turbulence structure in the aqueous boundary layer. One criterion for the turbulence is the surface condition: is it wavy or flat. Another one is the form of the mean profile following the theory discussed in Sec. 2.2.

Knowing the functional description of the concentration, the boundary-layer thickness $z_\star$ can be found at the depth $z_+ = 1$. As can be seen in Fig. 2.2, this is for the K-model from Eq. 2.20 and Eq. 2.21 $\bar{c}(1) = 0.361$ and $\bar{c}(1) = 0.235$ for $m = 2$ and $m = 3$ respectively. In the surface-renewal model the values from Eq. 2.29 and Eq. 2.31 are $\bar{c}(1) = 1/e = 0.368$ and $\bar{c}(1) = 0.240$ for $p = 0$ and $p = 1$ respectively.

As this is only valid for the mean profile, a statistical problem arises that is mentioned recently in Jähne et al. [2007]. For this technique, taking the mean of the concentration is equivalent to averaging the boundary-layer thickness $z_\star$ what is after Eq. 2.8 proportional to the inverse of the transfer velocity k:

$$\langle z_\star \rangle = D \left\langle \frac{1}{k} \right\rangle \neq \frac{D}{\langle k \rangle} \qquad (2.34)$$

The determination of k via a thickness $z_\star$ in a mean profile is only admissible if the variation of the concentration-profile form is not very high. This is especially not the case in the surface-renewal model with a free surface where the transport is dominated by statistical processes in which the form of the profile changes completely. In LIF experiments sometimes injection events are visible what is also reported by several other authors [Herlina and Jirka, 2004; Takehara and Etoh, 2002]. Variano and Cowen [2007] cited also Nagaosa [1999] and Magnaudet and Calmet [2006] that show similar phenomena in simulations.

For this case Jähne et al. [2007] proposed a bimodal evaluation calculating two different values of k, one for surface-renewal events and another for the time in between. The difficulty for the implementation is to find a unique criterion in every instant for this decision.

In LIF experiments that visualised the water boundary layer, the correct gradient of the oxygen concentration at the surface could not be determined directly because of optical blurring and high noise level. To reduce the noise, either smoothing of the data was done or averaging over a number of depth profiles, or both [DUKE and HANRATTY, 1995; MÜNSTERER, 1996; HERLINA, 2005].

To handle the blurring, some authors applied the method of taking the highest gradient of the smoothed data in some depth near the surface as the gradient at the surface defining the mass flux j. The data near the surface, where the blurring was obvious, was corrected by extrapolation. Assuming an exponential function, the boundary-layer thickness $z_\star$ was measured at a depth where the concentration decreased to $1/e$.

$$c_+(z) = \mathrm{e}^{-z/z_\star} \Rightarrow c_+(z_\star) = \frac{1}{\mathrm{e}} \tag{2.35}$$

In an exponential function this distance is the same as the inverse of the normalised concentration gradient at the surface or the distance from the surface at the extrapolation of this gradient to the bulk concentration level c_{bulk}.

$$-\left.\frac{\partial c_+}{\partial z}\right|_{z=0} = -\frac{1}{z_\star} \tag{2.36}$$

The highest gradient of smoothed measured data is often far from the surface and so the distances are not the same.

In this work both aspects, blurring and noise, were considered by fitting a model function that consists of a convolution of a function describing the concentration increase near the surface and a Gaussian smoothing function assumed as the point spread function (PSF) expressing the blurring explained in detail in Sec. 5.6. This fitting procedure is stable enough to determine the boundary-layer thickness of the noisy single depth profiles that were measured when no surface-renewal events are seen. With surface-renewal events the theoretical profiles are applicable only to mean profiles where the noise level is low. The different steps will be described in detail in Chap. 5 about the image processing methods. The results of fitting single profiles will be compared to the fits of mean profiles in Sec. 6.1.3.

2.4 Review: Gas Exchange with LIF in the Literature

In the literature two different kinds of visualisation techniques for gases dissolved in water are reported: first the pH-indicator technique and later the oxygen-quenching technique with the pH-indicator technique.

The key point of the pH-indicator technique is the conversion of the flux of an acid or alkaline gas from the air to the water surface into a flux of fluorescence intensity by a chemical reaction with a dye. 40 years ago this technique was used to investigate the gas-transport mechanisms in falling films (Fahlenkamp [1979]; Hiby et al. [1967]; Hiby [1968, 1983]). In 1989, the pH-indicator technique was first used in a grid-stirred tank by Asher and Pankow [1989]. The authors measured time series of the CO_2 concentration fluctuations close to a gas-liquid interface at a fixed position using dichloro fluorescein. The first successful measurements of vertical concentration-profiles within the aqueous mass-boundary layer at a free interface in a wind–wave facility were reported by Jähne [1991] using HCl gas. More detailed studies using fluorescein followed later (Münsterer [1996]; Münsterer and Jähne [1997]; Schladow et al. [2002]; Variano and Cowen [2007]).

In the same year, the first successful measurements from wind–wave flumes using the oxygen-quenching technique were reported by Wolff et al. [1991]. Pyrene butyric acid PBA was used, a dye known from measurements of dissolved oxygen concentrations in cells (cf. Vaughan and Weber [1970]). PBA luminescence was stimulated by a N_2 laser in the UV at 337 nm. Later other authors used the same dye in wind–waves flumes (Münsterer [1996]; Münsterer et al. [1995]; Woodrow and Duke [2002]) and grid-stirred tanks (Herlina and Jirka [2004, 2007]) for oxygen exchange studies.

The rather qualitative character of the previously published results indicates that the currently used fluorescent dyes still show significant disadvantages. The use of PBA to measure oxygen dissolved in water gives rise to several problems. Firstly, the quenching effect is rather weak causing a poor signal-to-noise ratio of the concentration measurements. Secondly, it is difficult to solve PBA in water. Thirdly, PBA is a surface active chemical species. This means that the hydrodynamic boundary conditions at the air–water interface (surface tension and surface elasticity) are altered by PBA. Thus, the search for a more suitable fluorescent dye seemed promising, and a better luminescent dye for the oxygen-quenching technique could be found that will be presented in the next chapter.

Part II

Experimentals

Chapter 3

Characterisation: Phosphorescence Dye and Quenching

The currently applied dye in oxygen visualisation techniques, pyrene butyric acid PBA, showed disadvantages like weak susceptibility to quenching, low solubility and surface activity. Hence, the search for a more suitable alternative seems promising. CASTELLANO and LAKOWICZ [1998] proposed a ruthenium complex as a soluble phosphorescent dye for the analysis of oxygen concentrations in water.

This class of the luminescent dye, that is used in this work, has little application in other fields because this type of chemical species does not behave well in living cells and most application need to fix an insoluble dye in a medium such as membranes. Consequently, this chemical is not easily available. The synthesis of the metallo-organic complex is described before it is characterised by its spectra of absorption and emission.

3.1 Luminescence and Quenching

There are different processes inducing a substance to emit light. Energy sources other than light are present in chemiluminescence (chemical reaction), incandescence (heat), electroluminescence (electrical current), crystalloluminescence (crystallisation), fractoluminescence (fracture of a crystal), piezoluminescence (pressure) or radioluminescence (ionising radiation).

In light induced photo-luminescence the energy comes from the absorption of UV or visible light exciting an electron from its singlet ground state S_0 to a vibrational state of the first excited singlet state S_1. These energy transitions are depicted in the so-called JABLONSKI diagram in Fig. 3.1.
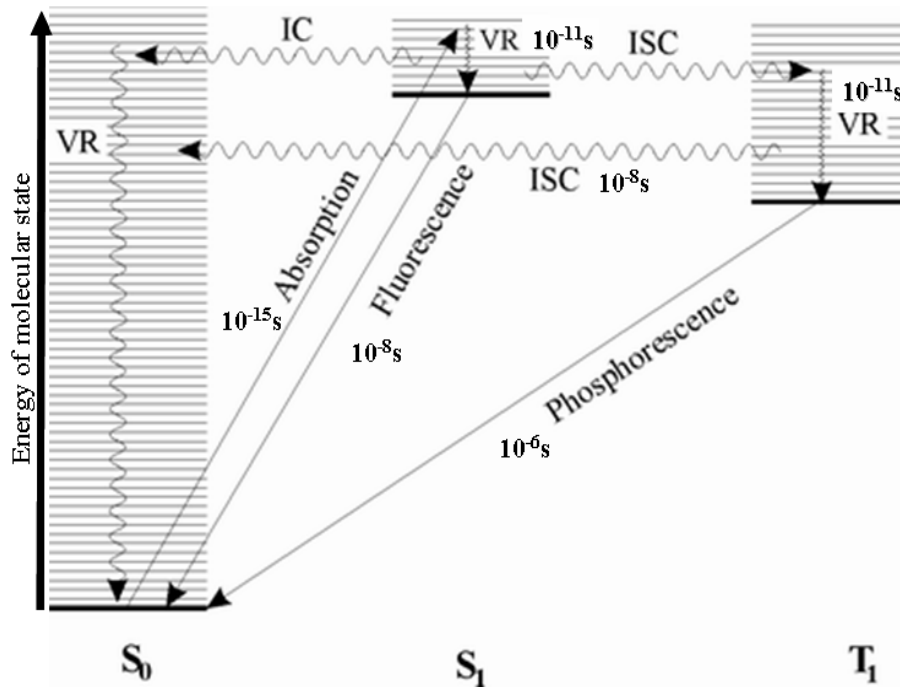
Figure 3.1: JABLONSKI diagram describing the energy transitions and typical
lifetimes in a molecule relevant for fluorescence and phosphorescence

After the absorption the vibronic energy is dissipated into heat and the
particle ends up in the vibronic ground state of the excited state S_1. From
here there are different relaxation paths. In fluorescence a photon is emitted
and a vibrational state of the ground state S_0 is reached. Then the lifetime
of the excited state is of the order of 10^{-8} s. Fluorescence is observed only
in the case that the faster process of internal conversion (IC) is suppressed,
which leads to a transition from one singlet state into another. Here the
energy would be dissipated by a non-radiative relaxation.

In some cases the excited energy states of the triplet and the singlet
interact allowing a intersystem crossing (ISC) into the triplet state T_1. The
ground state of the excited triplet state has a long lifetime because the photon
emission relaxing to a singlet state is not allowed and thus shows lifetimes τ
usually longer than 10^{-7} s. This emission is called phosphorescence.

Absorption leads to an excited state of the molecule. The probability for
an electronic excitation to cause an emission of a photon is called quantum
yield ϕ of the luminescence. In addition, the presence of certain substances
may decrease the luminescence further. This quenching of the luminescence
intensity I depends on the concentration of the quencher [Q]. When a lumi-
nescent dye is excited continuously the absorption rate a and the relaxation
rate $\tilde{a}$ are of the same magnitude. The relaxation is proportional to the con-
centration of the dye in the excited state $[D^\star]_0$. In absence of any quencher

the relaxation can be non-radiative energy dissipation with a rate k_{nr} or the emission of a photon with the luminescence rate Γ_{rad}.

$$a = \tilde{a} = (k_{nr} + \Gamma_{rad}) [D^\star]_0 = \gamma [D^\star]_0 \qquad (3.1)$$

The constant of proportionality γ is the inverse of the lifetime τ_0 of the excited state in absence of the quencher. In the presence of a quencher but keeping the excitation a the same, there is an additional relaxation rate k_Q. With higher concentrations [Q] of the quencher, a higher quenching effect is observed:

$$a = \gamma [D^\star] + k_Q[Q][D^\star] \qquad (3.2)$$

Taking the ratio of Eq. 3.1 and Eq. 3.2 simplifies the relation. The number of photon emissions and thus of luminescence intensity I is correlated directly with the number of molecules in the excited state $[D^\star]$:

$$\begin{aligned}
1 &= \frac{\gamma [D^\star]_0}{(\gamma + k_Q[Q]) [D^\star]} \\
\Rightarrow \frac{[D^\star]}{[D^\star]_0} = \frac{I}{I_0} &= \frac{\gamma}{\gamma + k_Q[Q]} = \frac{1}{1 + k_Q\tau_0[Q]} \quad \text{with} \quad \tau_0 = \frac{1}{\gamma} \\
\frac{I}{I_0} &= \frac{1}{1 + K_{SV}[Q]} \quad \text{with} \quad K_{SV} = k_Q\tau_0 \qquad (3.3)
\end{aligned}$$

The Eq. 3.3 is called Stern–Volmer equation [1919]. With high values of the quenching constant K_{SV}, the luminescence is very sensible to the presence of oxygen. The dependence on the quenching concentration is evident when the luminescence is plotted versus the quencher concentration as it is done in Fig. 3.2.

There are different mechanisms of quenching. It may occur after the formation of a temporal complex between the quencher and the dye. In this static quenching the concentration of the active luminophore is reduced and the absorption spectrum may be changed due to the absorption of the complex. The luminescence lifetime is independent of the concentration of the quencher.

In dynamical quenching the decrease of luminescence is induced by collisions between the dye and the quencher. Here the quantum yield ϕ is reduced and also the lifetime of the excited state is shorter. By measuring the decrease of luminescence with time after a very short excitation pulse as it is done in fluorescence lifetime imaging FLIM, dynamical quenching can be distinguished from static quenching.

In the case of the triplet, molecule oxygen the mechanism seems to be a spin–spin interaction leading to intersystem crossing with non-radiative
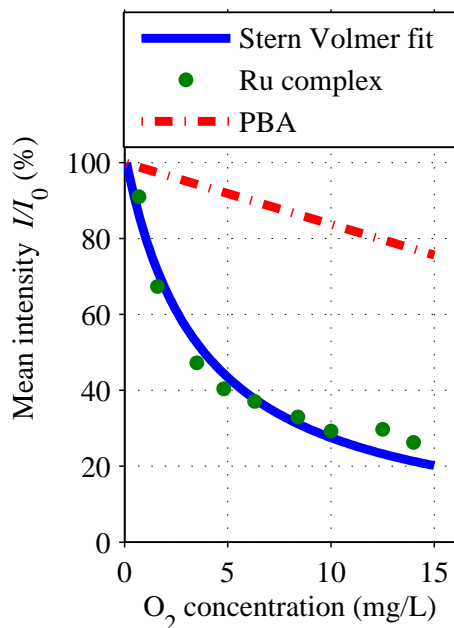
Figure 3.2: Relation between the quencher concentration and the luminescence of the ruthenium complex described in Sec. 3.3 (K_{SV}=11300) and the often used dye PBA (K_{SV}=645, Vaughan and Weber [1970], *dash-dotted line*). The *values* for the ruthenium complex are taken from Vogel [2004]. The *solid line* is a fit of the Stern–Volmer relation to the data. More dense data points are found in Fig. 5.8

relaxation. Lakowicz [2006, Chap. 9.2] cites some authors [Evans, 1957; Kawaoka et al., 1967; Kearns and Stone, 1971] that have studied oxygen quenching but the correct mechanism is still discussed.

3.2   Beer–Lambert's Law of Absorption

In the beginning of photo-luminescence processes, the energy is transferred to the molecule by absorption of light. When electro-magnetic radiation passes a medium, it can interact with the matter inducing absorption that in general depends on the wavelength λ of the radiation. The attenuation of the light intensity $dI'(\lambda)$ is proportional to the incident intensity I' in this area.

$$\frac{dI'(\lambda)}{dx} = -\alpha(\lambda)I' \tag{3.4}$$

The absorption coefficient[1] α is characteristic for the passed medium and adopts the unit $\left[\frac{1}{\text{length}}\right]$. By integrating, the light attenuation between the

---

[1]The so-called attenuation coefficient (formerly extinction coefficient) accounts also for scattering and luminescence (cf. International Union of Pure and Applied Chemistry IUPAC [1997]).

points $x = 0$ and $x = l$ can be calculated where the intensity decreases from I_0 to I:

$$\int_{I_0}^{I} \frac{1}{I'}\,\mathrm{d}I' = \int_0^l -\alpha(\lambda)\,\mathrm{d}x =$$

$$-[\ln I']_{I_0}^{I} = [\alpha(\lambda)\,x]_0^l =$$

$$-\ln I + \ln I_0 = +\alpha(\lambda)\,l - 0 =$$

$$\ln \frac{I_0}{I} = \alpha(\lambda)\,l \tag{3.5}$$

The inverse of α is called penetration depth l_p and denominates the distance in which the radiation decreases to $1/\mathrm{e}$. Disregarding luminescence and scattering, the transmittance T decreases exponentially with the length of the optical path l in the matter.

$$T = \frac{I}{I_0} = \mathrm{e}^{-\alpha(\lambda)\,l} \tag{3.6}$$

When a chemical substance in the medium causes the absorption, the absorption coefficient α can be expressed using the number concentration $n = \frac{\text{number}}{\text{volume}}$ of the substance: $\alpha = n\,\sigma_\mathrm{A}$, where $\sigma_\mathrm{A}(\lambda)$ has the area unit $[\mathrm{m}^2]$ and thus describes the absorption cross section.

The fraction of the absorber can also be given by the amount concentration of the molecules $c_\mathrm{A} = \frac{n}{N_\mathrm{A}}$ in units of $\left[\frac{\text{mol}}{\text{L}}\right]$ with the Avogadro number $N_\mathrm{A} = 6{,}022\,10^{23}\,\frac{1}{\text{mol}}$. This yields the molar absorption coefficient[2] κ_A in units of $\left[\frac{\text{cm}^2}{\text{mol}}\right]$: $\alpha(\lambda) = c_\mathrm{A}\kappa_\mathrm{A}(\lambda)$.

Taking the decadic logarithm of Eq. 3.6 leads to a form of the Beer–Lambert's law.[3] Here the absorbance (or absorbancy) A is proportional to the length of the optical path l in the medium and to the concentration of the absorber c_A with the decadic molar absorption coefficient ε_A as a material property constant of the solved substance.

$$A = -\lg \frac{I}{I_0} = c_\mathrm{A}\,\varepsilon_\mathrm{A}(\lambda)\,l \tag{3.7}$$

This absorbance A is frequently found in spectroscopy characterising the spectroscopic property of a substance at the wavelength of highest absorption. While the absorbance depends on the length of the optical path in the

---

[2]The symbol κ is preferred by the IUPAC [1997] for the natural logarithmic absorption coefficient.

[3]Often called Beer–Bouguer–Lambert or simply Beer's law. In German the chronological order of the names is followed. This exponential relation was found independently in similar forms by the two scientists: Pierre Bouguer 1729, Johann Heinrich Lambert 1760. It was extended to the concentration in liquids by August Beer 1852.

medium and the concentration of the absorber, the extinction coefficient at a certain wavelength is specific for any substance. Analogously, the expression $\ln \frac{I_0}{I}$ is called NAPIER absorbance[4] A_e. The different factors can be converted with this relation: $\kappa = \sigma_A \, N_A = \varepsilon \ln 10$.

3.3 Ruthenium Complex as a Luminescent Dye

Oxygen has been known a long time as a substance that reduces quantum yields of luminophores [KAUTSKY, 1939]. As O_2 is abundant in the atmosphere, this is a problem for most applications in fluorescence spectroscopy. To use this phenomenon fruitfully for the measurement of oxygen concentrations, some luminescent dyes with long lifetimes show the suitable quenching properties.

VAUGHAN and WEBER [1970] presented pyrene butyric acid PBA as a quenchable dye. The water solubility and favourable properties made of it a versatile oxygen indicator in cell biology as well as in visualising gas-exchange processes. Its structure is shown in Fig. 3.3.b. A disadvantage of the dye is that it lowers the surface tension like a tenside in a soap. Then the molecules accumulate at the surface because the energy is lower when the ionic part is solved in the water and the hydrophobic organic part has less contact with water. The same low energy condition can be established when these molecules gather to form micelles in the water.

Surface activity of a dye for visualising the gas exchange with different wind conditions is not desired because it lowers the concentration in the bulk but foremost because surfactants alter the surface tension and reduce the waves (cf. FREW et al. [1995]; FREW [1997]). Other disadvantages of this dye will be analysed in detail in Sec. 3.7.

Phosphorescence in aqueous solutions is observed rarely (cf. Chap. 8.18 in LAKOWICZ [2006]) because the luminescence of long lifetime states are quenched quickly by oxygen or other quenchers like amino acids, CS_2 or even water itself. It occurs only where the chromophoric centre is well protected like inside a protein or a screening organic ligand. This is the case for example in platinum or palladium porphin derivates and also for diimine complexes

---

[4]After a posthumous publication of NAPIER of 1619 about the logarithm with the base e but also the term optical density $OD(\lambda)$ or extinction is common, what is used more in general as the sum of absorption, luminescence, reflection and dispersion. The IUPAC [1997] dissuades from the use of these terms because they were not clearly defined. The implicating logarithms are not always with the same base leading to misunderstandings because in the physical literature the work with the natural logarithm is more usual.
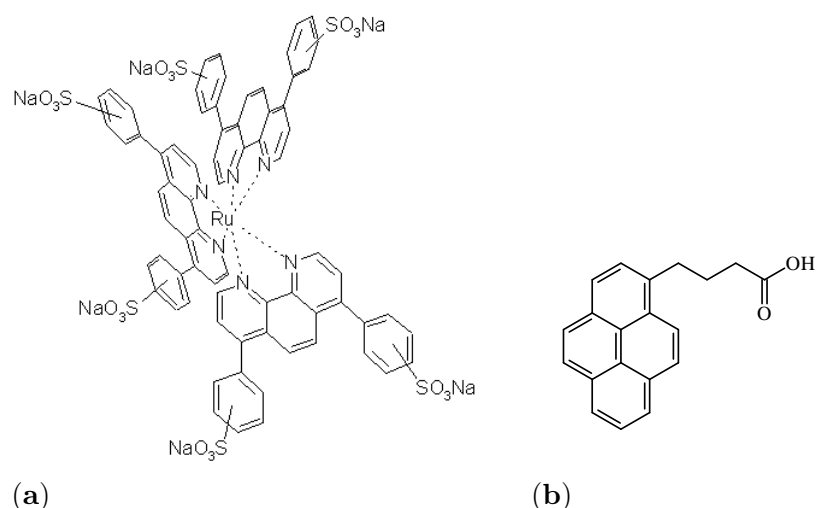
Figure 3.3: Chemical structure of luminescent dyes. (**a**) The ruthenium complex Ru(dpp ds)$_3$. (**b**) The organic molecule pyrene butyric acid PBA

of ruthenium, osmium and rhenium (cf. Chap. 20.3 in LAKOWICZ [2006]).

ZELELOW et al. [2003] applied a platium(II) porphyrin complex for oxygen measurement diffused in a membrane. BARLOW et al. [1998] used the quenching of a phosphorescent palladium(II) porphin complex to measure the concentration of oxygen in the heart organ with an imaging technique.

The system for measuring oxygen water concentrations proposed by CASTELLANO and LAKOWICZ [1998] is based on another soluble phosphorescent metal complex. The structure shown in Fig. 3.3 is a chemical compound consisting of three diimine ligands and a ruthenium central ion. Its systematic name is sodium tris(4,7-diphenyl-1,10-phenanthroline disulfonic acid)ruthenate(II) (Na$_4$[Ru^{II}(dpp ds)$_3$]) and the sum formula is Na$_4$[Ru(C$_{24}$H$_{14}$N$_2$O$_6$S$_2$)$_3$] with a molecular weight of $M = 1710.6$ g/mol and the Chemical Abstracts Service Registry Number (CAS) 23316-7-5.

The literature knows the ligand also with the names disodium batho-phenanthroline-disulfonate BPS, 4,7-diphenyl-1,10-phenanthrolinium di(sodiosulphonate) or (1,10-phenanthroline-4,7-diyl)bis-benzenesulfonic acid disodium salt and it has the specific weight of $M = 536.5$ g/mol. The ligand is sold as a hydrate of the disodium salt (CAS: 52746-49-3 or 53744-42-6). The position of the sulfonate groups is often given as 4,4' (*para*) but in most synthesis this position is not controlled.

The ionic sulfonate groups turn the molecule into a water-soluble substance. The 3-D structure is symmetric and thus shows no surface activity.

A related compound without the sulfonic acid groups, so that it is not soluble in water, is the tris(4,7-diphenyl-1,10-phenanthroline)ruthenium(II) dichloride (Ru(dpp)$_3$) (CAS 36309-88-3). Fixed in a membrane the dye is

used in sensors to measure oxygen concentrations with a optical method described by Lakowicz [2006, Chap. 19.4].

A new application for oxygen indicating dyes is the use in optodes, i.e. membrane tips at the end of light conducting glass fibres [Narayanaswamy and Wolfbeis, 2004; Schröder, 2006; Schröder et al., 2007]. These can measure the oxygen concentration in environments as small as a single biological cell.

3.4   Chemical Synthesis of the Ruthenium Complex

In the literature [see overview of Krause, 1987] various reactants were employed for the synthesis of this class of compounds. No objections to the use of ruthenium chloride, $RuCl_3$, were found. Other educts like potassium pentachloro ruthenate K_2RuCl_5 seemed to be more expensive related to the content of ruthenium.

Only the complex with a reduced Ru^{2+} ion as a centre atom shows the characteristic colour and phosphorescence. As a reductive reactant, ascorbic acid (AscA) was chosen because of its availability.

Other reducing agents mentioned by Krause [1987] are hypophosphite (NaH_2PO_2) or tartrate ($Na_2(HCOHCOO)_2$). Rose and Wilkinson [1970] proposed to reduce first the ruthenium with hydrogen gas H_2. This avoids the creation of side products but the intermediate solution of blue ruthenium(II) is prone to oxidation and can be handled only in inert atmosphere, e.g. by employing standard Schlenk techniques. Anderson and Seddon [1979] urged workers to adopt this method where trace impurities may be critical in spite of the grater intricacy and lower yields involved. The synthesis of $Ru(dpp\,ds)_3$ via the blue solution is described by Anderson et al. [1985].

A variant of the applied synthesis of the η^2-chalate complex is described in Rabilloud et al. [2001] without any purification. In the publication the solution of the dye can be stored in the refrigerator for several months. It was applied for staining proteins in electrophoresis.

Chemical reaction:

$$Ru^{III}Cl_3 + 3\,Na_2(dpp\,ds) \xrightarrow[T]{AscA} Na_4[Ru^{II}(dpp\,ds)_3] + 2\,NaCl + HCl \quad (3.8)$$
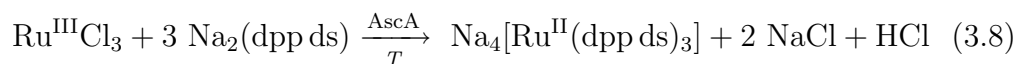
100 mg (0.45 μmol) ruthenium(III) chloride hydrate, $RuCl_3 \cdot x\,H_2O$ (alfa aesar, Karlsruhe), were solved in 20 ml deionised water and heated to boiling temperature. The use of a reflux condenser is advisable. 800 mg (1.5 μmol) of the ligand 4,7-diphenyl-1,10-phenanthroline disulfonic acid disodium salt

(98%, alfa-aesar, Karlsruhe) was added in little excess and the solution was kept boiling for 20 min. The solution turned in deep greenish brown.

An excess of 1 g (5.7 µmol) ascorbic acid sodium salt (AscA, here vitamin C L-ascorbic acid) was added and boiled further 20 min. The solution changed colour instantly to orange–brown. The filtering of the hot product solution was skipped. After cooling down to room temperature, the pH was adjusted to 7 with diluted sodium hydroxide solution. The solution showed now the characteristic red luminescence when illuminated with blue light.

The solution can be evaporated and dried in a exsiccator over phosphorus pentoxide P_4O_{10} in vacuum what gives a orange–brown solid. As the ruthenium complex is not soluble in other solvents than water, the substance was cleaned with ethanol. With this, most of the excess of educts and other salts are taken away.

For further purification the chemical compound can be recrystallised from ethanol–water solution. After solution in little amount of water the substance can be chromatographed with water as eluant as described by ANDERSON et al. [1985].

3.5   Absorption Spectra of the Dye

The absorbance A of the ruthenium dye following the definition of Eq. 3.7 was measured with a commercial HP 8453 UV–Vis spectrometer. The spectrum is shown in Fig. 3.4.
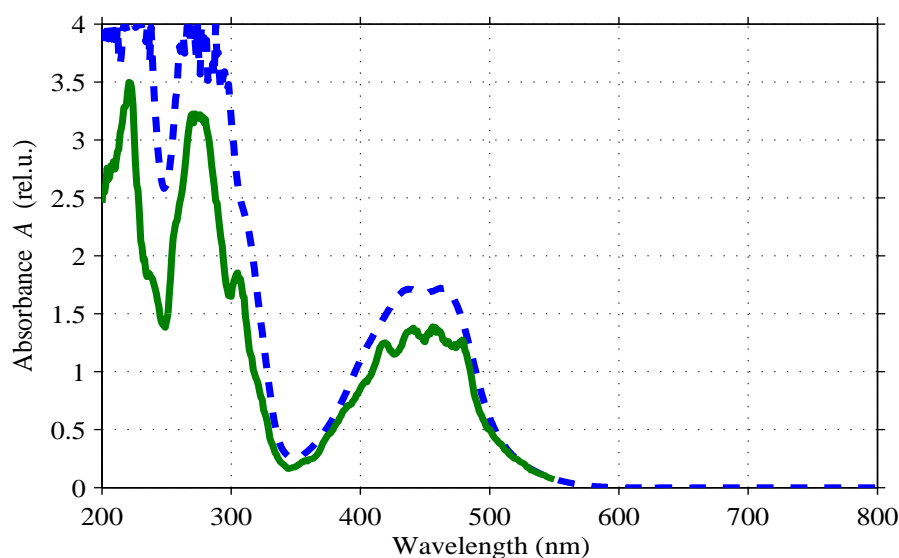
Figure 3.4: Absorption spectra of the ruthenium complex: absorbance of a UV–Vis spectrometer (*broken line*) and absorption measured via the emission at 617 nm in a fluorescence spectrometer (*solid line*)

There are several high absorption bands in the UV range of the wavelength spectrum below 350 nm and a broad distinct absorption band in the blue between 400–500 nm. The absorption maximum in the blue is 462 nm.

The relation between absorption and emission can be measured in a fluorescence spectrometer. The emission at a fixed wavelength is measured while the exciting light energy is changed continuously. This is done with a Fabry–Pérot interferometer (often called etalon) as a adjustable band-pass filter in the path of the white exciting light. The intensity of the detected luminescence must be normalised with the spectrum of the white exciting light to compensate its effect.

In Fig. 3.4 also the spectrum of such a measurement is shown. The wavelength of the detected luminescence was fixed at 617 nm so that the best dynamic range of the signal could be used. The differences in the spectra may be explained by a better resolution of the fluorescence spectrometer. The thin band width of the light passed through the etalon seems to be better than the resolution of the UV-Vis spectrometer determined by the slit function and the discretisation in pixels in the line detector. The differences in the UV range of the spectrum can be caused also by absorptions of the dye that do not induce phosphorescence at the fixed emission wavelength. Here the absorptions result in higher electronic states that have different probabilities for transitions into the triplet state T_1 in Fig. 3.1.

3.6   Phosphorescence Emission Spectra

The luminescent emission spectra were obtained with two methods. One was the excitement with a blue LED with a central wavelength of 445 nm. The emission was analysed with the Ocean Optics spectrometer USB2000. A glass fibre was positioned 90° to the LED in front of a small cuvette with a solution of the dye. The scattered blue light from the LED was filtered with an edge filter that cuts off any light above 470 nm. The fibre was mounted at the case of the spectrometer. Two spectra with different oxygen concentrations in the solution are displayed in Fig. 3.5.b. The amount of oxygen dissolfe in the water did not change the shape of the spectrum but only the intensity.

A second method is to measure the emission in a fluorescence spectrometer also shown in Fig. 3.5.b. Here the excitation wavelength was fixed to 473 nm (*solid line*) and 279 nm (*broken line*) and the wavelength of the emission was scanned with the same etalon filter as for the absorption spectrum in Fig. 3.4.

There is no characteristic difference in the emission between 550–750 nm but there is an additional luminescence between 350–450 nm when the ruthe-
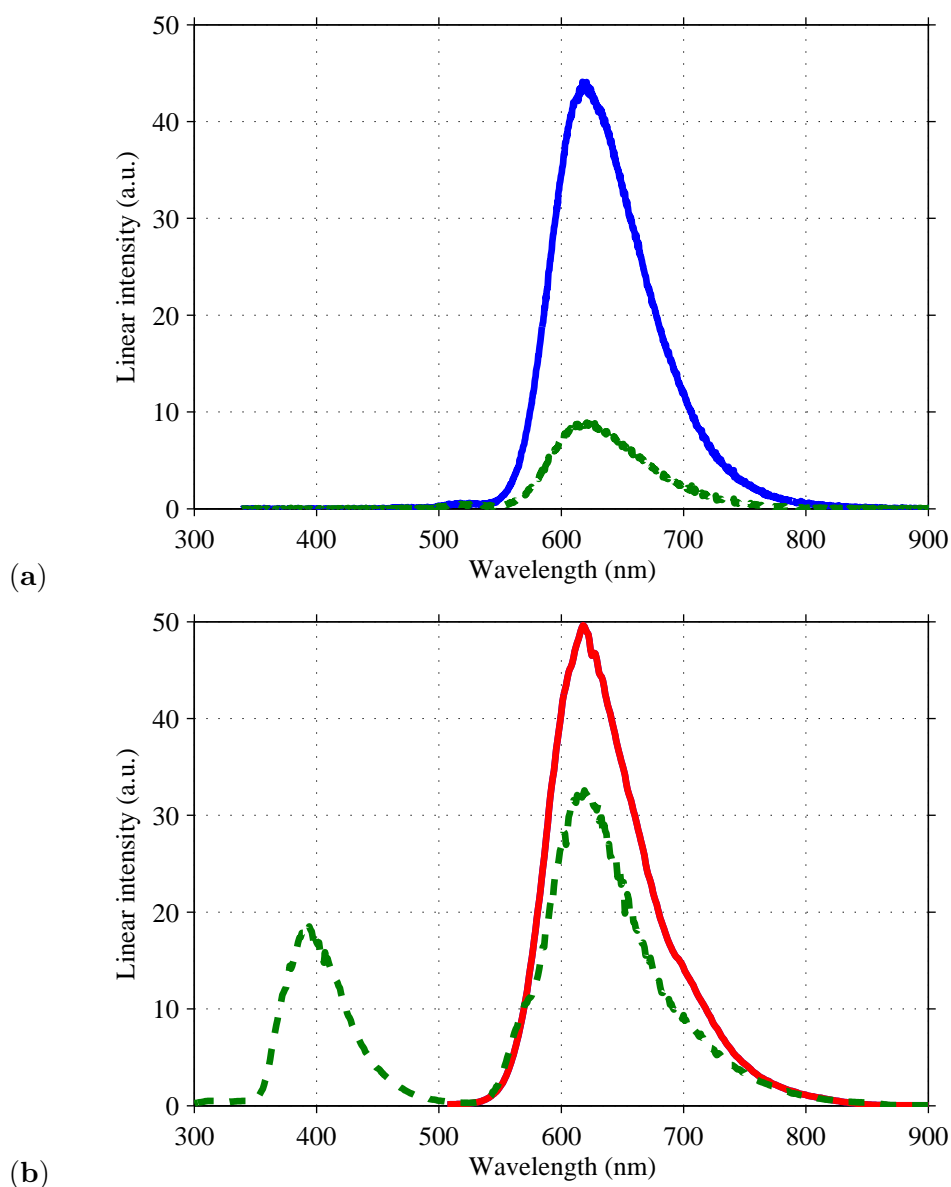
Figure 3.5: Emission spectra of the ruthenium complex observed at different oxygen concentrations and excitation wavelengths. (**a**) Oxygen concentration of 8 mg/mol (*solid line*) and 1 mg/mol (*broken line*) exciting with a blue LED showed the identical shape. (**b**) Spectra from a fluorescent spectrometer with excitation 279 nm (*broken line*) gives the same emission in the red as excited with at 473 nm (*solid line*) but has an additional emission in the UV

nium complex is illuminated with UV light. This can be fluorescence or phosphorescence of the second excited triplet state T_2. It was not studied if absorptions of wavelengths below $350\,\text{nm}$ lead to the same quenching properties like the excitation with longer wavelengths.

For comparison with the linear emission spectrum, the logarithmic absorbance spectrum of Fig. 3.4 was transformed into a linear intensity spectrum I_A by doing the following calculation:

$$I_A = 10^A - 1 \tag{3.9}$$

The large Stokes shift between the absorption and the emission with little overlap of the spectra in Fig. 3.6 demonstrate that there is very little self-absorption. This is an advantage for a dye in the application as an indicator.
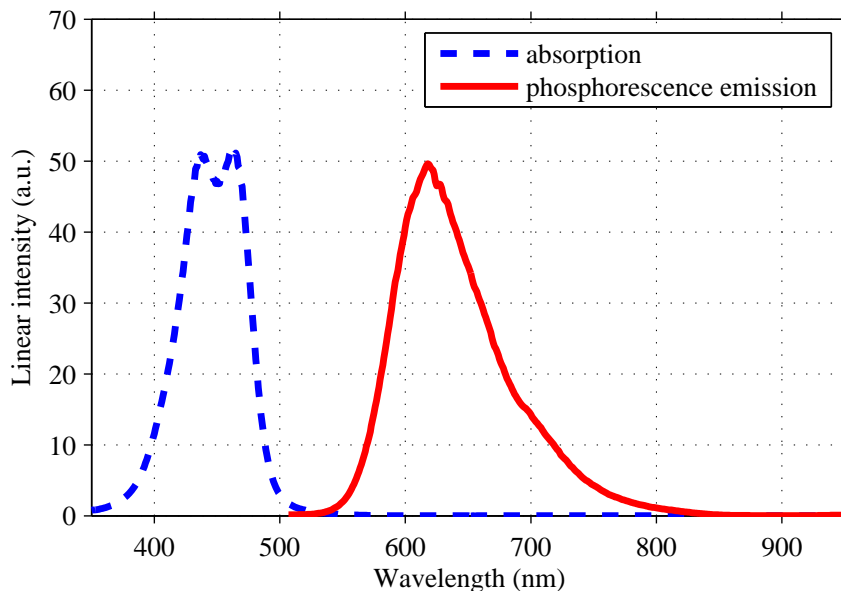
Figure 3.6: Absorption and emission spectra of the Ru complex: absorbance of a UV–Vis spectrometer (*broken line*) and phosphorescence emission after the excitation with the wavelength of $473\,\text{nm}$ in a fluorescence spectrometer (*solid line*)

3.7 Comparison of the Ruthenium Complex with PBA

For the measurement of oxygen concentrations, the luminescent dye has to fulfil some requirements of very different aspects. An ideal oxygen indicator as a water soluble dye for the herein described type of application should comply the following list:

Desired properties:
⋄ High quenching constant   ⋄ Large STOKES shift
⋄ High absorbance   ⋄ Good solubility
⋄ Good quantum yield   ⋄ Low surface activity
⋄ High photo-stability   ⋄ Compatibility with available light sources

Regarding this list of desirable characteristics, the advantages of the ruthenium complex can be compared to pyrene butyric acid PBA of Fig. 3.3 that has been widely used in other oxygen–LIF studies of gas exchange (for literature see Sec. 2.4).

- A high quenching constant, and thus, high sensitivity according to the STERN–VOLMER equation in Eq. 3.3, requires a long lifetime of the excited state in the order of at least some µs. Ru(dpp ds)$_3$ shows a unquenched lifetime of 3.7 µs and a quenching constant K_{SV} defined by Eq. 3.3 of 11 300 L/mol (0.35 L/mg) as reported by CASTELLANO and LAKOWICZ [1998] and confirmed by own measurements shown in Fig. 5.8. This graph shows that the intensity of luminescence in air saturated water with a oxygen concentration of 8.3 mg/mol is only about 10% of the intensity in absence of oxygen. Hence, 90% of the phosphorescence was quenched. The indicator is especially sensitive at low oxygen concentrations. This represents a much higher sensitivity to oxygen than the quenching constant of PBA (645 ±79 L/mol in VAUGHAN and WEBER [1970] or 683 ±70 L/mol in MÜNSTERER [1996]). The luminescence in air saturated water is still 87% (cf. Fig. 3.2).

- PBA needs a UV laser as a light source (e.g. a N$_2$ laser at 337 nm). This excitation wavelength of high energy leads to some additional bleaching. The ruthenium complex shows better photo-stability and absorbs in the visible blue between 400–500 nm where cheap and handy light sources like LEDs or diode pumped solid state dpss lasers for the stimulation of the luminescence are available. Fig. 3.4 shows 462 nm as a maximum of absorption in the visible.

- The Stokes shift of Ru(dpp ds)$_3$ between a stimulation with 473 nm and an emission maximum of 618 nm (cf. Fig. 3.6) is 145 nm. Above 530 nm, absorption is low enough to have no significant self-absorption of the fluorescent light. This is a much larger Stokes shift than for PBA when employing a N$_2$ laser with a stimulation at 337 nm, an emission maximum at 375 nm and a Stokes shift of 38 nm (cf. Vaughan and Weber [1970]) resulting in self-absorption. Using an other laser like a twice frequency-doubled yttrium–aluminium garnet YAG with the wavelength of 266 nm [Schladow et al., 2002; Lee and Schladow, 2000] changes the excitation wavelength but the problem of the self-absorption is the same.

- The six sulfonic groups make Ru(dpp ds)$_3$ excellently soluble in water, and the dye shows no surface activity (cf. Sec. 3.3). In contrast, PBA is almost insoluble in water. It can only be solved in NaOH before mixing with water resulting in a much lower maximum of concentration.

Chapter 4

Set-up: the Wind–Water Facility

Gas-exchange studies are of interest in oceanography and limnology. To dissolve luminescent dyes in such environments seems to be quite unrealistic. Even though there are experiments of using fluorescein as a tracer for water mixing [HO et al., 2006b].

To study the mechanism in small scales like a air–water boundary layer, it appears to be more appropriate to simulate some of the natural conditions in the laboratory because a luminescent dye can be solved homogeneously in the water and examined with a stable optical set-up under controllable conditions.

The experiments were conducted in a small circular wind–wave channel. In such a facility the wind field over the water surface reaches an equilibrium after some minutes. The optical set-up and the generation of the various wind speeds will be documented in this chapter as well as the methods for changing and measuring the oxygen concentration in the water.

4.1 Set-up at the Circular Wind–Wave Channel

The small circular wind–wave flume in Heidelberg featured a diameter of $1.2\,\mathrm{m}$ and a channel width of $20\,\mathrm{cm}$. A sketch of it is shown in Fig. 4.1. The water height in the presented studies were between $10\text{–}13\,\mathrm{cm}$. The tank was filled with approximately $70\,\mathrm{L}$ of distilled water. The concentration of the added phosphorescent dye was about $10^{-5}\,\mathrm{mol/L}$. The channel was equipped with temperature sensors in the air and the water and some pipe connections for probing water and air samples.

The facility had four rotating paddles to generate the wind. The speed
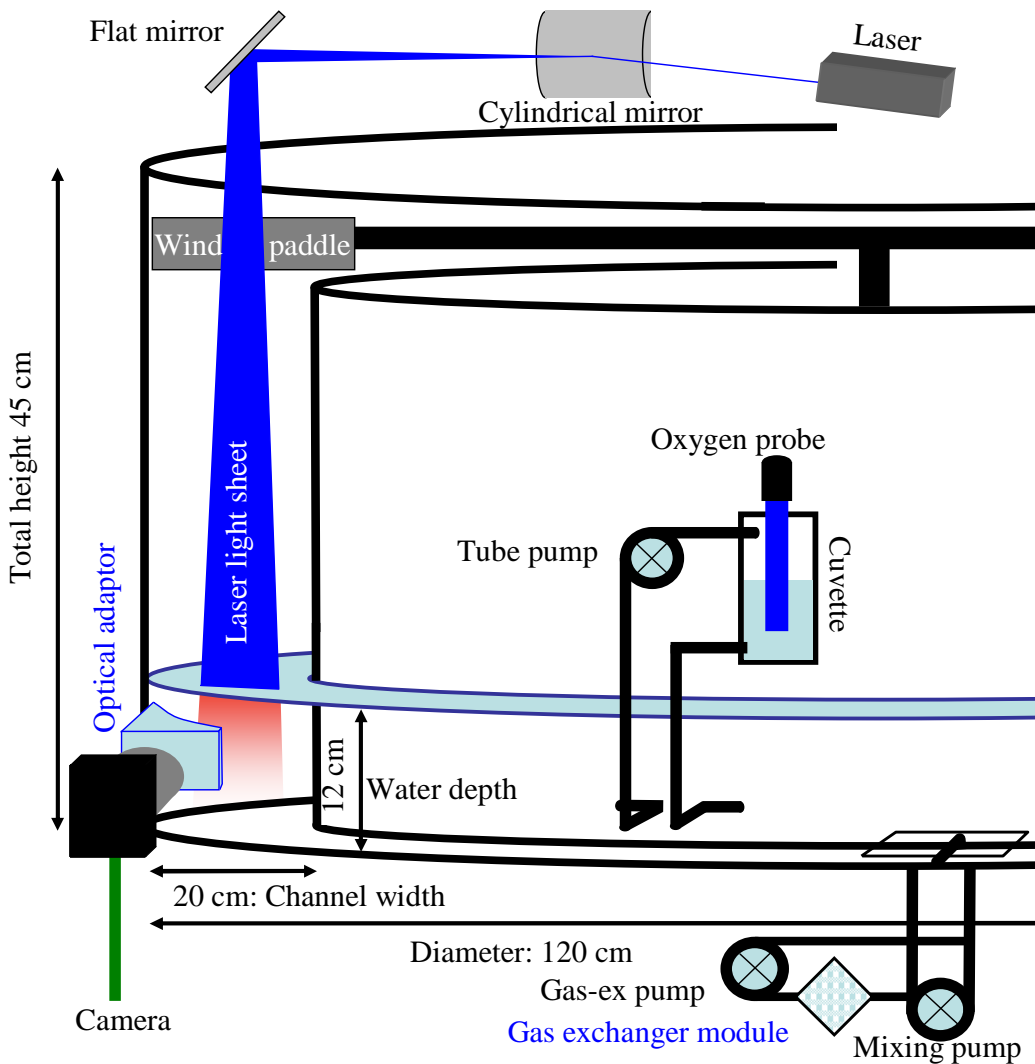
Figure 4.1: Schematic drawing of the small wind–wave facility and the optical set-up

was controlled by adjusting the current of the rotor depending on the actual wind speed. When a propeller sensor reported a lower wind speed the controlling PC raised the current and vice versa.

A commercial Clark-type electrode oxygen sensor was used to gather informations about the value and the changing rate of the oxygen concentration in the water bulk. The amperometric electrodes have their name from Clark [1956]. The method of analysing reducible and oxidisable substances is also called polarography. In modern sensors, oxygen penetrates a membrane of the sensor and is reduced at a cathode, creating a measurable electrical current. This current is proportional to the O_2 concentration in the environment of the device. This technique works in air as well as in water. The reaction of the oxygen is irreversible so that small amounts of oxygen

are consumed during the measuring process. This produces a drift of the signal over time in a stagnant medium. In order to assure stirring, a constant water flux was pumped out of the channel, passed the oxygen sensor in a small cuvette and re-entered the channel.

4.2   Optics for Imaging

A laser sheet was generated with a cylindrical mirror in the path of the laser light. The direction of the sheet was adjusted orthogonal to the wind direction as seen in Fig. 4.1.

Using a scanning flat mirror instead of the cylindrical mirror to generate the laser sheet gave rise to triggering problems with the camera. The homogeneity of the light sheet was slightly better. But the dominant influence on the light-sheet structuring arose from the poor optical properties of the scratched channel cover. In this work only the results with the laser sheet generated by the cylindrical mirror are described. An example of the captured image is shown in Fig. 4.2.
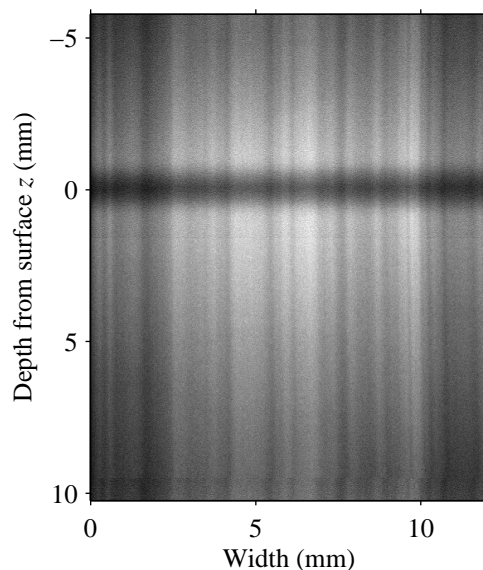
Figure 4.2: Typical image of the laser sheet taken with the measurement camera. The darkening is caused by the quenching of the oxygen penetrating the surface towards the degassed water bulk. The upper part of the image is a total reflection at the surface

The laser was a commercial diode-pumped solid-state dpss laser (from Roithner, Vienna). The output power was adjustable with the current to a maximum of about $50\,\mathrm{mW}$. The output wavelength was fixed at blue $473\,\mathrm{nm}$

with a spectral width much less than the resolution of the available spec-trometers of 0.3 nm.

The laser-line expansion to 2 cm was small relative to the distance of 50 cm between the water surface and the expanding mirror so that the assumption of parallel light in the first 10 mm below the surface is justified. The diameter of the laser beam was about 1 mm what was also the thickness of the resulting light sheet.

The camera was a CCD-camera with 1/3" Kodak sensor (monochrome, progressive scan) with a resolution of 640×480 pixel (Dragonfly Express from Point Grey Research, Canada). The maximal frame rate was 200 frames per second. But when taking a long series of images, there was a delay for the image acquisition so that the effective frame rate in the described experiments was 185 Hz.

The distance of the camera from the light sheet was about 50 cm, and most of the optical path was in the water. To minimise the distortion of the optical path, a water filled optical adapter was glued on the channel wall. This corrected for some of the distortion reducing the blurring and permitted the camera to look through a plane window.

The camera was tilted horizontally to reduce occlusion effects from waves. This angle was 5–10°. Thus, the upper part of the captured image is a total reflection on the surface. If the surface is not distorted by waves and is flat, the reflection is a mirror image of what is seen below the surface. An example of this is shown in Fig. 4.2. At $z = 0$ a dark horizontal line indicates the surface because here oxygen penetrates the surface and a higher concentration in the boundary layer lowers the luminescence intensity by quenching.

The presented method is most powerful without waves. Waves lead to occlusions of the surface when observed from the side. Higher waves would also move the surface out of the frame that is pictured by the measurement camera. And enlarging the imaged area decreases the resolution. Between these two factors an optimum has to be found.

Surfactants suppress the generation of waves with wind speed up to sev-eral meters per second. They also effect the gas exchange between air and water. Biological surfactants as from phytoplankton are important in a natu-ral environment [FREW et al., 1990] and the effect of surface films have been of interest in several studies [FREW et al., 1995; FREW, 1997].

In most experiments in the circular channel, one or two drops of stearic acid with the systematic name of octadecanoic acid were applied on the water surface as a surfactant to generate a stagnant film.
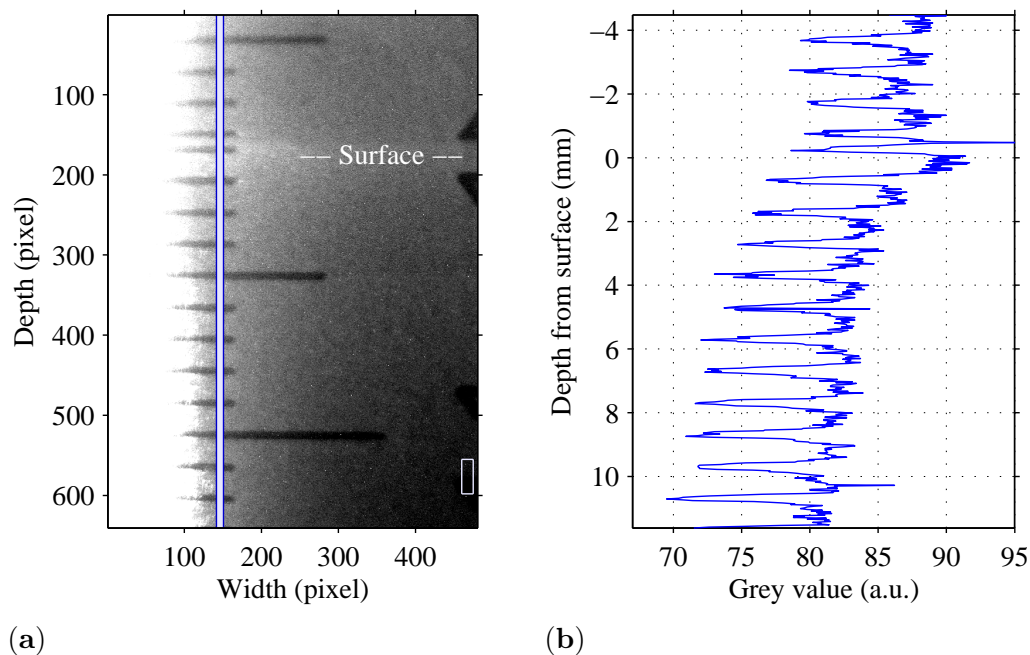
Figure 4.3: Image for spatial calibration of a millimetre scale. (**a**) Above the
surface at pixel 158 the total reflection is seen. A pixel resolution of
$25.2\pm0.2\,\mu\text{m/pixel}$ can be read off. (**b**) Mean of the 10 profile lines
marked in (a) to determine the pixel resolution

4.3   Spatial Calibration and Blurring

For the spatial pixel resolution a millimetre scale positioned at the laser sheet
in the water was captured with the camera in the experimental set-up. The
image is shown in Fig. 4.3.a.

The left side of the image shows a white area of saturation because of the
laser line illuminating the scale. This assures that the millimetre scale was
positioned in the plane of the laser sheet which is in the focal plane of the
camera optics.

To determine the pixel resolution, the distance of 437 pixel of 11 scale
marks with a distance of 1 mm was taken. With this the distance from one
pixel to the next is $25.2\pm0.2\,\mu\text{m/pixel}$. To visualise the scale marks, a mean
grey value of 10 lines, that are highlighted in Fig. 4.3.a, is shown in Fig. 4.3.b.

The surface in Fig. 4.3 is the middle between the longer scale marks. The
reflection of the water surface in the upper part of the image is bent near the
phase boundary by the scale dipping into the water. Because of this effect,
the marks near the surface appear distorted.

The edges of the marks are not sharp. This is a property of the optical
path quality that can be explained by the oblique course of the light passing
different materials and by the high magnification. During the evaluation of

the data the importance of knowing the extend of blurring became apparent.

To assess the extend of blurring, an edge in the image of Fig. 4.3.a was selected. It is the the area marked with a box at the right bottom in the image. In Fig. 4.4.a this area is zoomed. In Fig. 4.4.b a model function was fitted to a mean of the 16 rows. The model consisted of a box function with the mean values of the darker part and of the brighter part. To consider the blurring, a convolution of this function with a blurring function was done that was assumed to be the one-dimensional point spread function (PSF) of the optical system.

For this blurring, a GAUSS normal probability curve (Gaussian) f_b was assumed and the variance σ_{blurr}^2 was taken as a measure of the extend of the blurring:

$$f_b(x) = N_{\text{Norm}} \ \exp\left(-\frac{x^2}{2\sigma_{\text{blur}}{}^2}\right) \qquad (4.1)$$

The normalisation factor N_{Norm} was chosen as the sum of all values so that a convolution with this function does not change the mean grey value.

(a)   (b)   (c)
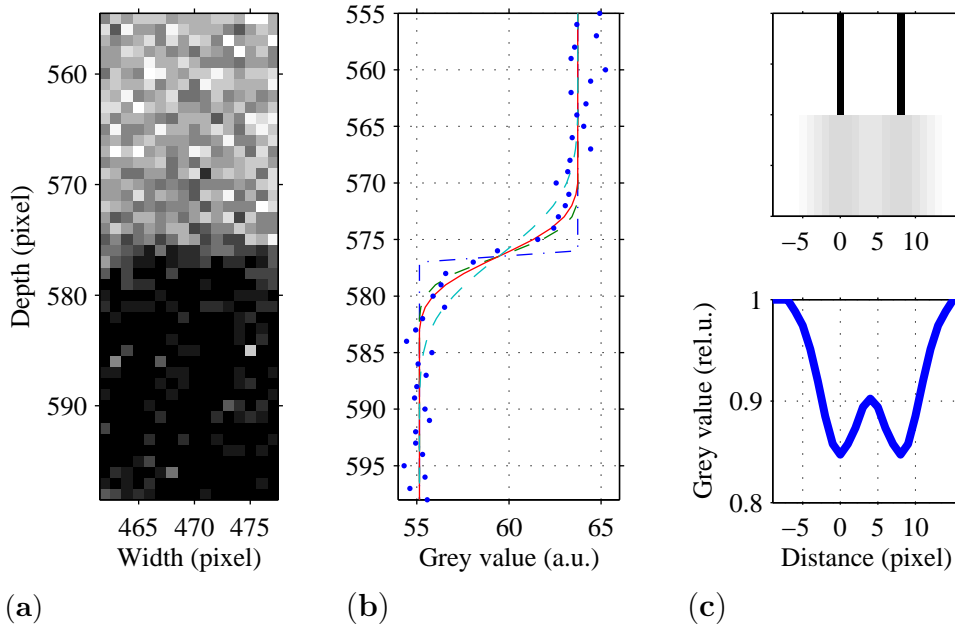
Figure 4.4: Estimating the extend of blurring in the optical path. (**a**) A detail of the image in Fig. 4.3.a. Taking the mean of all 16 rows reduces the noise. (**b**) The mean row (*dots*) can be compared to a a box model (*dash–dotted line*) convoluted with different blurring functions. The convolution with a Gaussian of $\sigma_{\text{blur}}^2 = 7$ (*solid line*) fits best. (**c**) Effect of the blurring on the grey value: two lines with the distance of 8 pixel before and after convolution with the blurring function

The resulting function from convolution of the box model with the Gaussian was fitted to the averaged measured rows and σ^2_{blur} was varied. The fit with $\sigma^2_{\text{blur}} = 7$ yields the lowest residual difference between the measured points and the model function. This means that after 4 pixel the intensity goes down to less than $1/e$. In Fig. 4.4.b also convoluted functions with $\sigma^2_{\text{blur}} = 4$ and 20 are plotted with *broken lines* for comparison.

The value $\sigma^2_{\text{blur}} = 7$ is the upper limit of the blurring because not all the assumptions will be fulfilled that the black mark on the scale is printed with a sharp edge, that this edge is ideally projected in the middle between two pixels and that the camera is perfectly parallel to this edge excluding smoothing by averaging.

In Fig. 4.4.c the effect of the blurring is demonstrated. A measure of the optical resolution is the minimum of the distance where two lines can be distinguished. After convolution with a Gaussian with $\sigma^2_{\text{blur}} = 7$ this distance is 8 pixels. With the pixel resolution of $25.2\,\mu m$, this results in a effective optical resolution of about $200\,\mu m$. But with noise the distance can grow.
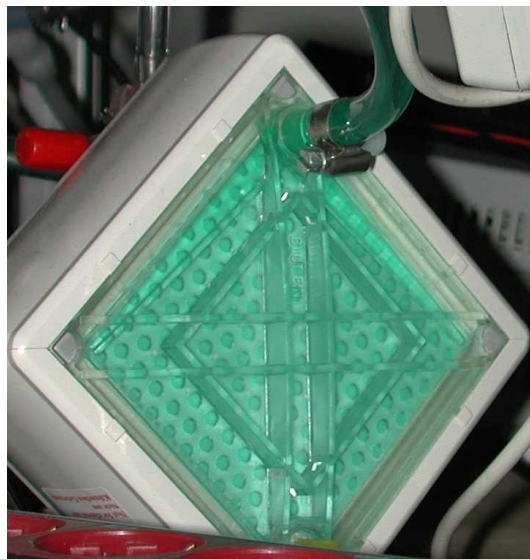
Figure 4.5: Photograph of the "Jostra Quadrox" gas-exchanger module from Maquet. It was used to lower the concentration of oxygen in the water bulk

4.4   Varying the Bulk Concentration

In order to strip dissolved oxygen from the water, a "Jostra Quadrox" gas-exchanger module from Maquet is installed (see Fig. 4.5) in a volume of $20 \times 20 \times 5\,\text{cm}^2$. It contains membrane capillaries with a total membrane

surface of $1.8\,m^2$ and a water volume of $250\,ml$. These small capillaries have micro perforations that are permeable only for gas molecules while liquids are held back. The device is normally used in cardio–pulmonary machines to load blood with oxygen and extract carbon dioxide. The gas exchanger can be used for other gases as well [Vogel, 2006].
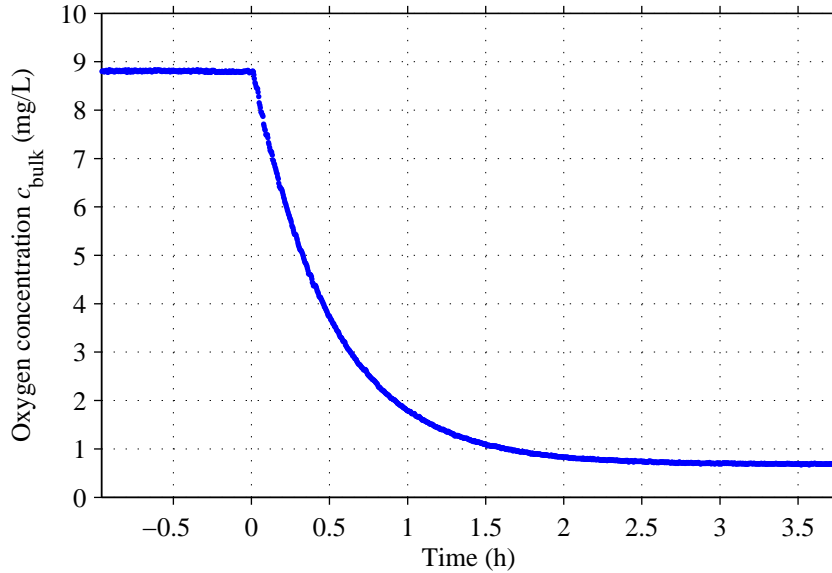
Figure 4.6: Decrease of oxygen concentration during degassing with the gas-exchanger module.

In the work described herein the gas exchanger was employed with a vacuum of $60\,mbar$ to degas the water to oxygen concentrations lower than $0.8\,mg/L$ as it is seen in Fig. 4.6.

Water was pumped through the module with a flux of $14\,L/min$, so that the concentration in the wind–wave flume decreased from approximately $8.8\,mg/L$ to $0.83\,mg/L$ after 3 hours as is seen in Fig. 4.6. The starting concentration was higher than the equilibrium concentration of $8.3\,mg/L$ because at the beginning of this measurement the gas-exchanger module worked with a sightly elevated pressure from a gas generator. At higher pressure the partial pressure of oxygen in water is higher than at ambient pressure. The gas generator stripped CO_2 and H_2O from ambient air and was used to assure a sufficient air flux in the gas exchanger.

4.5   Controlling the Wind Speed

In the experiments with wind, the speed of the wind paddles was varied by controlling a power supply with a PC. The computer gathered information on the wind speed and raised the current if the mean wind speed was too

low and lowered it if the wind speed was too high. Wind measurements are shown in Fig. 4.7.a.

In experiments with parallel measurements of gas-exchange rates of trace gases, the wind speed was increased after 30 min. When only oxygen was measured, the wind speed was changed after 20 min. Shortening the exchange times increases the contrast in the boundary layer because with time the oxygen concentration in the water bulk increases and so the intensity of phosphorescence decreases.

(a)

(b)
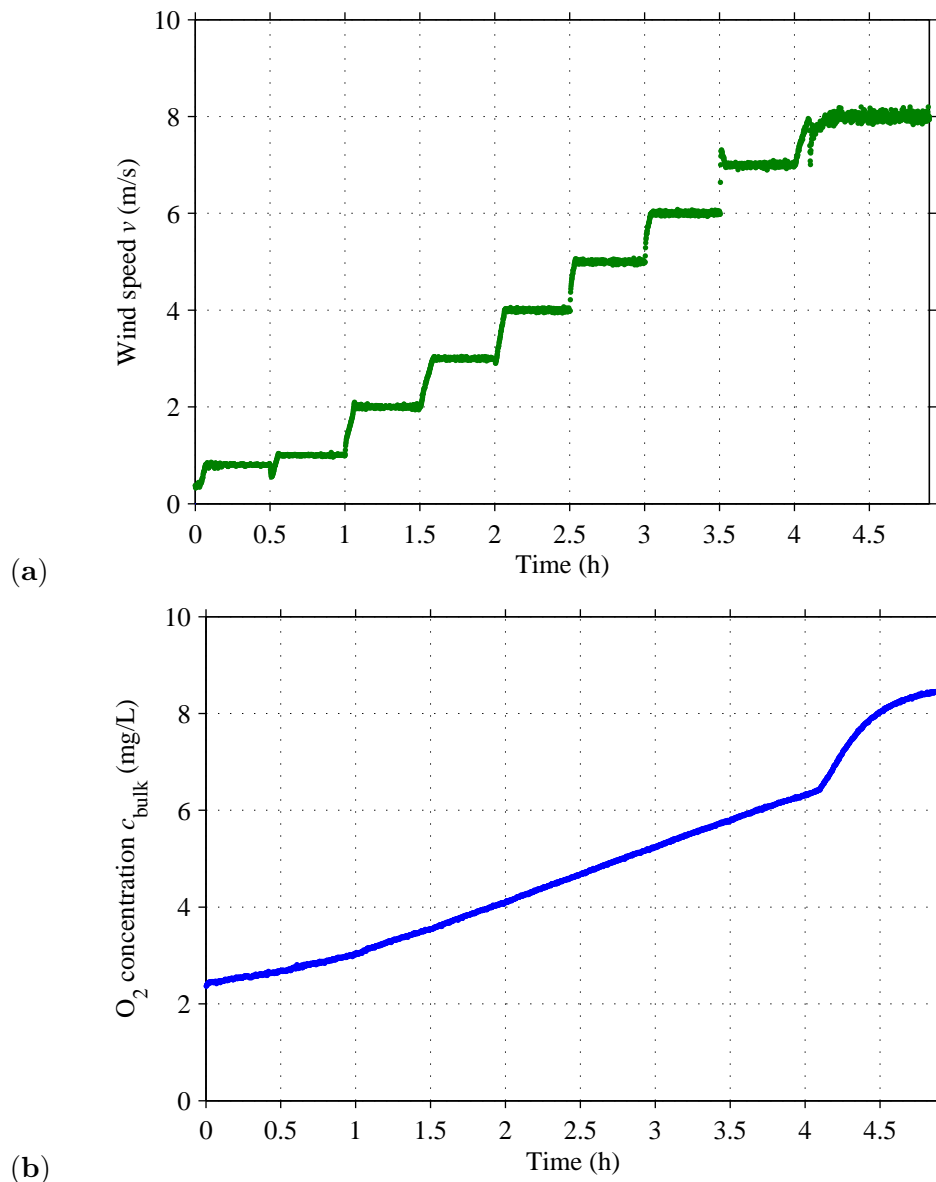
Figure 4.7: Typical development of the wind speed in an experiment. (**a**) The wind changed after a fixed time of 30 min. (**b**) Correlated to the wind speed was the increase of bulk oxygen concentration

In this experiment a surfactant forced a smooth surface. At wind speed higher than 7 m/s the surface film breaks what can be seen in the plot after 4 hours. In a first moment the wind energy is transformed into wave energy and the speed slowed down. It takes some time to adjust the current to achieve the maximum wind speed of almost 8 m/s.

In Fig. 4.7.b the parallel development of the oxygen concentration with the wind speed is displayed. With increasing wind speed the slope of the oxygen curve rises. When the surface film breaks, waves are generated and the gas exchange is enhanced dramatically.

Chapter 5

Methods: Evaluation of Image Series
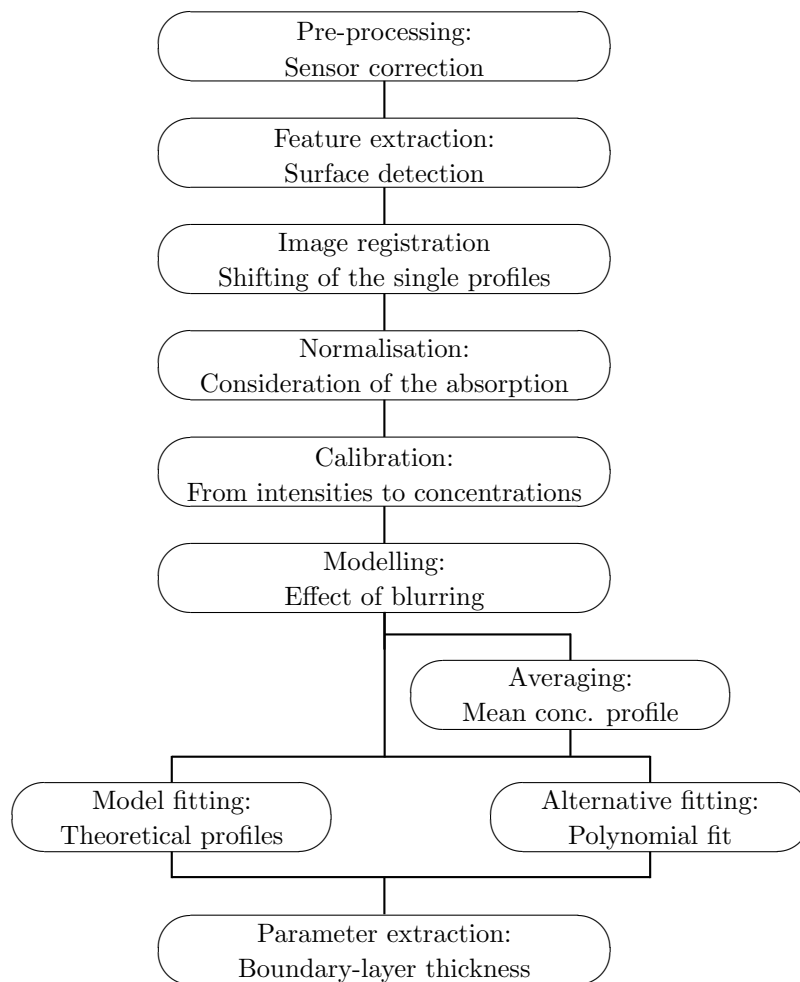
Figure 5.1: Flow chart of the image processing steps: from raw image data of luminescence intensity to concentration profiles and the boundary-layer thickness

5.1   Pre-processing: Sensor Corrections

The data acquired by the CCD chip of a digital camera has little offset for that negative values are not possible. To account for this offset, a dark image has to be subtracted from the acquired images.

Before any experiment a dark sequence of 5000 images was captured under the same conditions as during the experiment but without the laser light. This was done by blocking the laser beam. Averaging one column in time results in a noisy dark image line like the one shown in Fig. 5.2. The influence of surrounding light was low because of the small integration time at a frame rate of $185\,\text{Hz}$.
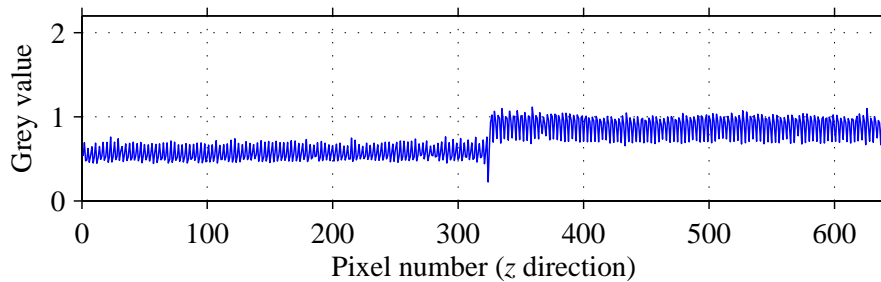
Figure 5.2: A mean column of a sequence of dark images. The two different parts of the chip show a little different offset. The z-direction is the depth

The built-in CCD chip in the Dragonfly-Express camera, that was used for all measurements, consisted of two independent fields that showed a little shift between these areas, and at the interface additional intensity differences were seen. Especially in low light conditions it was important to correct for this effect. Thus, the first step of the evaluation was to subtract the dark line from every measured line. The dynamic sensitivity of the chip shows a similar structure originating from the two parts but it was not corrected. Is has an observable effect when luminescence is low at high oxygen bulk concentrations as in Fig. 6.3 at high measurement numbers where the luminescent signal is low.

5.2   Detection of the Surface

The position of the free water surface in a depth profile moves between images and in most cases also from line to line. The motion is caused by waves, vibrations or agitation. For the evaluation of luminescence intensity profiles the shift of the surface position has to be taken into account.

A helpful feature in the images is that in invasion experiments of oxygen the luminescence in the boundary layer decreases and that this structure is

mirrored by total reflection at the surface what is seen in the example image of Fig. 4.2. This feature and its symmetry is used for the automatic surface detection in this thesis.

Difficulties in estimating the position of the surface arise from other factors than the concentration that can alter the light intensity. For high frame rates the signal-to-noise ratios get low. Another factor is that reflections on the surface may be disturbed by a rough surface and show very low intensity far from the surface. Or passing waves lead to occlusions and no surface can be seen at all. Also, in surface-renewal events the lowest concentration can be found below the surface.

In the literature some solutions of the problem of surface detection were developed. VARIANO and COWEN [2007] decided by eye where the surface in every image was. The surface appeared brighter because of the reflection of floating particles. A drawback of this tedious work is that some bigger particles give some reflections also when they are only near the laser sheet.

Also a second camera looking at the surface from a position slightly above the interface level can be used. The method was presented by BANNER and PEIRSON [1998] and applied for some LIF measurements by VARIANO and COWEN [2007]. In the upper camera the surface is clearly seen as the end of the light sheet because there are no interfering reflections. The images of the two cameras have to be spatially correlated and synchronised in time.

Another method uses the fact that the highest concentration of oxygen is normally found at the surface and the luminescence shows a local minimum at the surface. But the intensity drops also with the depth because of the absorption by the dye and because of some other effects mentioned above.

MÜNSTERER [1996] compared this local minimum method to other methods regarding their sensibility to noise as shown in Fig. 5.3. He modelled a depth profile and added different levels of random noise resulting in ratios of the surface signal to the noise. Then the different methods of surface detection were applied and the difference between the detected surface position and the input of the model was computed as a standard deviation σ_{err}. The deviations are all relatively small because the symmetry is not very sensitive to noise.

Different convolution kernels are studied for the use as symmetry filters in order to find the feature of the symmetry produced by a total reflection. The simplest point symmetric filter consists of a constant positive value on one side and a constant negative value of the same magnitude on the other side. For filtering a convolution of the filter mask and the measured depth profile is done. Near a point of high symmetry the filtered signal passes through a region of large local asymmetry and gives a large value. At a point of high symmetry the filter has a zero crossing. This box-symmetry filter may have

(**a**)

(**b**)
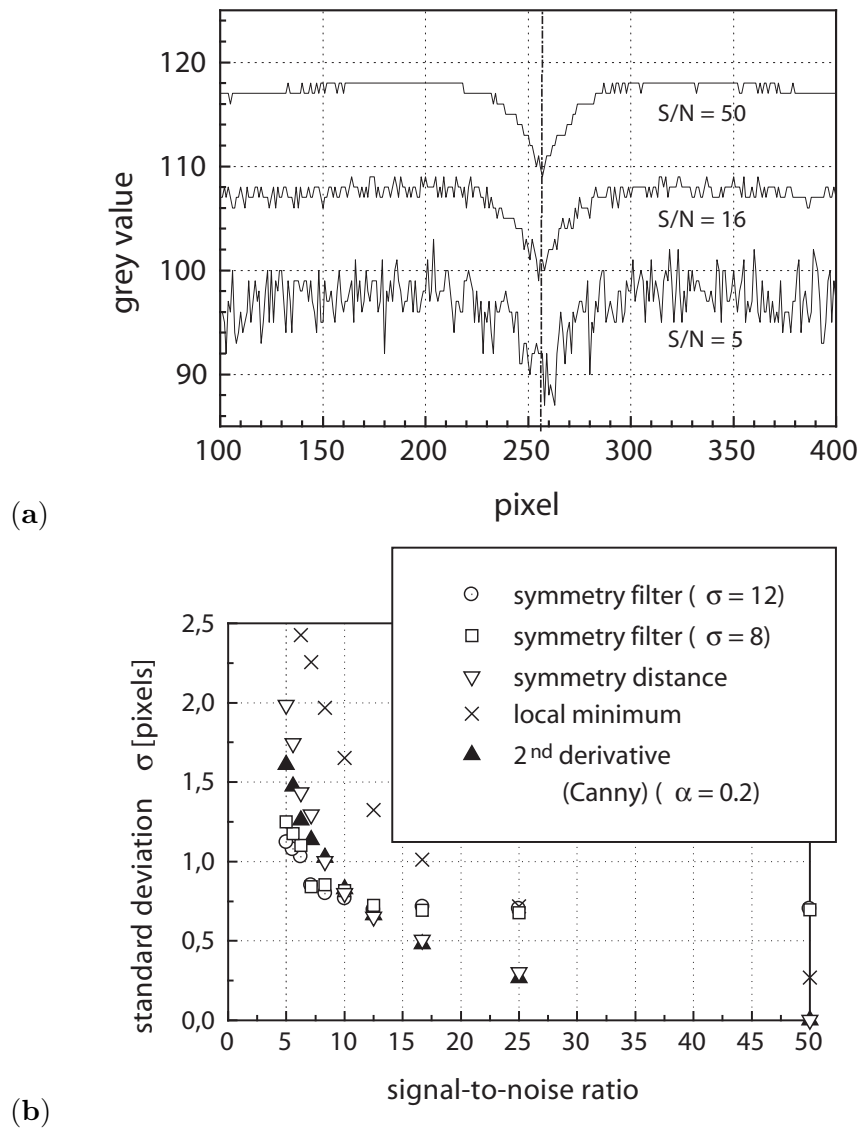
Figure 5.3: Effect of noise for different symmetry filters (**a**) Three modelled profiles with different signal-to-noise ratios. (**b**) Deviations from the correct symmetry point for different methods depending on the noise (From MÜNSTERER [1996])

a similar negative behaviour to noise as a box filter. The reception of noise is shown in Fig. 5.3.b.

In the same figure also a measure of the symmetry distance is found. This computation intensive method is based on the distance of the measured data points to a perfectly symmetric curve. The accuracy at high noise levels is not very good.

MÜNSTERER [1996] stated that a symmetry filter that consists of a binomial filter (also Gaussian filter, further reading in JÄHNE [2005]) that is inverted at the centre worked better as the box-like symmetry filter. The binomial filter has the same form as was used as a blurring function in Eq. 4.1. The shape of the binomial symmetry filter and of the box-symmetry filter is found in Fig. 5.4.c.
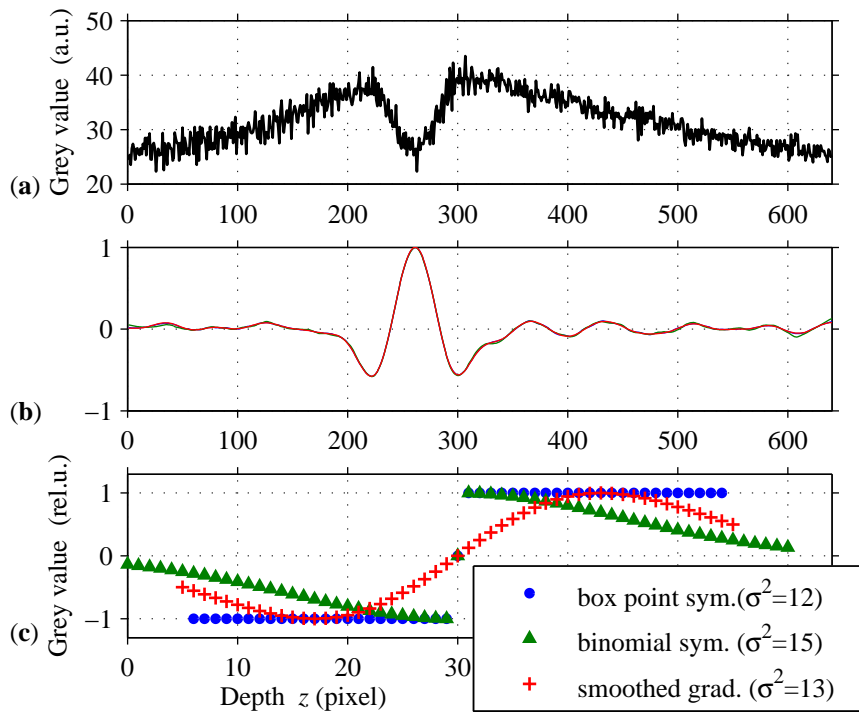
Figure 5.4: Effect of three different filters on the surface detection. (**a**) Example of a measured profile. Left side is the reflection of the right side. (**b**) Filtered profile. The effects of the filter masks on the example are very similar. (**c**) Different masks for filtering. (For the box-symmetry filter, σ_{filt}^2 is quarter of the length.) The mask was convoluted twice with the profile. The maximum gives the surface

The binomial symmetry filter is compared to two similar filters. Because of the symmetry the gradient of the intensity should change the sign at the surface. The convolution of the simplest gradient filter ($[-1\ 0\ 1]$) would detect no edges but only noise. Making the mask larger corresponds to the

symmetry filter discussed above. Another possibility is to suppress the noise first by a binomial filter and then apply the small gradient filter. The shape of a combined binomial smoothing and the tree-element gradient mask is shown in Fig. 5.4 with the name smoothed gradient filter.

To detect the correct zero crossing, the symmetry filter or the gradient filter was applied twice detecting the surface at the maximum of the filtered signal. For the gradient filter this corresponds to the second derivative. By spline interpolation of five pixels around the maximum even a sub-pixel accuracy of the surface detection can be achieved. But considering the accuracy of the detection and also the difficulty in shifting the noisy profiles by less than a pixel, only rounded integers were allowed for shifting.

The size of the mask can be optimised for the specific task of finding the symmetry in a measured profile by looking at the signal-to-noise ratio after applying the filter. Here the signal is the global maximum of the second derivative and the noise is every local maximum that is not the surface. The optimisation is demonstrated in Fig. 5.5 for three filter types.
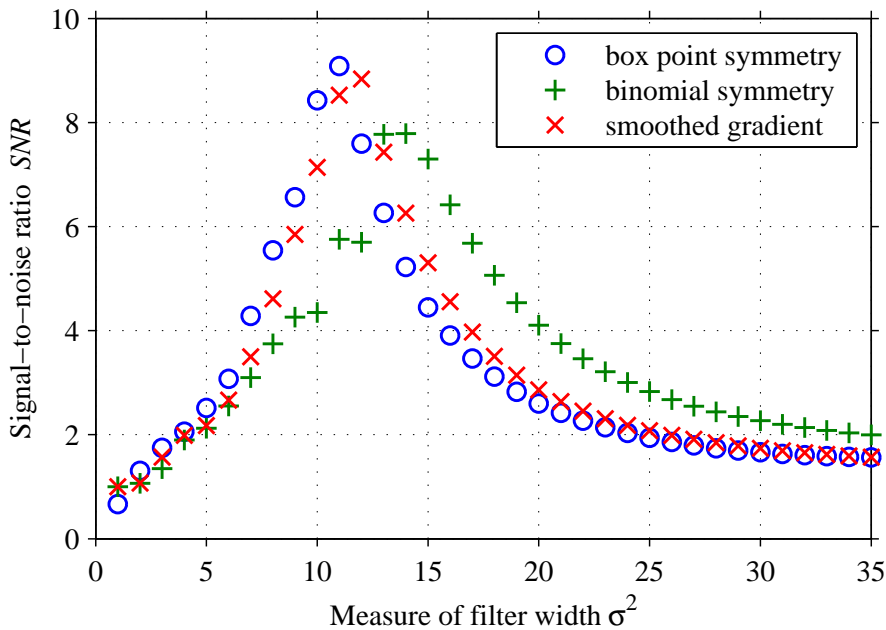
Figure 5.5: Filter optimisation: selection of the suitable filter width for surface detection shown in Fig. 5.4. N.B.: The signal of SNR is the maximum of the filtered signal at the right surface position while the noise is the a secondary peak leading to wrong detections

When the filter is too narrow the noise creates local maxima that are not desired. For wide filters, the characteristic feature, that is to be detected, is smeared out. The optimum for this task was around $\sigma_{\text{filt}}^2 = 13$. The name of σ_{filt}^2 is used for analogy to the filters using a Gaussian also for the box-

symmetry filter but it is simply the quarter of the total length of the mask. The optimum length of $\sigma^2_{\text{filt}} = 12$ of the box-symmetry filter was used for the further evaluation. This length worked best for the critical detection with thin boundary layers.

In Fig. 5.4.b the effect of the convolution of a measured profile with the three different convolution kernels is shown. After optimising the length of every filter, no preference for a certain filter type was found.

A measured depth profile is shown in Fig. 5.6.a. Taking the mean of the lines without any surface detection leads to an additional blurring. After the surface is detected, the lines can be arranged to put the surface at the same pixel position and then the lines can be averaged. This is shown in Fig. 5.6.b. After this image registration and averaging, also a little dip is visible at the surface originating from particles floating on the surface giving high reflection intensities. This shows that the optical resolution is good enough to see effects of the surface.
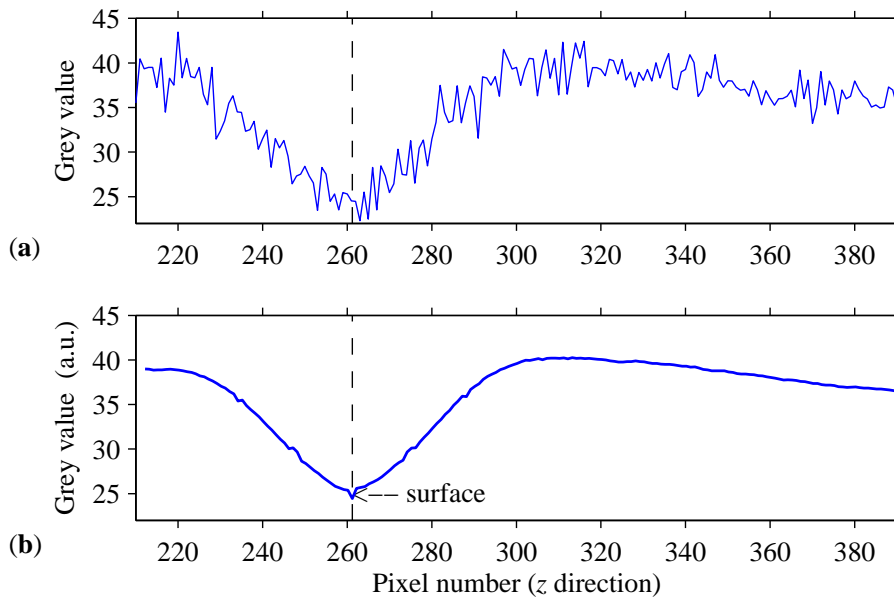
Figure 5.6: (**a**) Profile. Left side is the reflection of the right side. (**b**) Mean after surface detection and image registration. N.B.: no smoothing was done on the displayed profiles

5.3   Consideration of Absorption

After the surface is found, the profile of light intensity can be corrected for the absorption of the dye. If the exciting laser light is coming from above the surface, the laser-light intensity in a certain depth is lower because it has

been absorbed partially by the dye in the water layer above. Consequently, also the luminescent emission gets lower.

The effect of this decrease is seen in the right of Fig. 5.6.b and it can be calculated with the BEER–LAMBERT's law of Eq. 3.4. In the evaluation an empirical exponential was fitted to the profile disregarding the first 100 pixel from the detected surface where the oxygen quenching occurs.

$$I = a_A \exp(-\frac{z}{l_p}) + b_A \tag{5.1}$$

The penetration depth l_p was established as 900 pixel. With the scaling factor $f_{sc} = 25.2\,\mu m/pixel$ this is 22.7 mm. This was taken for all measurements with the same dye concentration. The other two parameters, the factor a_A and an offset b_A, were fitted for every line because the absolute intensity was fluctuating and some scattered light was not affected by absorption.

For a measured profile this normalisation takes the form as shown in Fig. 5.7. The relative intensity of phosphorescence is one for gas concentrations that are the same as the oxygen concentration in the bulk. Near the surface the intensity decreases because a higher concentration of the quenching oxygen that penetrates the water surface. A measure of quality of this normalisation step is a constant baseline in some distance from the water surface where no turbulence structures are expected.
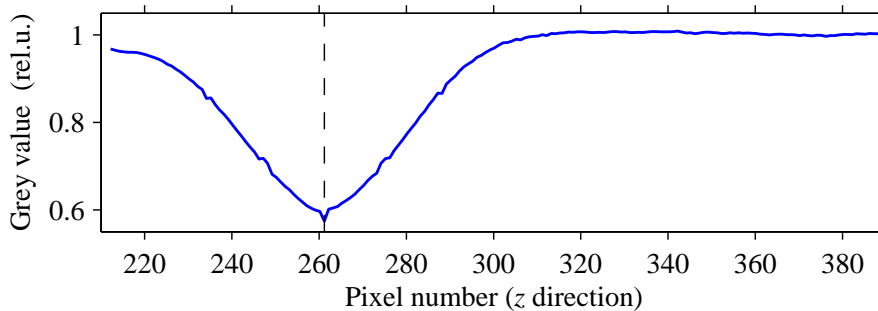
Figure 5.7: Mean profile normalised to BEER–LAMBERT absorption shows a constant baseline far from the water surface (on the right)

5.4 Calculate Concentrations from Luminescence Intensity

The relation between concentration of a quencher like oxygen and the intensity of luminescence is described by the STERN–VOLMER equation of Eq. 3.3:

$$\frac{I}{I_0} = \frac{1}{1 + K_{SV}[O_2]}$$

For small differences in concentration, a linear approximation of this relation is justified. In this case, the normalised intensities can be taken directly to compute normalised concentrations as it was done in FALKENROTH et al. [2007].

To establish a more accurate relation between intensity and local oxygen concentration over a wide range of concentrations from 0.8–8 mg/L, several calibration curves were measured. A typical graph is shown in Fig. 5.8.
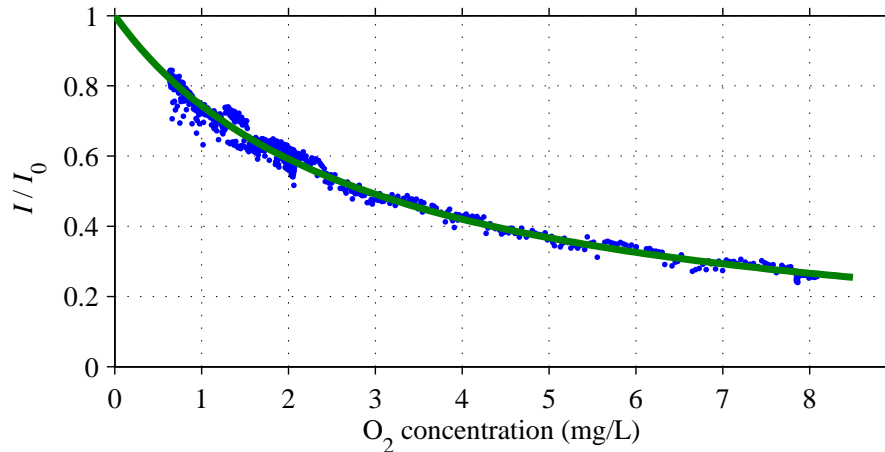
Figure 5.8: Calibration curve: effect of quenching for different O_2 concentrations. The quenching constant was measured to be $11\,000\,\frac{1}{M}$

The sole parameter of the fitted curve is the quenching constant K_{SV} and is was calculated to be $11\,000 \pm 2000\,L/mol = 0.345 \pm 0.063\,L/mg$.

The calibration loses accuracy for a fluctuating laser light because of effects like occlusions by the spinning wind paddles or reflection and refraction at the free water surface. Also the calibration of the oxygen probe was not stable between different measuring days. In addition, renewal events altered the intensity of the luminescence in the reference depth during the calibration measurement. They were caused by the bulk turbulence generated by the pump of the gas exchanger. However, using the curvature of the calibration function is nevertheless appropriate.

The calibration procedure can be omitted when using other dyes like the ones that were used previously for the visualisation of the water-boundary layer. The quenching constant of PBA is much smaller and so the curvature of the calibration curve can be neglected. Using pH-indicators, a pH range is selected where the intensity of the fluorescence is linear with the pH value. But to get to the molecular concentration of the acid or base, the logarithmic scale of the pH must be considered.

Applying the above calibration on the measured data, the problem of the fluctuating laser intensity in the water emerges. This can be handled

by normalising the intensity far from the surface to the intensity that is expected at the concentration that is measured at the same time with the oxygen probe sensor. The assumption here is that in the mean of several pixel and far from the surface, the concentration is equivalent to the bulk concentration. The resulting mean concentration profile is shown in Fig. 5.10. After this calibration procedure the effect of fluctuating incident light has no influence on the signal any more.

5.5   Effect of Blurring

The surface is not imaged as a sharp discontinuity because of the limited quality of the optical path of the luminescence reaching the camera. The image is blurred. This effect is a problem for the determination of surface concentration and its gradient and also the boundary-layer thickness.

A homogeneous blurring can be described as a convolution of the real profile with a blurring function. In digital image processing this function is called the point spread function (PSF).

In this work a Gaussian as described in Eq. 4.1 with a variance $\sigma_{\mathrm{blur}}^2 = 7$ was assumed for the blurring function (for the determination of the extend of blurring, see Sec. 4.3). As the optical path for the described experimental set-up was kept stable, the same function was used for the evaluation of all images taken. The effect on a modelled profile is shown in Fig. 5.9.
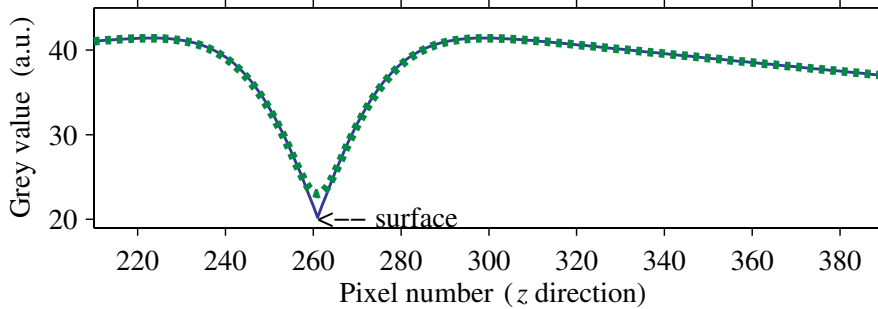
Figure 5.9: Effect of blurring on a model function: the smoothing of a modelled curve is evident at the sharp edge of the surface

5.6   Fitting a Model to Measured Profiles

The increase of the oxygen concentration near the surface can be described with the appropriate model following the theoretical profile as illustrated in Sec. 2.2. Considering the mirror effect at the surface and with the convolution

with the blurring function, a model function is designed that depends on only two parameters: an depth scaling parameter $z_{\star m}$ describing the boundary-layer thickness and the concentration difference Δc_m between the surface $c_{surface,m}$ and the water bulk $c_{bulk,m}$ that is used to calculate the normalised concentration c_+. In invasion experiments the surface concentration can be lower than the concentration of the equilibrium with air because of a thin air-side boundary layer. The reference bulk concentration $c_{bulk,m}$ is the baseline of the concentration profile.

$$c_+ \;\; = \;\; \frac{c_m - c_{bulk,m}}{\Delta c_m} \tag{5.2}$$

This smoothed model function can be fitted to every single concentration profile from Sec. 5.4 to determine the parameters as demonstrated in Fig. 5.10 with the profile $p = 1$ of Eq. 2.31. In this procedure the residual difference between the measured data and the modelled function was minimised. The non linear least square algorithm implemented in the MatLab software made use of a subspace trust region method and the software documentation cites COLEMAN and LI [1996, 1994] for reference.
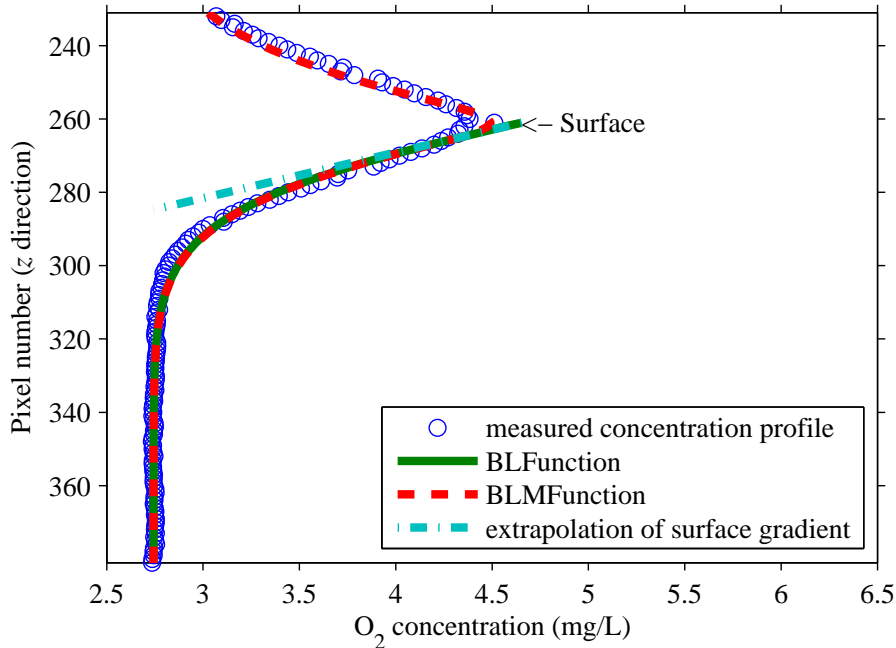
Figure 5.10: Extracting the boundary-layer thickness $z_\star$ with fitting method. BLFunction is the theoretical concentration profile without blurring. BLMFunction is the model function that was fitted to the data. The extrapolation of the concentration gradient at the surface yields $z_\star$.

Fitting is possible also with noisy data. Thus, no smoothing of this data is needed before this evaluation step. A smoother depth profile is obtained by averaging several lines. Both computations were carried out and compared.

The consideration of the blurring in the fitted model is especially important in cases when the extend of blurring is large.

Multiplying the parameter $z_{\star m}$ in the units of pixels with the scaling factor $f_{sc} = 25.2\,\mu m/pixel$ of the pixel resolution determined in Sec. 4.3 gives directly the boundary-layer thickness $z_\star$. According to Eq. 2.36, it is the inverse of the gradient of the normalised concentration c_+ at the surface determined by the flux that is present in the boundary layer in that moment derived in Sec. 2.2.

$$-\left.\frac{\partial c_+}{\partial z}\right|_{z=0} = -\frac{1}{z_\star}$$

From the slope of the concentration profile at the surface, the flux and thus the transfer velocity k can be calculated directly from Eq. 2.33 by knowing the diffusivity D_{ox} of oxygen at the measured temperature.

5.7   Polynomial Fit as Alternative

Fitting the model function to the measured data is a computationally expensive method for the evaluation. A much faster way to extract boundary-layer thickness $z_\star$ is to measure a thickness of the depth profile where the concentration reached a certain level.

The first unknown is the surface concentration. Because of the blurring the concentration is higher than directly calculated from the luminescence intensity in invasion experiments. If the extend of blurring is much smaller than the boundary-layer thickness, then the extrapolation of the maximal slope to the surface is a good guess. To estimate the value of the highest gradient a polynomial of order three was fitted to the measured values around the surface as seen in Fig. 5.11.

Now different distances from the surface can be extracted with corresponding levels of concentration. In the case of a smooth surface that behaves like a rigid wall, the concentration falls to a fraction of 0.24 of the surface concentration at the distance of the boundary-layer thickness $z_\star$ as shown in Sec. 2.3.

For a free surface, the concentration falls to $1/e$ of the surface concentration within the boundary-layer thickness assuming the classical surface-renewal model (cf. Eq. 2.35). When the profile follows an exponential function as claimed by the model, another way to extract the same distance from
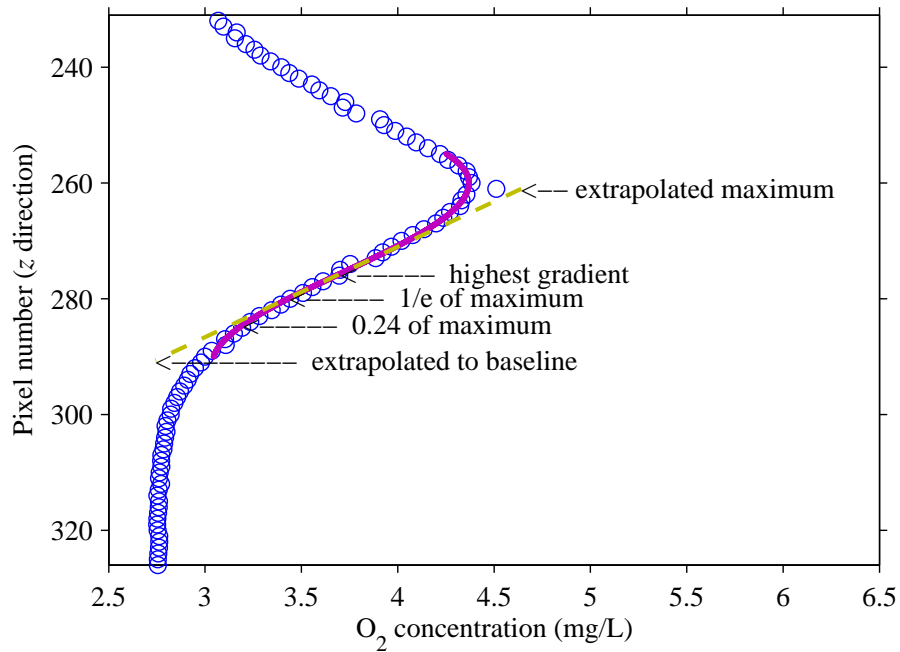
Figure 5.11: Extracting the boundary-layer thickness $z_\star$ with polynomial fit (*solid line*) to a measured depth profile (*circles*). The extrapolation (*broken line*) of the maximum slope of a polynomial fit function gives the extrapolated surface concentration. Depending on the assumed theoretical profile, the boundary-layer thickness $z_\star$ can be measured at different concentration levels

the surface is to extrapolate the slope at the surface to the baseline of the normalised bulk concentration level.

In Fig. 5.11 as in all evaluated profiles, the highest gradient of the concentration profile is near the $1/e$ concentration. Consequently, the distance at the extrapolation to the baseline is always higher than the distance at $1/e$ level.

Part III

Results and Discussions

Chapter 6

Results: Gas-Transfer Velocities and Depth Profiles

The image processing algorithm extracted the properties of gas exchange from the images in the boundary layer. Now, these parameters will be presented and discussed. Criteria for their quality will be developed and analysed. Systematic gas-exchange measurements with a smooth surface and different wind speeds are analysed. The assignment to one of the theories of turbulence introduced in Sec. 2.2 is the subject of the first part. Additionally, the developed tools were found to be applicable also to the study of turbulence structures generated by a mixing pump. Furthermore, few examples of concentration fields below a wavy surface revealed some interesting details. Finally, concentration fluctuations calculated for all three different external conditions are documented.

6.1 Smooth Surface Under Wind Stress

A main objective of this part is to find the correct theoretical model that describes best the measured concentration profile in the boundary layer during gas-exchange experiments with different wind speeds. First the concentration field is analysed. Because of the blurring, the concentration and its gradient can not be determined directly at the surface. In a second step, the model profile is fitted to the data with the method described in Sec. 5.6 and the error of the fit is analysed. The results suggest two candidates for the model to be the appropriate description of the measured mean profiles.

In the fitting procedure, the boundary-layer thickness is calculated in the mean profile and in every single profile. Both results are compared in Sec. 6.1.3 to the values calculated with the alternative method presented in Sec. 5.7 where a polynomial is fitted to the measured mean profile and the

data near the surface is reconstructed by extrapolation.

To decide about the actual transfer velocity, the values of the two model candidates are compared to mass-balance methods of oxygen bulk concentrations Sec. 6.1.4 and other gases in Sec. 6.1.5 determined in parallel measurements as a ground truth.

6.1.1   Analysis of Concentration Fields in the Boundary Layer

Measurements with a smooth surface were performed with a surfactant that suppressed the generation of wind waves. Augmenting the wind force, the gas-exchange rates increase without the generation of visible turbulence structures. The image processing steps described in Chap. 5 yield mean concentration profiles. 12 sequences of 5000 frames were taken for a single wind speed. After raising the wind speed, the imaging was stopped for more than 7 min to assure stabilisation of the wind field before taking the next series of images.

During the experiment the oxygen concentration increased in the way shown before in Fig. 4.7. It was not possible to keep the bulk concentration low with a working gas-exchanger module because its pump generated visible bulk turbulences that significantly increased the gas transfer at the surface. The influence of these turbulences and their structure will be studied in Sec. 6.2. With increasing bulk concentration the contrast of luminescence decreased what had a negative effect on the signal-to-noise ratio.

Fig. 6.1 shows time series of one vertical image line in the laser sheet observed with 185 Hz for 27 s giving 5000 frames. A typical image of the camera is seen in Fig. 4.2. The images shown here are taken after a constant wind speed was established for half an hour. The distance from the surface to the bottom of the image is approximately 10 mm. In the images the boundary layer is visible as a horizontal darkening and gets thinner with increasing wind speeds. Especially in Fig. 6.1.b periodic dark vertical lines are occlusions by the four wind paddles.
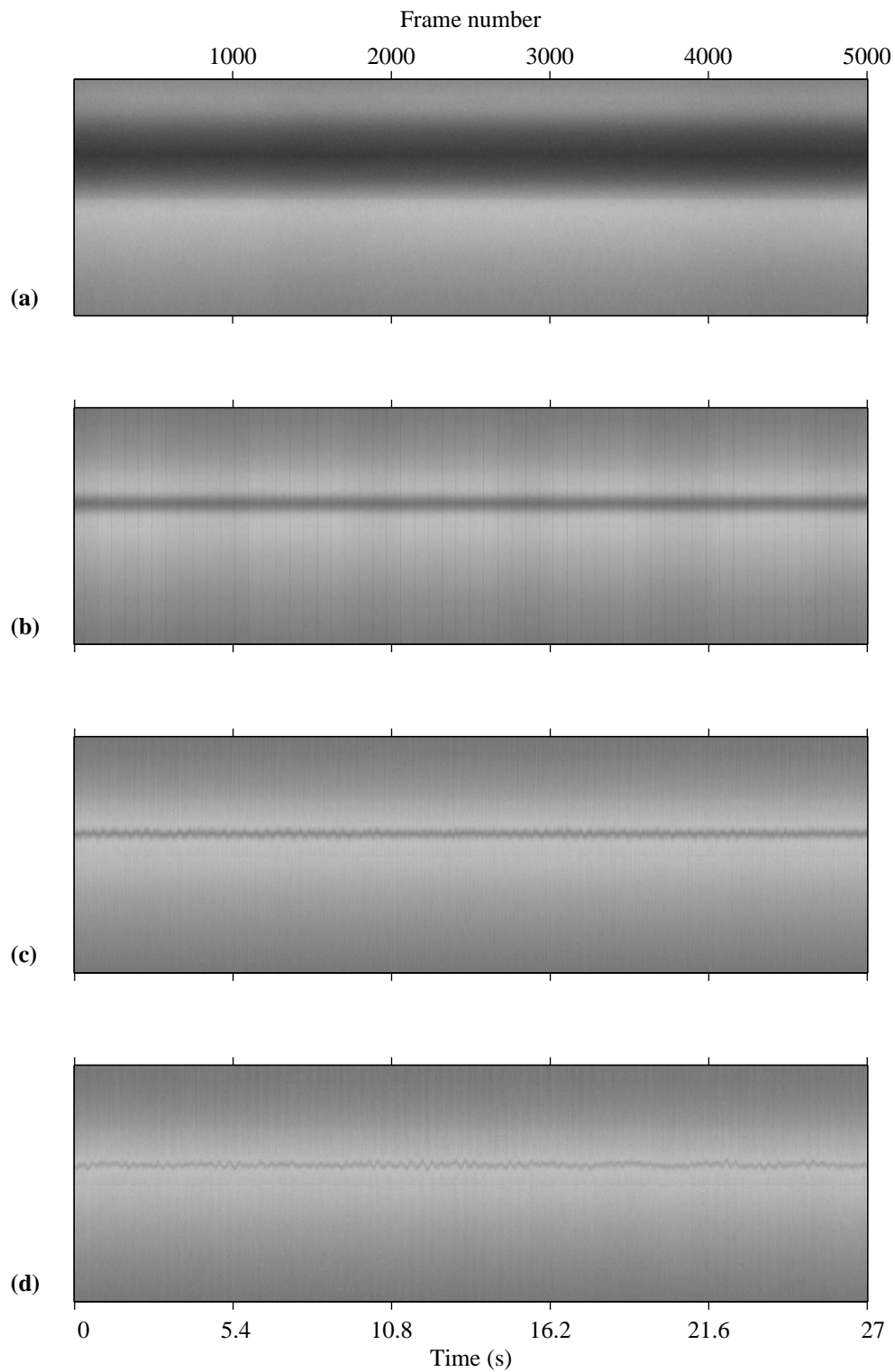
Figure 6.1: Raw time series of one vertical line (640 pixel) of the laser sheet. (**a**) 20 min after stopping the O_2-stripping pump and without wind. (**b**) Wind speed of 0.8 m/s. (**c**) 3 m/s. (**d**) 6 m/s. N.B: Above the dark surface a total reflection is seen in the images

From image series similar to the examples shown in Fig. 6.1, arbitrary single intensity profiles are shown in Fig. 6.2. The intensity decreases with increasing oxygen concentration what is seen as low intensity near the surface. Here oxygen penetrates the phase boundary. High oxygen concentrations are also seen as a lower signal at higher wind speeds because during the experiment with step wise increasing wind speeds, more and more oxygen gets solved in the water. This leads to a low contrast near the surface at high wind speeds.
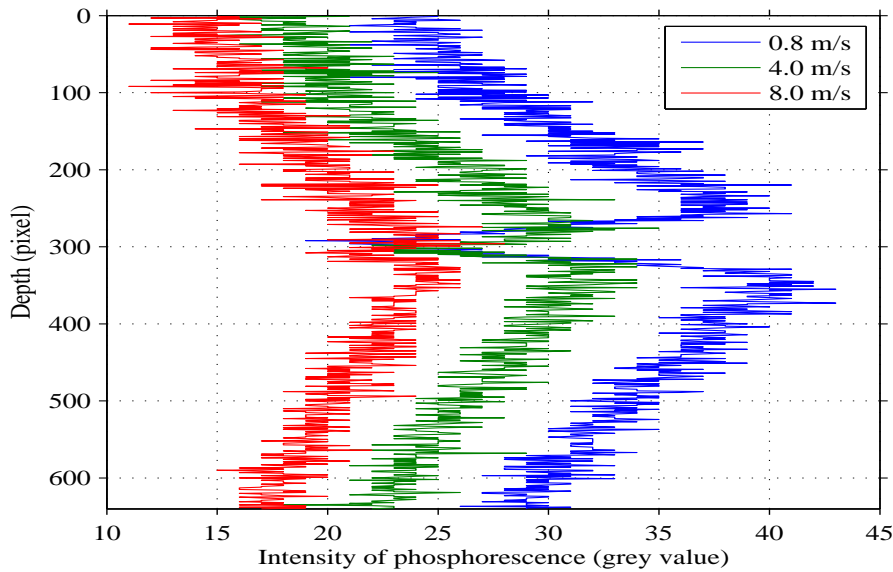
Figure 6.2: Single intensity profiles before image processing show the signal quality at the different wind speeds. The contrast at the surface at the position around 300 pixel decreases with higher bulk concentrations

From 5000 grames, a mean concentration profile is computed. The depth is displayed in Fig. 6.3 up to pixel number 256 including 50 pixel of the total reflection at the surface at negative depth. The bulk concentration increased stepwise because of the waiting time between the sequences.

The increase in concentration near the phase boundary is observed with a high spatial resolution of $25.2\,\mu m/pixel$. In this experiment the concentration at the surface is increasing with time. It may be explained by a thinner air–side boundary layer if this is not an artefact of the oxygen calibration.

A step in the bulk concentration level at the depth of about $1.6\,mm$ originates from an artefact of the camera chip described in Sec. 5.1. But in general the baseline of the concentration is stable what means that the correction for the Beer-Lambert absorption from Sec. 3.2 works fine.
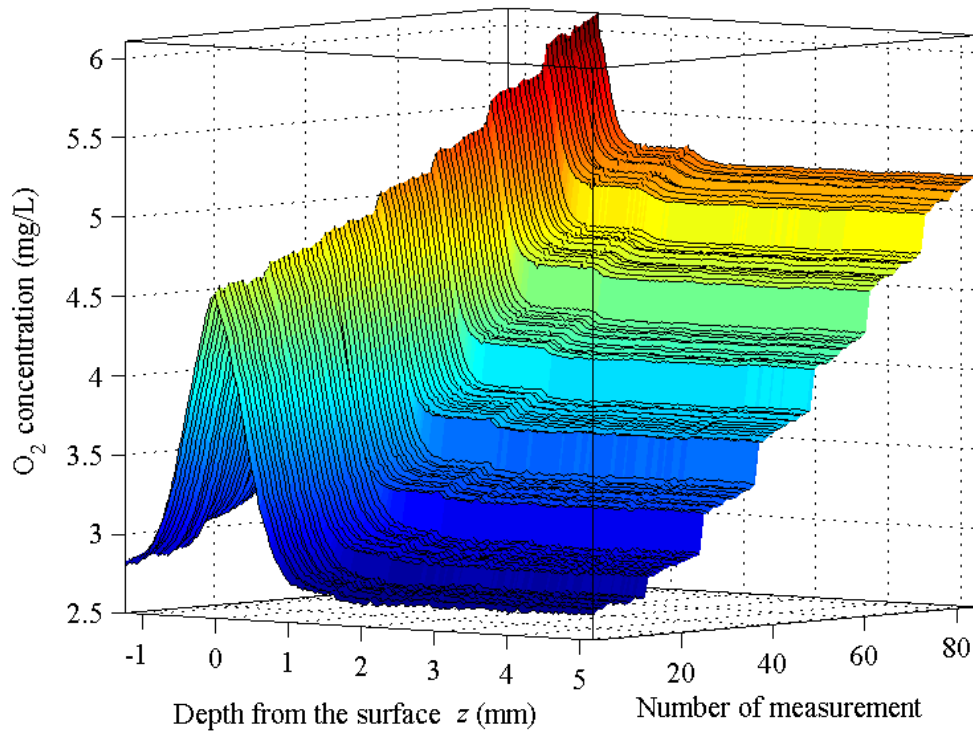
Figure 6.3: Mean concentration profiles of one measurement series with stepwise increased wind speed. The maximum of concentration is not the concentration at the surface because of the optical blurring

6.1.2   Concentration Profiles and Turbulence Models

With different assumptions about the turbulence structure, different concentration profiles in the boundary layer can be deduced from the theory discussed in Sec. 2.2. To decide which description has the dominant influence on the depth profiles seen in Fig. 6.3, the theoretical profiles were fitted to the normalised measured concentrations.

In Fig. 6.4.a the surface-renewal model with a smooth interface and $p = 1$ was assumed as the depth dependence of the turbulent diffusion. For comparison the other profiles discussed in Fig. 2.2 are plotted in the same graph with the normalisation from the fit with $p = 1$. It is clearly seen that the models with $m = 2$ or 3 and $p = 0$ are distant from the measured data. But the line with $m = 4$ from the K-model is also near the measured data.

This shows that in the case of a smooth surface it is very difficult to distinguish between the conceptual models by just analysing the depth profiles. To document the dangers of fitting the profiles, in Fig. 6.4.b the fit of the identical data was done to the model with $m = 4$. This graph suggests that this is the best fit to the model. A definite decision on the suitable model can

(**a**)

(**b**)
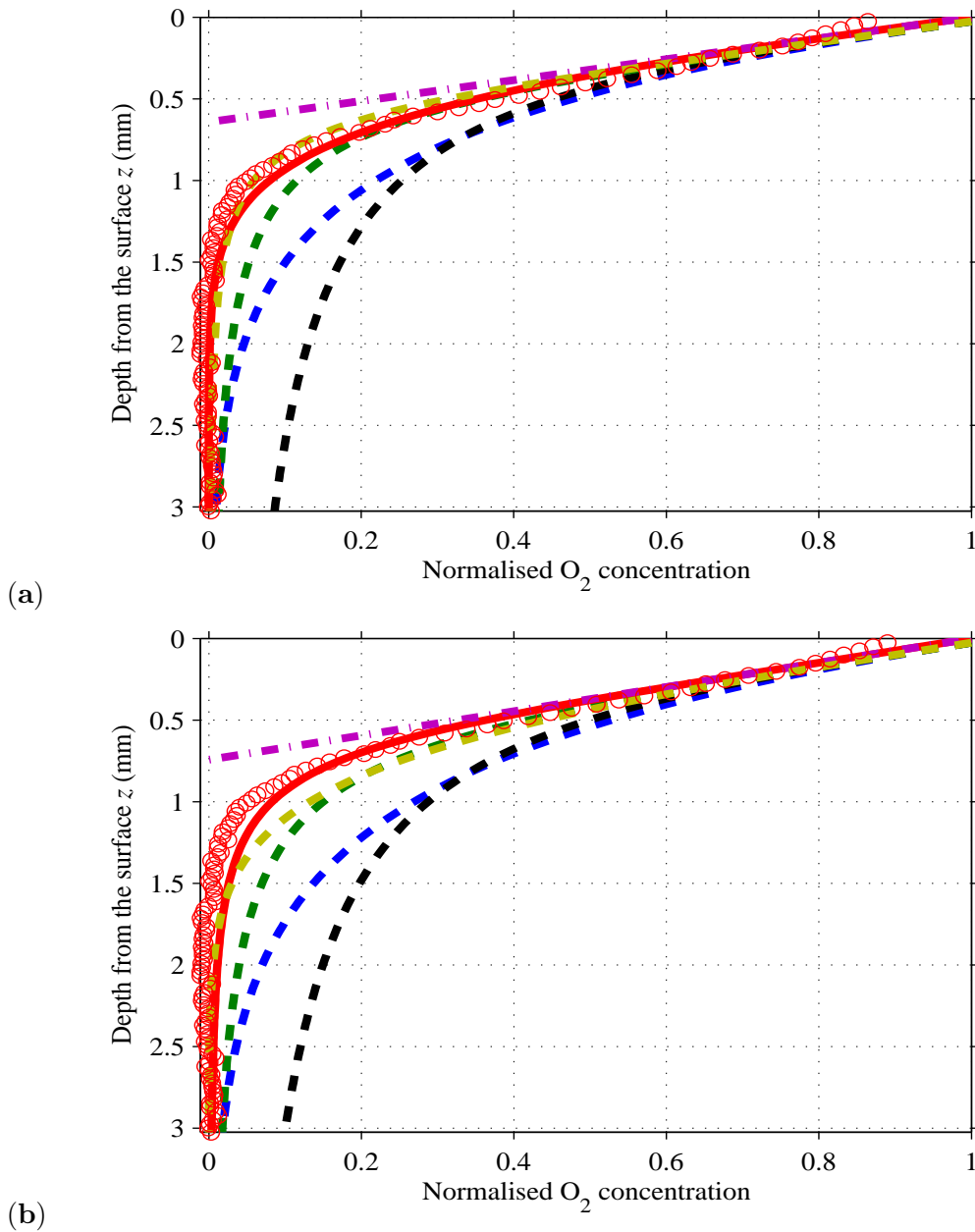
Figure 6.4: Analysing the form of a measured concentration profile (○) with
two different models. The wind speed was $1\,\mathrm{m/s}$ and the boundary-
layer thickness was $585\,\mathrm{\mu m}$. (**a**) The best model seems to be the
surface renewal with the rigid-wall-assumption ($p = 1$, *solid line*).
The other models of Fig. 2.2 are plotted for comparison (*broken lines*,
$m2$, $p0$, $m3$, $p1$, $m4$). The K-model $m = 4$ has a very similar form.
(**b**) The same measured profile can be analysed by fitting the K-
model ($m = 4$, *solid line*) to the data. Here it appears that only this
model is the best description of the profile. ($m2$, $p0$, $m3$, $p1$, $m4$)
The shape of a measured profile alone can not distinguish between
the models at a smooth interface

not be on the basis of a single mean profile. After fitting the other models with $m = 2$ or 3 and $p = 0$, they could be excluded clearly as adequate descriptions of the measured profile.

A better criterion for the decision of the best theoretical description than looking at only one fit could be to analyse the residual difference between the data and the fitted model for different conditions. Such a study is shown in the graph in Fig. 6.5.

A low value of standard deviation of error σ_{err} between the fitted model and the data signifies a good accordance. The best accordance between the fit and the data is seen for the model with $m = 4$, but the difference to $p = 1$ is not significant. For all models, the value of σ_{err} first decreases with higher wind speed. This is because the boundary layer gets thinner and the share of the fitted region is larger where the bulk concentration is a constant baseline. In this region the difference between a model and the data is naturally small without any information about the quality of the fit. But it is possible that secondary currents that are present in the water of circular wind–wave flumes at small turbulence states are also responsible for this tendency.
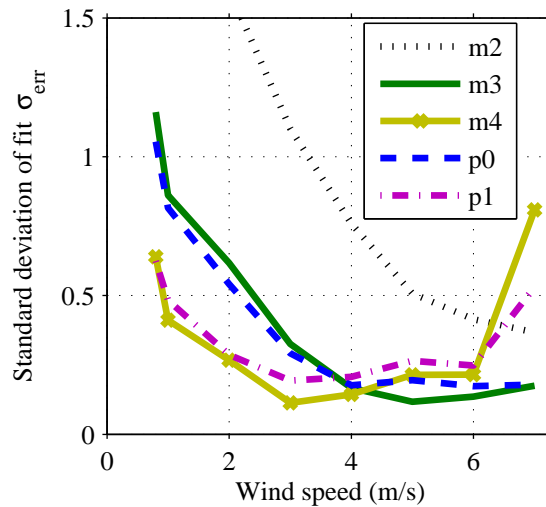
Figure 6.5: Error σ_{err} for different model-fits varying the wind speed. The data differs less from the model $p = 1$ than from $m = 4$, considering that the highest wind speed is subject to a low signal-to-noise ratio. The difference of the models is not significant enough to decide in favour of one of it

There are some explanations for the observation that σ_{err} increases with wind speeds higher than $5\,\mathrm{m/s}$. One is that the signal-to-noise ratio is lower for these measurement points because of the increased oxygen concentration in the bulk. Furthermore, due to the faster flux, a thinner boundary layer is more difficult to detect correctly with the given optical resolution. Another

reason may be that the effect of the step in the concentration baseline seen for $z > 1\,\text{mm}$ in Fig. 6.3 gets more influence.

A possible interpretation of the observation, that $m = 3$ becomes the model with the lowest error for high winds, is that for low wind speeds and high values of the boundary-layer thickness $z_\star$, the mechanism is different than for high wind forces with thin boundary layers. The experiments that were conducted may give a hint but do not allow a decision just from the shape of the concentration profile.

6.1.3   Comparison of Transfer Velocities from LIF-Measurements

In the fits in Fig. 6.4 also an extrapolation to the baseline of the bulk concentration is seen. This intersection gives the value of the boundary-layer thickness $z_\star$. It is the inverse of the gradient of the normalised concentration at the surface. According to Eq. 2.8 this parameter can be used to determine the gas-transfer velocity k:

$$k = \frac{D}{z_\star} \tag{6.1}$$

In this definition the molecular diffusivity D_{ox} has to be known. As it is a temperature dependent quantity, the water temperature during the experiment was kept constant and the change in the temperature range found in the experiments was smaller than 0.1°C.

For a wind speed of 0.8 m/s the thickness of the boundary layer $z_\star$ with the fitted profile of $p = 1$ is 25.8 pixel corresponding to 0.65 mm. With D_{ox} of 2.36 $10^{-5}\,\text{cm}^2/\text{s}$ at 25.1°C (from Mayer [1995]) the gas-transfer velocity k was 1.3 cm/h what is the expected value for a slow gas exchange with little turbulence at a smooth surface. The averaged values of 12 mean concentration profiles for every single wind speed are found in Fig. 6.6.

12 values are computed for every wind speed. The displayed values of the boundary-layer thickness $z_\star$ in Fig. 6.6 are always mean values. The displayed comparison demonstrates also that there is little difference between fitting the model and extrapolating the surface gradient, on the one side, and taking the distance where the normalised concentration has fallen to the value of 0.24 predicted by the same model as deduced theoretically in Sec. 2.3, on the other side. For this case of a smooth air–water interface, the alternative methods yield the same result. In the following, the faster method of the 0.24 level will be taken to compare it to other values.

In the same Fig. 6.6, also the quantities from single profile fits are displayed. They are the average of 12×5000 extracted boundary-layer thickness

(a)　　　　　　　　　　　　　　　**(b)**
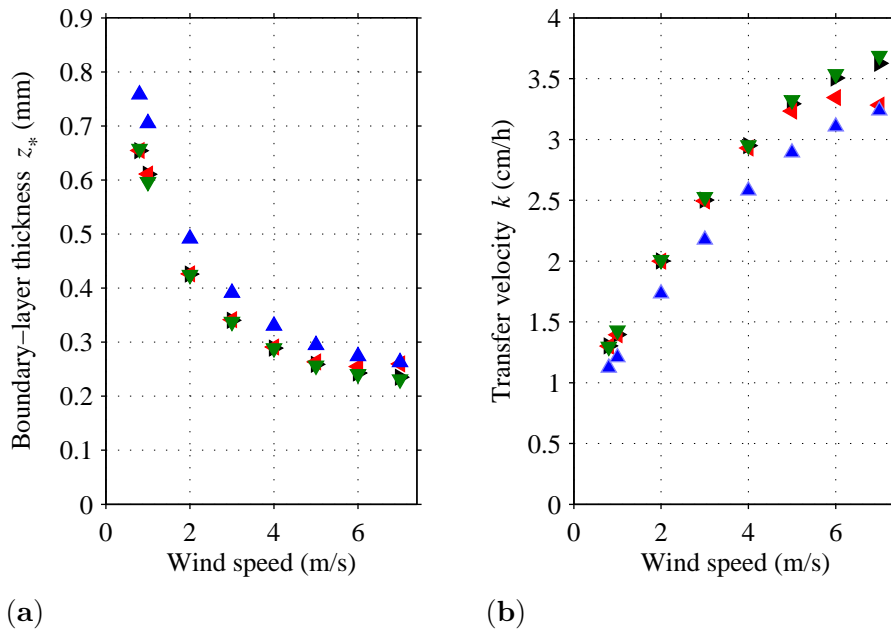
Figure 6.6: Correlation of boundary-layer thickness with wind speed. **(a)** Thicknesses derived with different methods are very similar: $\triangledown$: the distance at 0.24 level of concentration difference Δc. $\triangleright$: thickness of fitted boundary layer with model $p = 1$, $\triangleleft$: boundary layer as mean of a fit to single profiles; $\triangle$: result from fitting the model $m = 4$. **(b)** Calculated transfer velocities using $k = D/z_\star$

values. This is a good example of what was stated in Sec. 2.3: this value can differ under conditions of high turbulence but with low turbulence the difference is negligible.

For comparison the results from fitting the model $m = 4$ are also shown together with the other values. In the gas-transfer velocity k there is a significant difference between the models that were not distinguishable in the concentration profile fits of Fig. 6.4. To decide about the correct model, the transfer rate has to be determined with an independent method such as the mass-balance methods applied in the following Sec. 6.1.4 and Sec. 6.1.5.

An important question is: are the results reproducible? The same measurement as described above was conducted in another day. The results are compared in Fig. 6.7. The triangles are the results from the luminescence measurements in question.

In Fig. 6.7 for low wind speed, the agreement between the results from the boundary-layer thickness $z_\star$ in different measurement days is excellent. In the compared measurement the wind speed took longer to reach the desired velocity what increased the bulk concentration and lowered the signal-to-noise ratio. This is why the transfer velocity drops off earlier than in the
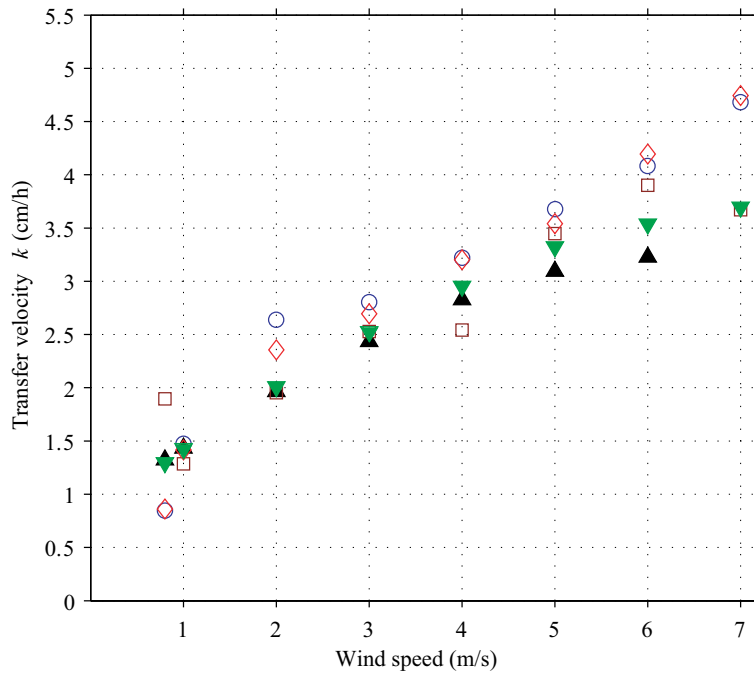
Figure 6.7: Transfer velocities from different measurements of luminescence compared to values from oxygen bulk concentrations for different measurement series. ▽: same as in Fig. 6.6; △: also luminescent measurement with same model on a different measurement; ◇: values from probe measurements parallel to ▽. □: parallel to △. ○: different (3rd) day but same conditions

other measurement of Fig. 6.6.b and could not be evaluated any more at the wind speed of 7 m/s.

6.1.4   Transfer Velocity from the Bulk Concentration

Another question is asking for the ground truth. To give an estimate for the quality of the achieved gas-exchange rates from the measurement of the boundary-layer thickness in depth profiles, the quantity of the transfer velocity was measured also with another method and different devices. Parallel measurements of dissolved oxygen concentration in the water and trace gases in the air were performed constantly permitting the calculation of reference transfer velocities k_{r}.

Using an oxygen sensor, the water side increase in O_2 concentration c_{w} was recorded during the experiment as shown in Fig. 6.8.a. It was assumed that a temporal concentration change in the water with volume V is only due to the gas exchange across the water surface A. This change of the oxygen concentration in the water is the same as the net transition of oxygen from

one phase into the other by gas exchange. As the mass is constant, a mass balance can be formulated:

$$V_{\mathrm{w}} \frac{\mathrm{d}c_{\mathrm{w}}}{\mathrm{d}t} = -k_{\mathrm{r}} A \left(c_{\mathrm{w}} - \alpha c_{\mathrm{air}} \right) \qquad (6.2)$$

The factor α is the dimensionless OSTWALD's solubility. From this equation the transfer velocity k_{r} can be calculated if we determine the temporal derivative of the water–side concentration directly from the measured data. The equilibrium water concentration $c_{\mathrm{bulk,eq}} = \alpha \, c_{\mathrm{air,eq}}$ can be determined from concentration convergence after six hours in Fig. 6.8.a because the air–side concentration did not change during the measurement.

(a)   (b)
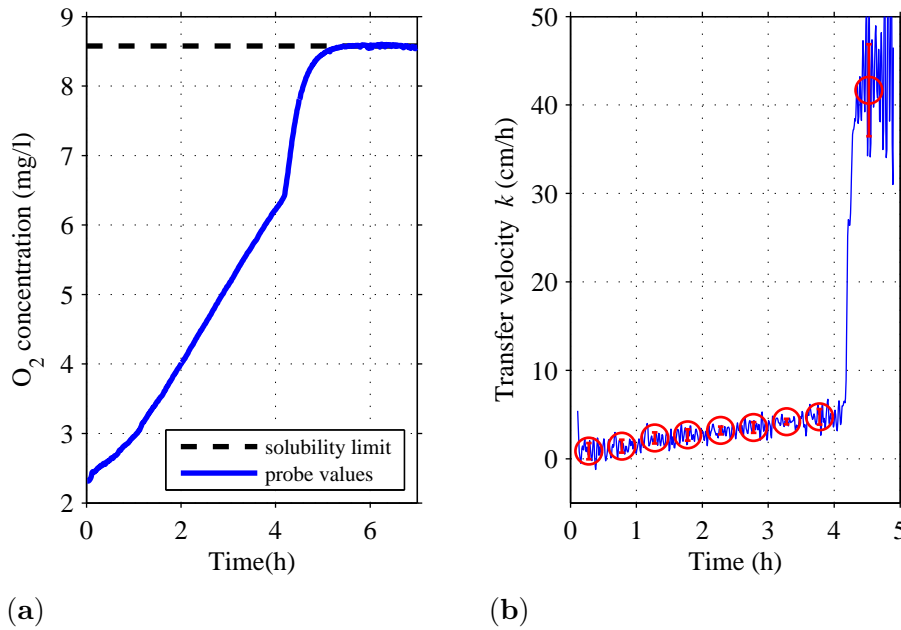
Figure 6.8: Evolution of the bulk O_2 concentration. **a**) Water bulk measurements of O_2 concentration. The O_2 concentration reached equilibrium after 4.5 hours. (**b**) Gas-transfer velocities computed from Eq. 6.2. Mean values for different wind speeds are indicated ($\bigcirc$) and compared to the results from phosphorescent measurements in Fig. 6.7

The resulting transfer velocity k_{r} is shown in Fig. 6.8.b. As the temporal resolution of this calculation method is in the order of minutes, the variance of the calculated values is high. Averaged values are represented by circles in the plot. The abrupt increase in the transfer velocity after four hours is caused by the formation of waves. At this time the stability of the surfactant film broke, as the critical wind speed was reached that lies between 7.5 and 8.0 m/s for the used circular wind–wave facility.

The gas-transfer velocities from the oxygen probe measurements are depicted in Fig. 6.7 together with the results from phosphorescence measure-

ments for comparison. The transfer rates for different measurements under the same condition show the same scale of magnitude and the same tendency. But the accuracy of this mass-balance method is not very impressing. The reason for the scattering is that the gas-sensor data is noisy, on some days much more than on others because of the unstable stirring of the oxygen probe. The accuracy of the measurement depends on the flux condition in the measurement cuvette as explained in Sec. 4.1.

6.1.5   Comparison with Transfer Velocities of Other Gases

Similar mass-balance methods of other trace gases had a higher accuracy. They were measured in the same experiment by Degreif [2006] and published in Falkenroth et al. [2007].
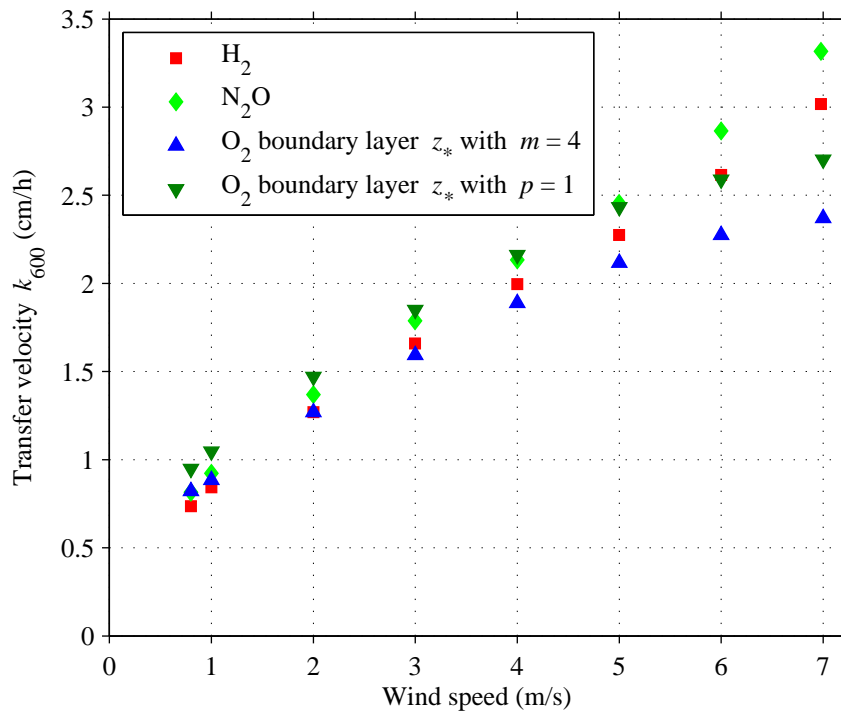
Figure 6.9: Simultaneous measurement of transfer velocities of different gasses scaled to $Sc = 600$. The comparison shows good agreement with the model $p = 1$ and less for $m = 4$ at higher wind speeds

To compare the gas-transfer velocities k they have to be scaled with the diffusivity D. More common is the scaling to a Schmidt number $Sc = 600$ what is the value of CO_2 in sweet water (cf. Eq. 2.6). Also the temperature dependence of the Schmidt number can be taken into account that was

retrieved from the thesis of Degreif [2006].

$$k_{600} = k \left(\frac{\text{Sc}(T)}{600} \right)^{-n} \tag{6.3}$$

The gas-exchange rates of the trace gases in Fig. 6.9 were calculated from air–side concentration measurements for the evading gases H_2 and N_2O. This figure shows that the transfer velocities derived from the boundary layer are in agreement with the reference measurements. This comparison demonstrates that the model of $p = 1$ is more likely to reflect the adequate description of the turbulence structure in the boundary layer than the model of $m = 4$. Especially at high wind speeds the latter is significantly lower than the reference gas-exchange velocities.

The transfer rates calculated from the boundary-layer thickness in Falken-roth et al. [2007] were significantly higher. The data was the same but the evaluation was done without concentration calibration and, what is more important, without surface detection because it was neglected without waves. This led to an additional smoothing of the data so that the wrong model of $p = 0$ was assumed what over estimates the gas flux.

6.2 Bulk Turbulences Generated with a Mixing Pump

Before an experiment the water in the channel was degassed and mixed using a water pump. This pump generates bulk turbulences that reached the water surface where the boundary layer with high oxygen concentrations is pealed off. This type of structures are interesting in some fields of research [Brumley and Jirka, 1987; Lee and Schladow, 2000; Atmane and George, 2001; Herlina and Jirka, 2004; Variano and Cowen, 2007]. The time series of one line with bulk turbulences are shown in Fig. 6.10.

The images demonstrates the penetration of the boundary layer by eddies. Most obvious are injection events: packages of water with high oxygen concentrations are transported in filaments away from the surface where they dilute in the well mixed bulk. These injection events are described also by Variano and Cowen [2007] who cites also other authors.

The performance of the registration step can be best seen going from Fig. 6.10.c to .d. Each profile is shifted so that the surface positions end up at a fixed pixel number of 50 in the registrated image.
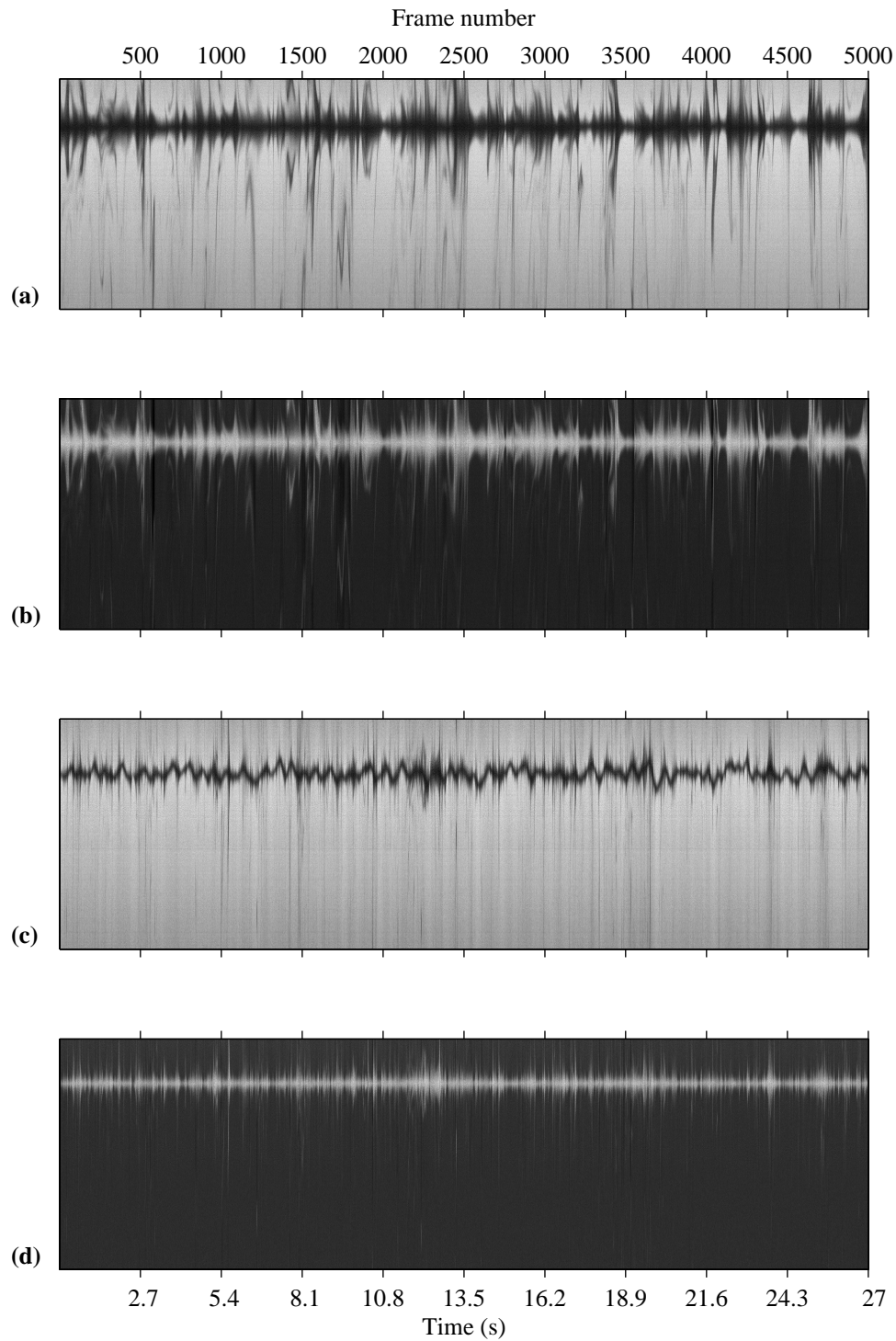
Figure 6.10: Time series of bulk turbulence generated by a water pump. The water depth shown is approximately 6.5 mm. (**a**) 11 L/min pump flow before image registration. (**b**) After image registration to the surface location. (**c**) 37 L/min before registration with visible waves. (**d**) After registration
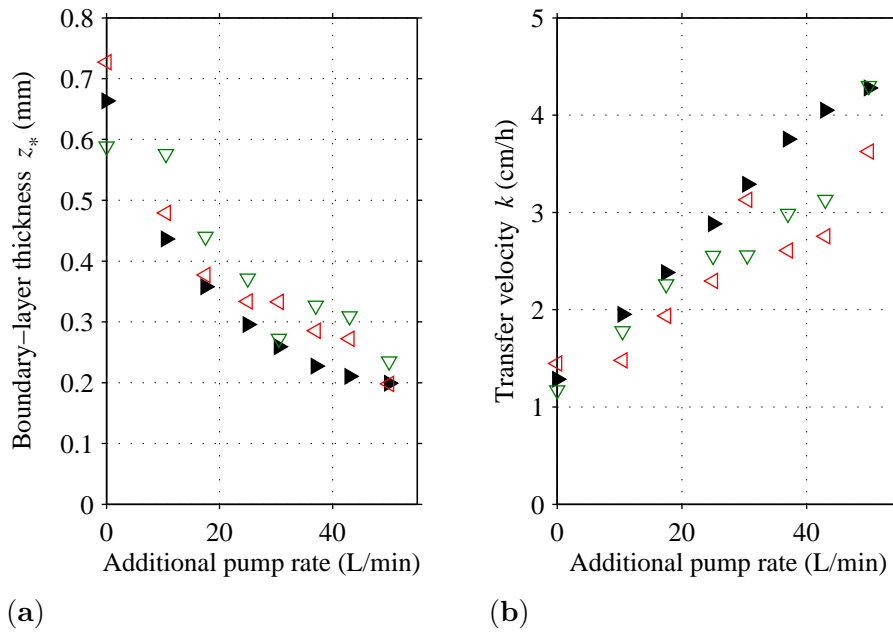
Figure 6.11: Correlation of boundary-layer thickness with additional pump flow to the constant flow of the gas exchanger. Every measurement point is an average of 12 mean profiles calculated of a time series like in Fig. 6.10. (**a**) The correlation of the boundary-layer thickness with pump flow. ▷ from model fit to mean concentrations. ▽ from model fit to single concentrations. ◁ from method with highest gradient of polynomial. (**b**) Corresponding transfer velocities

When analysing these time series, it is always important to keep in mind that a four dimensional flux in time is projected in the two dimensions of these images and that the medium is not stagnant but flows through the illuminated area giving the impression of a movement of a single water parcel.

Despite the high density of turbulence structures, the mean profiles could be evaluated with the same methods as shown before. The results are shown in Fig. 6.11.

The changing condition in this Fig. 6.11 is an additional flux of a mixing pump. It was varied in addition to the constant flux from the pump that was connected to the gas-exchanger module. The working gas-exchanger kept the concentration of oxygen in the bulk low what assured a constant and good contrast in the boundary-layer. As a result of this high signal-to-noise ratio also thin boundary-layer thicknesses smaller than $250\,\mu m$ could be resolved.

The comparison of different model fits reveals that a different theoretical description has the major influence on the turbulence structure as in the case of gas-exchange with a smooth surface. In Fig. 6.12 it is evident that the K-model with $m = 3$ is the closest to the measured data.
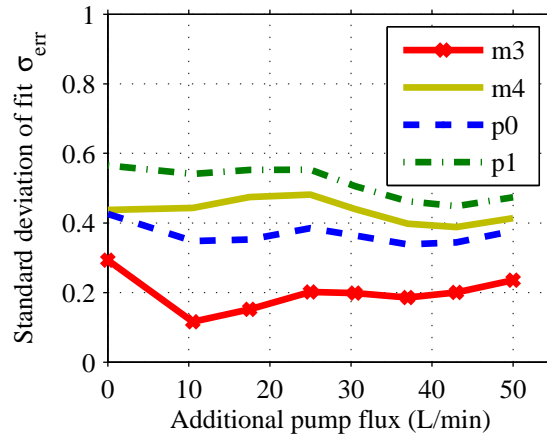
Figure 6.12: Error σ_{err} for different model fits varying the pump rate

Here the error σ_{err} does not increase significantly with thinner boundary layers even though they are thinner than in the case of the wind experiments with a surfactant. The reason for this is again the higher signal-to-noise ratio because of the low oxygen concentrations in the bulk.

The fit of the model $m = 3$ is the best also in the graph of normalised concentration c_+ in Fig. 6.13. The shape of the profile is different enough from the other theoretical descriptions to decide that this K-model is the most appropriate description of the concentration distribution in the aqueous boundary layer.

6.3   Turbulence Structures with Wind Waves

The difference of the model profiles for wavy conditions show a larger difference than the models for a smooth surface. Thus, the assignment to measured profiles seem to be more promising at wind waves. With the imaging method used in this work, no systematic measurements with wavy conditions were feasible. Only very low elevations of wind waves are still in the framed field of view of the camera with high magnification. Some examples of time series with a wavy surface and the analysis are discussed the following.

With a clean surface, even slow winds generate small waves, so-called capillary waves. In contrast to gravitational waves, the dominant force at this small scale is the surface tension. These waves are small enough to be imaged in the field of view of the camera with the high magnification used.

To keep the size of the wave small and exclude gravitational waves, a skimmer was positioned at the surface as a barrier. The skimmer had the width of the channel. It extended about 4 cm into the water what may have caused additional turbulences near the water surface. The position of the
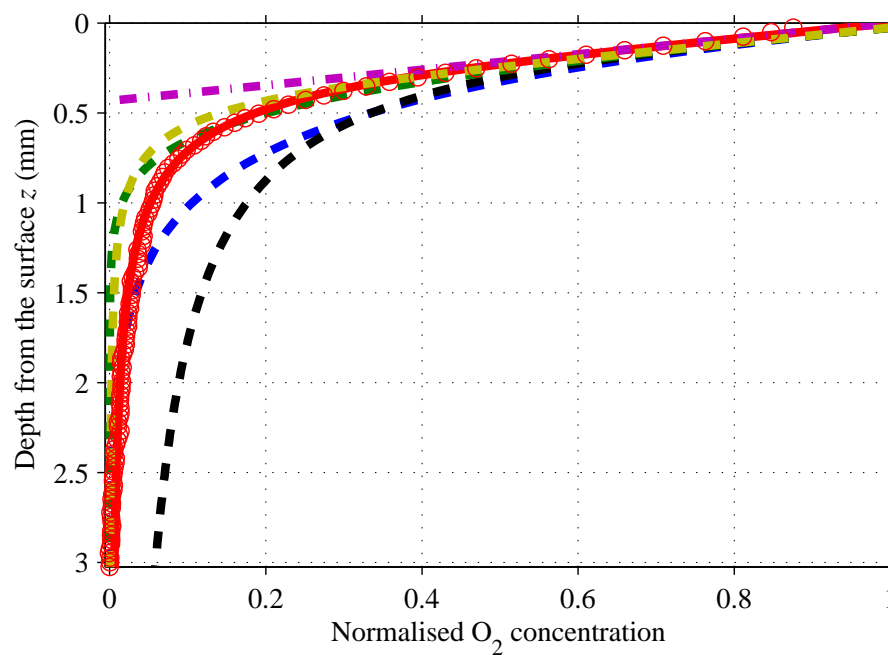
Figure 6.13: Fitting the theoretical models to the data of profiles with pump
turbulences (*circles*). For this condition the best model seems to
be the K-model $m = 3$ with the rigid-wall-assumption (*solid line*).
The other models of Sec. 2.2 are added in the plot for comparison
(*broken lines*: $m2$, $p0$, $p1$, $m4$). The additional pump flux was
11 L/min and the boundary-layer thickness was 435 μm

barrier was on the opposite side of the measurement position in the flume.
The skimming of the surface layer with wind stress assured also a clean water
surface.

Some example images with the wind speeds of 2.5 m/s and 2.6 m/s will
be discussed on the next pages because they show some interesting features.

In Fig. 6.15 a detail of the time series with a wind speed of 2.6 m/s is seen. In the image the line of the dark surface is still recognisable. Beneath it, a peeling event is visible. Here the boundary layer with high oxygen concentration is peeled off and transported away from the surface visible as dark structures.
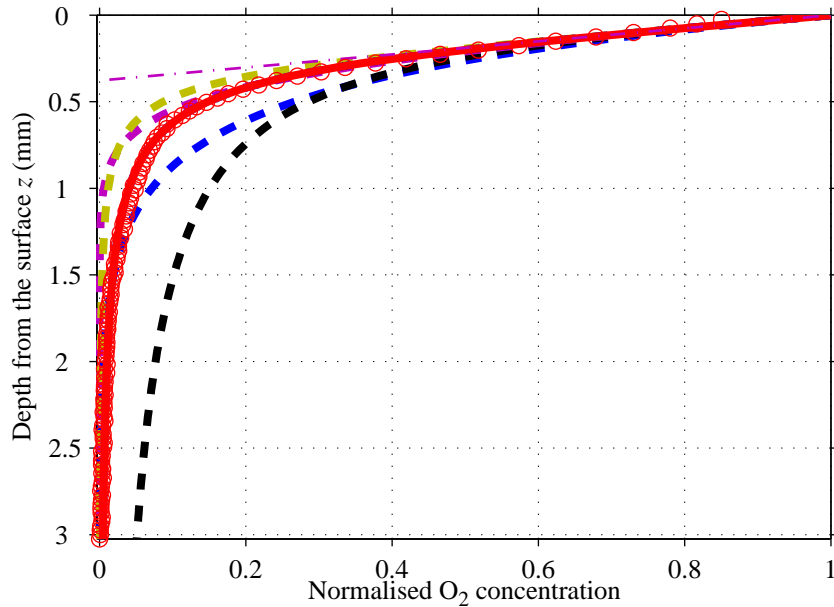
Figure 6.14: Wavy surface: mean concentration profile at 2.6 m/s. Here the best model is the K-model $m = 3$ showing a boundary-layer thickness larger than expected (from right to left: $m2$, $p0$, $m3$, $p1$, $m4$)

The mean concentration profile of 5000 single profiles is shown in Fig. 6.14. The boundary-layer thickness determined by the extrapolation of the surface gradient as seen in the figure is 380 µm. This corresponds to a transfer velocity k of 2.2 cm/h what shows not the expected enhancement compared to the value between 2.2–2.3 cm/h in Fig. 6.6 for a smooth surface.

The shape of the profile appears to correspond to the K-model. This is somewhat surprising because in Fig. 6.15 structures are visible that are more associated with surface-renewal events. The theory seems to be in some contradiction to the observed structures. But in this case it may be explained by a insufficient number or importance of the turbulent structures.

In Fig. 6.16 the performance of the image registration is demonstrated. In the upper image the raw intensity of the luminescence is seen. The lowest values are at the surface where the luminescence is quenched by oxygen molecules that penetrate the surface. In some distance a maximum of the intensity is reached. Then the intensity decreases by dye attenuation of the incident light. The undulating surface can be seen clearly.
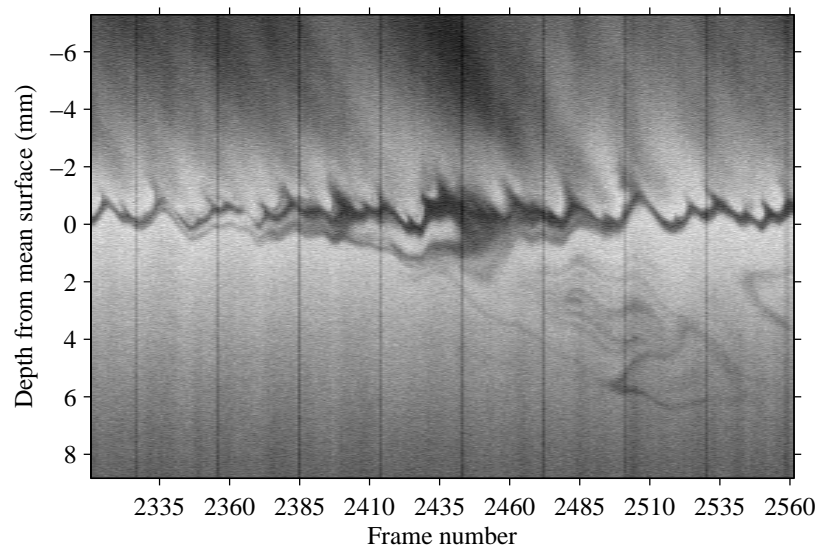
Figure 6.15: Wavy surface: raw time series at a wind speed of 2.6 m/s with visible surface-renewal events where high oxygen concentrations are pealed off the surface and lower the intensity in turbulent structures
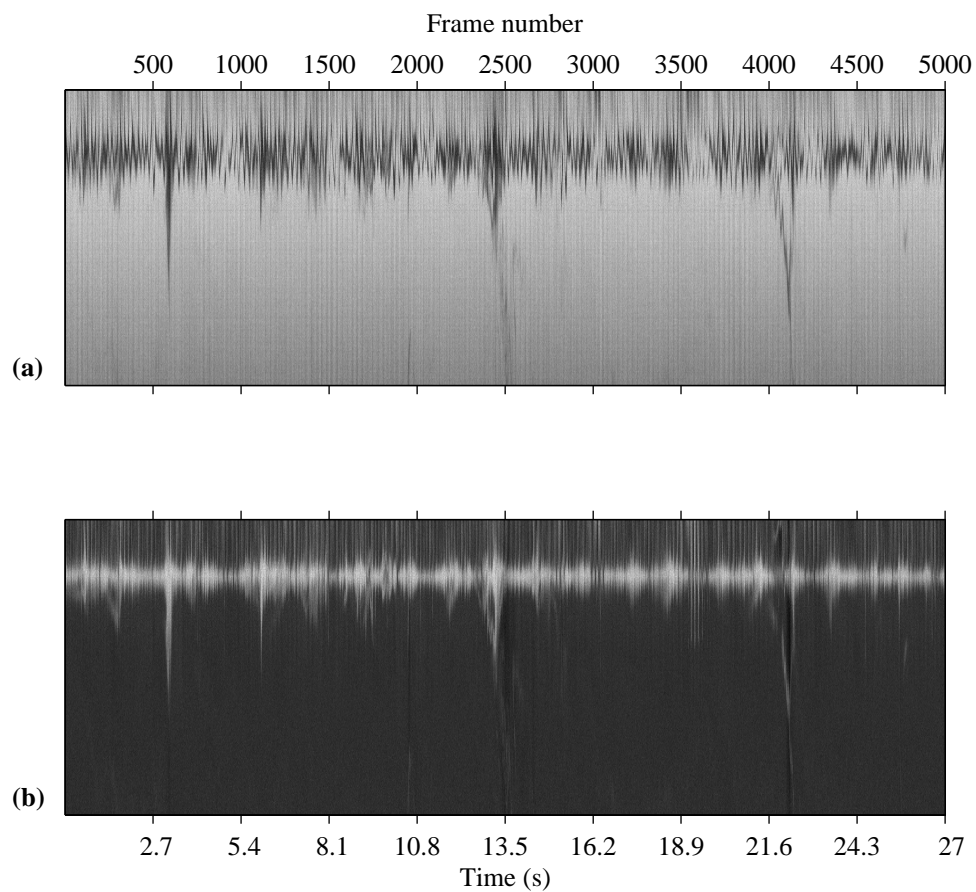
Figure 6.16: Wavy surface: image registration of time series at a wind speed of 2.6 m/s. (**a**) Before image registration. (**b**) After image registration

Image processing including image registration yields time series of the concentration profile shown in Fig. 6.16.b. No undulation can be seen any more. The bulk shows low oxygen as a dark colour with some injection events of high oxygen concentration. The high concentration near the surface is centred at a straight line indicating a successful image registration.

For the image registration this is the limit case because the feature of a reflecting surface is also not very pronounced with a wavy surface. But the details of the time series show clearly that on most rows no occlusions hinder the detection of the surface. Examples of unsuccessful image registration are documented in Appendix A.
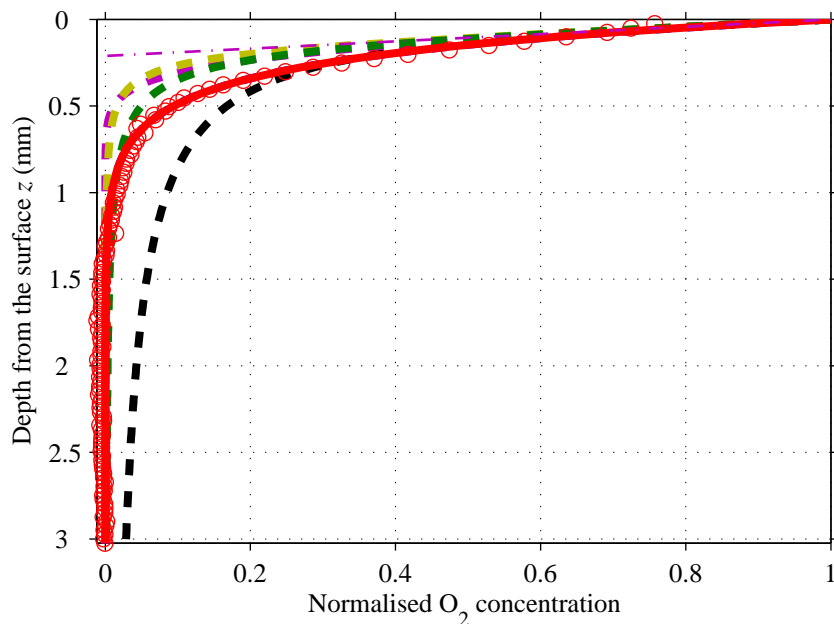
Figure 6.17: Wavy surface: mean concentration profile at 2.5 m/s. Here the best model is the surface-renewal $p = 0$ showing a small boundary-layer thickness ($m2$, $p0$, $m3$, $p1$, $m4$)

In Fig. 6.18, a detail of a time series with similar conditions but different observations is shown. The images were taken 40 min after the sequence shown before with the a slightly slower wind of 2.5 m/s. In the whole sequence, no turbulence structures of surface-renewal events are visible.

In contrast to this finding, the profile shown in Fig. 6.17 suggests the surface-renewal model $p = 0$. This model predicts a faster transport through the boundary layer and, consequently, the boundary-layer thickness here was 210 μm what yields a transfer velocity of 4.0 cm/h what is an enhancement of the gas flux that is expected in the presence of wind waves.
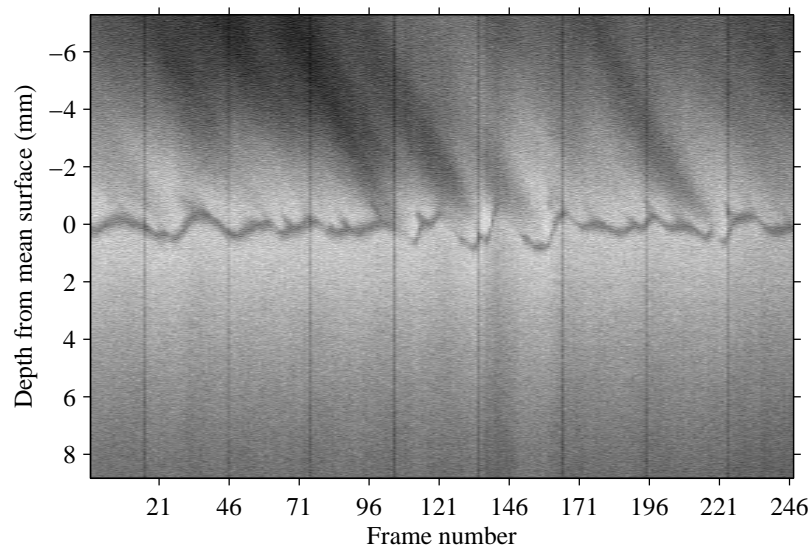
Figure 6.18: Time series with small waves without turbulence structures at
2.5 m/s wind speed. The grey values are raw luminescence intensi-
ties without any treatment
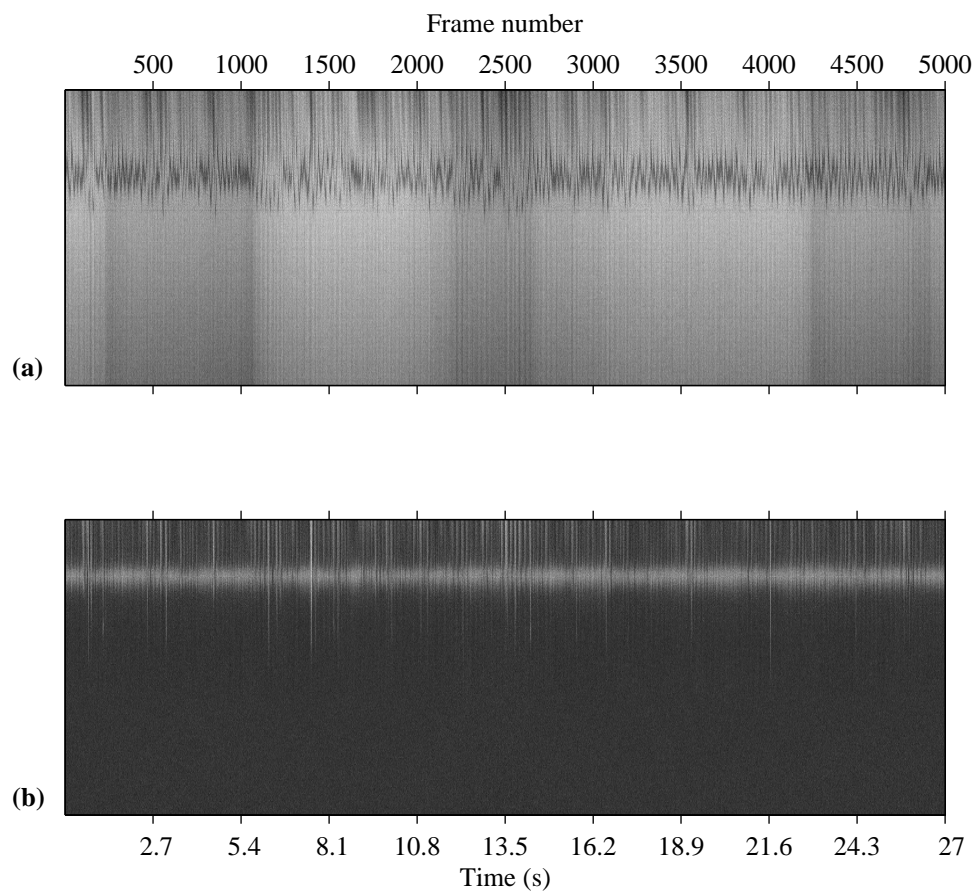
Figure 6.19: Wavy surface: image registration of time series at a wind speed of at
2.5 m/s. (**a**) Before image registration. (**b**) After image registration
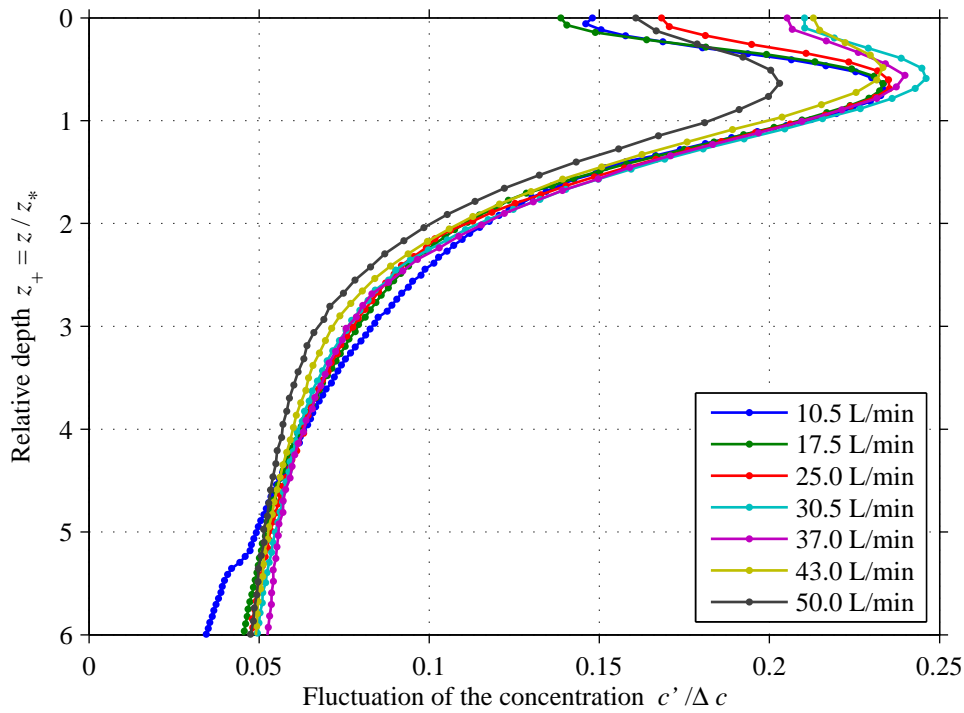
Figure 6.20: Fluctuation of the calculated concentration with bulk turbulence for different additional pump rates with the transfer velocities of Fig. 6.11.b

An unsuccessful image registration would result in a false profile but Fig. 6.19.b shows that it worked fine. The high concentrations are all in one straight line of a surface. In the raw data in Fig. 6.19.a some darker rows are visible. Here the camera showed instabilities that showed up in some sequences. The image processing handles this in the same way as intensity fluctuations caused by the incident light. After the calibration the fluctuations and the regions of low grey value do not appear in the time series of the concentration profile.

6.4   Fluctuation Profiles of the Concentration

In this part, the analysis of the fluctuation of the concentration will be documented. This fluctuation is a measure of the turbulence in the boundary layer. It was calculated as the standard deviation taking the root-mean-square of the difference between every single profile and the mean of 5000 profiles.

$$c' = \sqrt{\frac{1}{5000} \sum_i^{5000} (c_i - \bar{c})^2} \qquad (6.4)$$

Every fluctuation profile was normalised to the concentration difference Δc between the bulk and the surface. 12 profiles were averaged and plotted over the normalised depth z_+.

6.4.1   Fluctuations in Bulk Turbulences

In Fig. 6.20 the fluctuation with bulk turbulence is seen. The maxima of the fluctuations are all within the boundary-layer thickness $z_\star$. In the bulk, the concentrations should be homogeneously mixed and show less fluctuations. But the bulk turbulences show always many turbulence structures from injection events what explains high fluctuation values even far from the surface. VARIANO and COWEN [2007] describes also the transport of high oxygen concentrations in long filaments deep into the bulk.

The fluctuation do not tend to zero at the surface as the hydrodynamical model would suggest. Also the measurements with $60\,\mu m$ probe sensors by ATMANE and GEORGE [2001] shown in Fig. 6.21 show some fluctuations at the surface in the same order of magnitude. The concentrations of HERLINA [2005], plotted in the same graph, are calculated with the assumption of a constant concentration at the surface and so the fluctuations are defined to zero. In the classical surface-renewal model by DANCKWERTS [1951], the renewal events reach the surface and should generate some fluctuations.
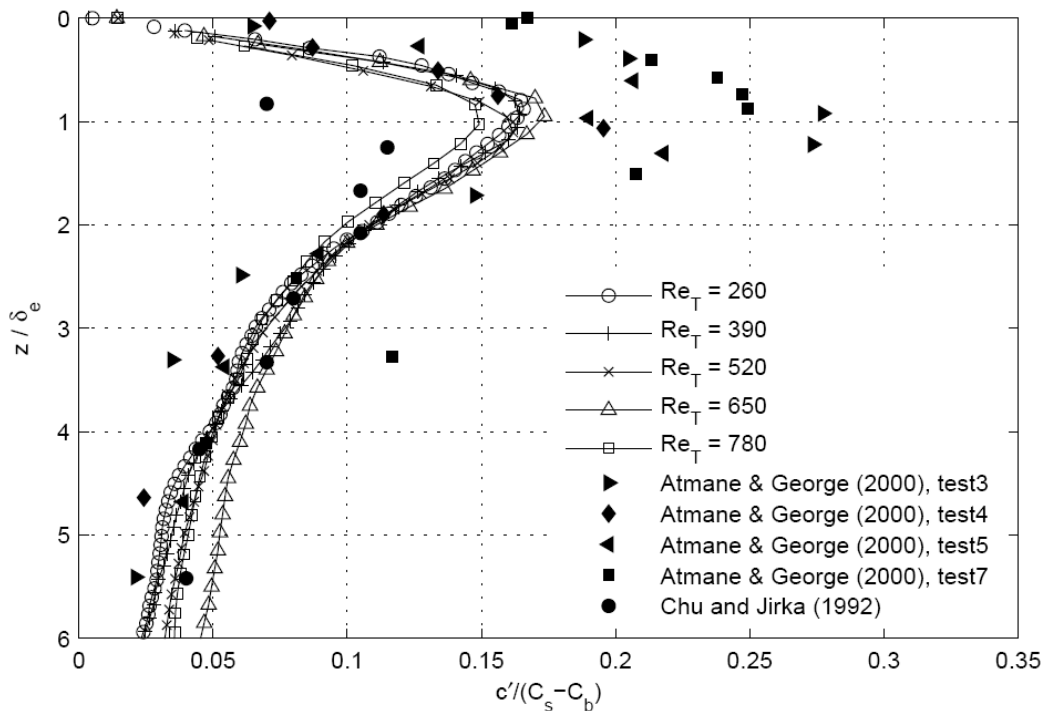
Figure 6.21: Comparison of concentration fluctuations in the literature (From HERLINA [2005])

In Fig. 6.21 both measurement techniques gave a maximum of the fluctuations around the distance of the boundary-layer thickness. But in both methods the determination of this distance has some uncertainty.

Pump flow	Δc	c_{bulk}	boundary-layer thickness
10.5 L/min	2.31	0.51	432 µm
17.5 L/min	2.29	0.59	354 µm
25.0 L/min	2.21	0.68	293 µm
30.5 L/min	2.10	0.74	256 µm
37.0 L/min	2.08	0.81	225 µm
43.0 L/min	1.95	0.88	208 µm
50.0 L/min	1.96	0.96	197 µm

Table 6.1: Parameters for the evaluation of fluctuations in the case of bulk turbulences assuming the model $m = 3$

6.4.2   Fluctuations in Wavy Conditions

As described in Sec. 6.3, the image registration worked only in some cases with small waves. Here two examples of time series are presented. The analysis of the concentration profile in Fig. 6.17 yields the surface renewal model $p = 0$ for the case at $2.5\,\text{m/s}$. The fluctuation in this case displayed in Fig. 6.22 in agreement with the model increases towards the phase boundary and is at a higher level than for the case at wind speed of $2.6\,\text{m/s}$. Here less fluctuations are seen and they decrease towards the interface. This is in agreement with the profile that was found to follow the K-model in Fig. 6.14.

Wind speed	model	Δc	c_{bulk}	boundary-layer thickness
2.6 m/s	$m = 3$	3.49	1.77	350 µm
2.5 m/s	$p = 0$	4.49	1.05	421 µm

Table 6.2: Parameters for the evaluation of fluctuations in the case of wavy conditions

The optical blurring hinders the fluctuation to fall too much. This smoothing effect prevents to observe the process directly at the phase boundary. But the effect is also caused by sensor noise that adds to the fluctuations. The noise level is higher at low luminescence intensity near the surface where oxygen quenches the phosphorescence. In the experiment with bulk turbulence, the bulk concentration was kept low by continuous degassing with
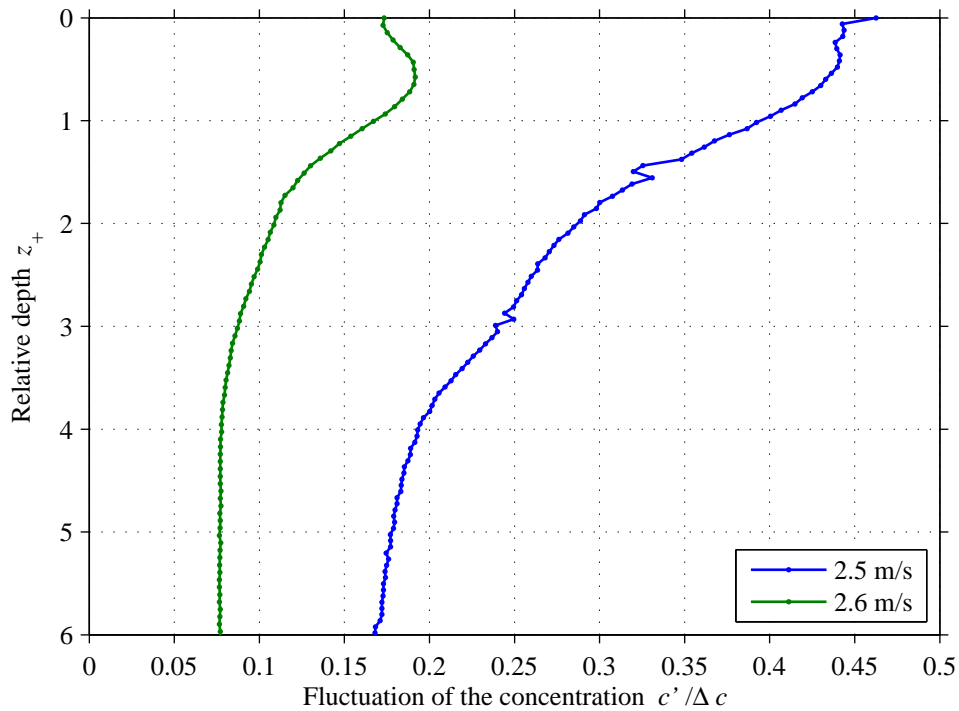
Figure 6.22: Concentration fluctuation at a wavy surface. The fluctuation increases towards the surface at wind speed 2.5 m/s in agreement with the found surface renewal for this case. The fluctuations decrease towards the interface at wind speed of 2.6 m/s to what the K-model was assigned

the gas-exchanger module. Here the effect of noise should be very low and should not change. In the experiment with a smooth surface and increasing wind speeds, the bulk concentration was increasing lowering the signal-to-noise level with time and increasing wind speed. The results in terms of concentration fluctuation is shown in Fig. 6.23 in the next section.

6.4.3   Fluctuations with Wind Stress at Smooth Surface

The fluctuations at a smooth interface in Fig. 6.23 increase towards the interface but the magnitude of the values is lower by a factor of 2 compared to the case of surface renewal in Fig. 6.22.

The low values and the trend of the fluctuation to higher values with lower signal-to-noise ratio indicates that in this experiment the fluctuation is mainly due to sensor noise. Also the discontinuity (at the step in Fig. 6.23 $z_+ = 1.2$ for 1 m/s) is a hint at sensor noise because of the different properties of the two parts of the sensor described in Sec. 5.1.

The small fluctuations in the bulk are in agreement with the observation of only very few renewal events. The increase of these fluctuations is again caused by the low signal-to-noise ratio at high oxygen concentrations in the bulk.
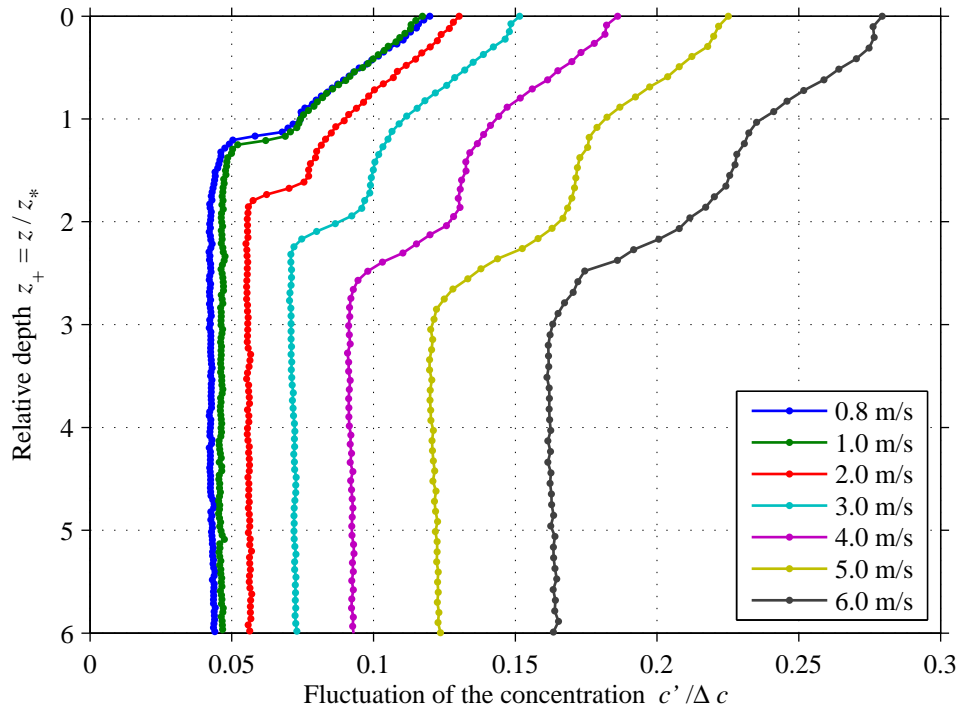
Figure 6.23: Fluctuation at a smooth surface with different wind speeds

Wind speed	Δc	c_{bulk}	boundary-layer thickness
0.8 m/s	2.53	2.55	648 µm
1.0 m/s	2.43	2.86	604 µm
2.0 m/s	2.24	3.32	421 µm
3.0 m/s	1.99	3.86	337 µm
4.0 m/s	1.75	4.43	284 µm
5.0 m/s	1.49	5.01	256 µm
6.0 m/s	1.24	5.59	243 µm

Table 6.3: Parameters for the evaluation of fluctuations in the case of smooth surface assuming the model $p = 1$

Chapter 7

Conclusions: Discussion of the Findings

This chapter evaluates the different aspects of the results of this thesis. This is also an opportunity to compare the findings with the results that other authors presented in related fields of research.

Phosphorescent Dye. The characterisation of a novel phosphorescent metal–ligand complex (MLC) showed excellent agreement with the requirements for the application as an oxygen indicator in water. The STOKES shift between absorption and emission was wide enough to exclude significant self-absorption (Sec. 3.6) that would falsify concentration computations. The synthesis of the organo–metal compound can be accomplished without intermediates from commercially available educts (Sec. 3.4). The new phosphorescent dye for the quantitative visualisation of concentration fields within the aqueous mass-boundary layer shows significant advantages over the previously used dyes. These include high quantum yield, prompt solubility, strong absorbance, high photo-stability, large STOKES shift and no surface activity. Thus, a much better signal-to-noise ratio and reliability can be expected from this oxygen indicator compared to previous studies [MÜNSTERER, 1996; HERLINA, 2005] (Sec. 3.7).

Set-up. The experimental set-up allowed the generation of reproducible conditions for the study of gas-exchange processes (Sec. 4.1). Because of the temperature dependence of the dye the experiments were conducted with a stable water temperature. The introduction of a new experimental method for changing gas concentrations in water with a novel gas-exchanger module helped to reduce the preparation time compared to a technique relying on nitrogen bubbling found in the literature [HERLINA, 2005]. Moreover, the accuracy and hence reproducibility is also significantly higher with these

gas-exchange modules. The lower bulk concentrations increased the contrast at the boundary layer with an additional positive effect on the signal-to-noise ratio (Sec. 4.4).

Transfer velocity. Direct measurement of oxygen-concentration profiles turned out to be an accurate method for gas-exchange studies. The different approaches for determining the transfer velocities in wind experiments with a smooth surface are in good agreement proving the applicability of the used techniques. There is no fundamental difference in the results for the evasion of the trace gases N_2O and H_2 that were carried out by Degreif [2006] from the invasion of oxygen measured with a mass-balance method and using the boundary-layer thickness to calculate the gas-exchange rate for the same measurement day (Sec. 6.1.5). The measurement of reference bulk concentration need simple improvements detailed in Sec. 8.2 to stabilise the measured values in order to achieve the accuracy of the other methods (Sec. 6.1.4).

Model prediction at smooth surface. The concentration profiles revealed the depth dependence of the turbulence. Analysing the profiles by fitting the theoretical predictions to them (Sec. 6.1.2) in combination with the comparison of the transfer velocity (Sec. 6.1.5), showed that the gas-exchange with a smooth water surface are best described by the surface-renewal model $p = 1$. In this model, the transport is dominated by events. Remarkable is the observation that no expected turbulence sturctures were seen in the sequences. The remaining uncertainty in this statement is due to the limited optical resolution that hinders to determine directly the concentration and its gradient at the surface. The fitting approach helped to deal with these limitations (Sec. 5.6).

Comparison with previous studies. In comparison, Münsterer [1996] observed a behaviour between the models of $p = 1$ (surface-renewal model) and $m = 3$ (K-model). Possibly also $m = 4$ (cf. Eq. 2.22), that was calculated only in the present work, would be an adequate model for the description of his profile shapes but this could not be verified because the data was not available. His wind speeds over a smooth surface were up to $4\,\mathrm{m/s}$ but are difficult to compare because the dimension of the wind–wave tank and the position of the wind sensor relative to the surface was different. By calculating the friction velocity $u_\star$, a comparison could be done but the available measurements in the same wind–wave facility of Degreif [2006] for a wavy surface and Garbe et al. [2007] for a smooth surface show high uncertainties. For wavy conditions Münsterer [1996] has visualised concentration profiles

suggesting the surface-renewal model $p = 0$ at wind speeds faster than $5\,\text{m/s}$. However, the resolution gave only 3–4 measurement points within the boundary layer making the normalisation to the concentration difference difficult.

Alternative evaluation of profiles.   The evaluation using simple extrapolation of the highest gradient (Sec. 5.7) yielded similar results for the transfer velocity as the fitting procedure (Sec. 6.1.3). When the boundary-layer thickness is comparable to the blurring, the prediction of the adequate profile was only possible by modelling the function with the theoretical profile after convolution with the blurring function (Sec. 6.1.2). This method had also advantages when, instead of the mean, the single profiles with a high noise level were analysed because no smoothing of the data was necessary. In the presence of shear, induced by wind speeds up to $7\,\text{m/s}$ over a smooth surface, only few turbulent structures could be observed. This is reflected by the fact that no bimodal evaluation was needed for correct transfer rates as suggested by JÄHNE et al. [2007] recently and in this case the statistical effect described in Eq. 2.34 can be neglected. Thus, the values of the gas-transfer velocity from both, mean and single profile evaluations (Sec. 6.1.3) show no significant difference.

Bulk turbulence.   A side product, that seemed to be worthy to analyse, was the turbulence generated by a mixing pump. Hence, the concentration profiles behave like the K-model with $m = 3$ described in Eq. 2.21. The decision was more definite than in the case described above The evidence was the residual difference between the fit and the smoothed model function (Sec. 6.2). That this profile shape is different from the form of the profile with wind stress is expected because no shearing forces at the interface are present. Even though the water was circulated by the pump flow and some shear stress was generated. This may partly explain the difference to experiments by HERLINA [2005] in a shear free grid steered tank where mean flows were avoided. She described the profiles always with exponential functions from the surface-renewal model of Eq. 2.29. Another reason may be that her surface was cleaned while in the pump experiments herein described a surfactant film was always present and difficult to remove, once it was applied.

Concentration fluctuations near the surface   To analyse concentration fluctuations in the boundary layer a very high signal-to-noise ratio is required to exclude effects of the sensor noise. This prerequisite was fulfilled in the case of bulk turbulences. Here a comparison of the fluctuation profiles with other studies showed parallels of the measurements in the water flume to

bottom-generated tanks where other authors avoid every mean flow or shear stress.

Chapter 8

Summary and Outlook

Before an outlook on future studies is given, the work and the central results will be summarised in this chapter.

8.1 Summary

Gas transfer across gas–liquid interfaces is of importance in natural environments and technical applications. Recently, the exchange of gases between the two most important reservoirs in the global cycling, the atmosphere and the oceans, has received increased attention considering that it determines the global distribution of many gaseous and volatile chemical species. Large uncertainties in climate modelling are mainly due to the fact that mechanisms controlling air–water gas transfer in conditions such as the presence of surfactants or the different domains of wind speeds are not well understood. Current parametrisations are semi-empirical exhibiting scatter in gas-transfer velocities in the order of 200%.

The transfer of sparingly soluble gases including carbon dioxide, methane and oxygen is controlled by the transport from the air–water interface through the sub-millimetre aqueous boundary layer. With novel visualisation techniques applying the idea of laser-induce fluorescence (LIF), the mechanism of the exchange processes can be visualised. This enables the analysis of concentration profiles a few hundreds of microns beneath the surface.

LIF studies on gas exchange previously presented in the literature verified mostly qualitative effects of the turbulence and measured concentration fluctuations in the boundary layer. In combination with particle-image velocimetry the turbulence state of the liquids was determined in image pairs. The signal-to-noise ratio of established LIF techniques is partly limited by the poor quantum yield of the used luminescent dyes restricting the resolution in space and time.

In this study, a novel phosphorescent ruthenium–ligand complex was applied as a luminescent dye taking advantage of its favourable properties. The dye demonstrates an increased luminescence intensity and sensitivity to the oxygen concentration in water. This allowed improved experiments in a circular wind–wave channel increasing significantly the frame rate of the digital camera. This is a vital prerequisite for exchange processes which take place on time scales of fractions of a second. Concentration profiles could be visualised with a high spatial resolution achieving 25.2 µm/pixel. The enhanced intensity contrast made short exposure times possible enabling a camera frame rate of 185 m/s that is fast enough to observe some turbulence processes in gas-exchange experiments. Experiments were run by varying oxygen concentrations in the water body and by measuring the response due to the exchange processes. These experiments were facilitated by novel commercial gas-exchange modules significantly reducing experimental effort.

A challenge in the evaluation of image series from luminescence profiles is the detection of the surface. The developed image-processing algorithm performed well in the case of a smooth surface. It was possible to extract the boundary-layer thickness accurately. In the experiment with winds of 0.8–7 m/s and a surfactant film on the surface, the thickness decreased from 670 µm to 250 µm which is only little more than the effective resolution of approximate 200 µm. From the values of the boundary-layer thickness, gas-transfer velocities for a smooth surface were calculated between 1.3–3.6 cm/h. They correlated well with reference evasion measurements of N_2O and H_2 conducted in parallel. This gave a ground truth for the measured quantities. Additionally the transfer rates were calculated from bulk oxygen measurements with a similar mass-balance method as for the mentioned trace gases. The obtained values for the transfer rates from the mass-balance technique are similar to the results from the other methods but showed some fluctuations.

The analysed quantitative concentration distribution in the boundary layer is a result of molecular diffusion and turbulent transport. The mathematical description of the concentration profile revealed differences for different conceptual descriptions. A new mathematical formulation was added to the four functions that were developed previously by other authors. These were needed to analyse the shape of the measured concentration profiles.

The systematic analysis of the concentration profile at smooth surfaces together with the comparison of the transfer velocity made it possible to distinguish between the different theoretical approaches. The measured data suggests that the description using the theory of surface-renewal events is the best representation of the concentration profile observed. But the differences between the models are not significant enough. However, the expected tur-

bulence structures, that the surface-renewal model predicts, were not visible with a flat surface even at high shear stress with wind speeds of 7 m/s.

The novel visualisation technique improved significantly the resolution of concentration imaging in the aqueous boundary layer. In fact, for the first time systematic measurements were accurate enough to determine the boundary-layer thickness from concentration profiles and calculate transfer velocities with the same accuracy as measured with mass-balance methods. With the presented procedure, new opportunities are opened to study the mechanisms of gas exchange on a small scale of the diffusive boundary layer where fundamental theoretical knowledge is lacking.

8.2 Outlook: Possible Improvements and New Concepts

The presented method with the novel indicator dye is easy to apply in other studies providing a high signal quality for oxygen measurements in water. A possible combination with particle-imaging velocimetry PIV enables to visualise additionally flow fields in the water. The techniques complement one another as shown by HERLINA and JIRKA [2004] and VARIANO and COWEN [2007].

Currently a new inert and chemically clean linear wind–wave facility is being constructed that is specifically designed for the visualisation technique described in this study. The air space and the water channel will be coated with Teflon and the whole facility is gas-tight. Therefore, acid and alkaline gases can be used in this facility. The water channel will be 4 m long, about 0.4 m wide and 0.1 m high and can be filled with ultraclean water. This facility will provide an improved optical access allowing the imaging with a higher optical resolution.

The measurement of the fluorescent lifetime, that is shortened by the presence of quenching oxygen, gives concentrations independently from the intensity of the phosphorescence. A new type of 'smart-pixel' sensors may approach this aim. Such a camera is able to detect modulations of light in the frequency range of several MHz. PMDTechnologies in Siegen, Germany, distributes camera system that use this principle to measure distances adding to every pixel of a 2D image a depth information. When the absolute intensity is not the measured quantity any more than the method is not suggestible to intensity fluctuations of the exciting light or to inhomogeneous concentration of the dye. It is imaginable to visualise the boundary layer in the field by dropping small amounts of dye in a focused area on a lake or the ocean.

To keep a constant signal-to-noise ratio, the bulk concentrations should

be kept as low as possible. This can be achieved by starting the experiments quickly after the degassing procedure. But this excludes the possibility of measuring other tracers in the same experiment that need time to be solved in the water body for evasion experiments. One solution is to develop the mass-balance method further. A new technology of oxygen probes uses a similar phosphorescent technique as in the presented work. It is now commercially available and promises to reduce the noisy signal of the oxygen sensor without the need of constant stirring.

Alternatively separate experiments can be restarted for every wind speed. Shorter measurement times increase the bulk concentration and the contrast of luminescence at the surface boundary layer. The ideal solution to the increasing bulk concentration would be to keep the concentration low by continuous degassing. But here the problem arises of how to avoid the turbulences generated from the flow through the gas exchanger. And then the transfer velocity can not be computed from the simultaneous change of bulk concentrations or of concentrations of other reference gases.

High frame rates are needed for resolving turbulent processes and resolve the movement of the surface subject to undulations by waves. But high frame rates limit also the signal-to-noise ratio. The photo-stability of the novel phosphorescent dye is good enough for the employment of a brighter light source that would increase the signal-to-noise ratio for more accurate measurements of fluctuations.

Part IV

Appendix

Appendix A

Wavy Conditions with Unsuccessful Image Registration

In Fig. A.2 a typical time series taken with winds of $2.8\,\mathrm{m/s}$ is found. The wave slope is higher than in the images shown in Sec. 6.3 what leads to effects that make it impossible to compute concentration profiles. A light saturation is seen because of focussing effect of a curved wave. The surface is rarely recognisable because passing waves cause occlusion effects. The frequent turbulence structures are difficult to distinguish from the feature of the surface. The waves on the surface also suppress the total reflection.

Although the image registration in Fig. A.3 failed, the profile was analysed with the same tools as the mean profiles before. The false mean profile in Fig. A.1 appears to follow the surface-renewal model. This means that even without a correct image registration, the concentration profiles seem to make sense what is misleading. Hence, every evaluation has to be done with care paying attention to the successful image registration of the surface. A similar case is documented in the following.
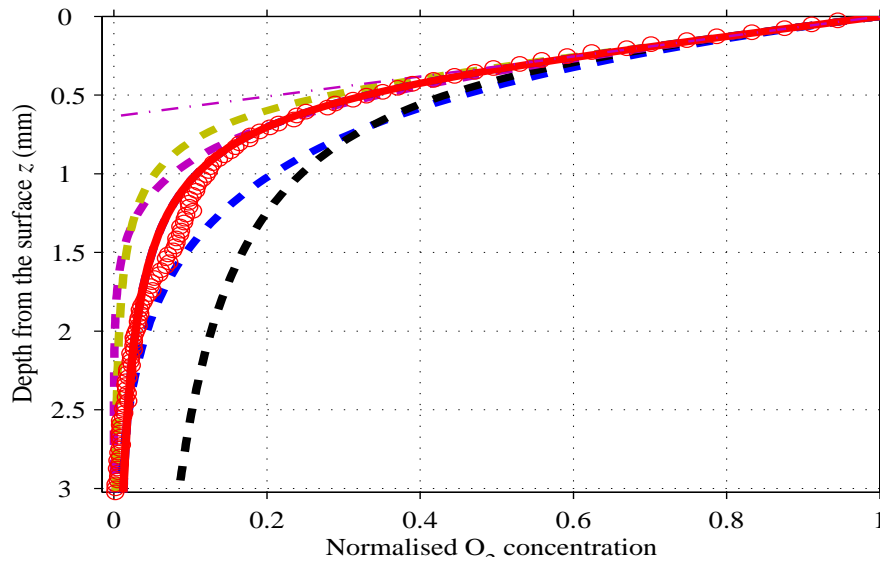
Figure A.1: Wavy surface: false mean concentration profile at $2.7\,\mathrm{m/s}$. After unsuccessful image registration the profile looks like the K-model $m = 3$. The boundary-layer thickness is overestimated ($m2$, $p0$, $m3$, $p1$, $m4$)
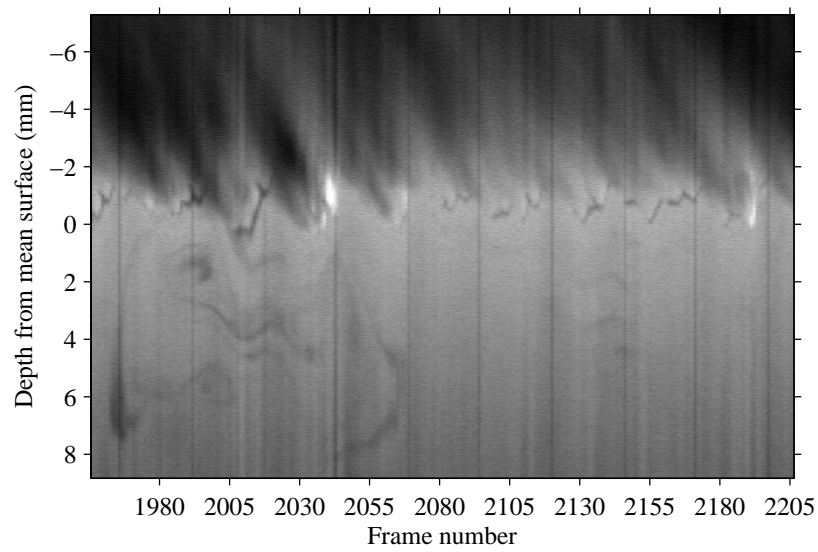
Figure A.2: Time series with small waves with high turbulence structures at 2.7 m/s wind speed. Surface-renewal events are visible. The surface is not always seen hindering a successful registration
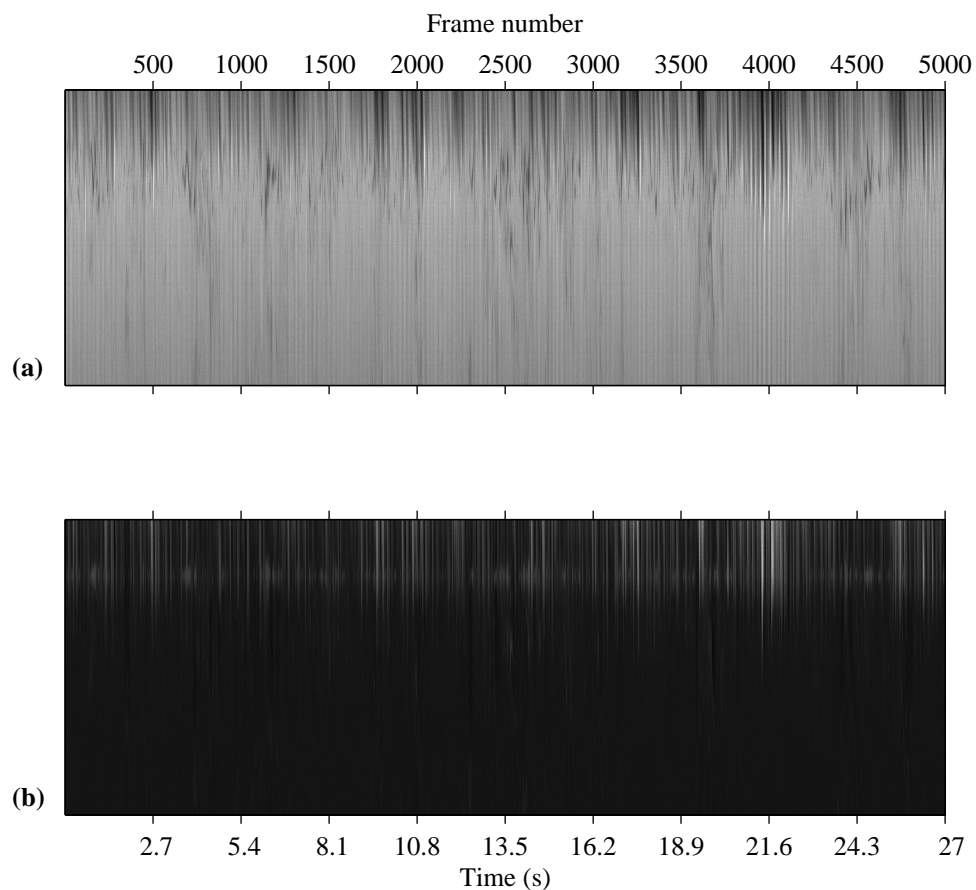
Figure A.3: Wavy surface: image registration of time series at a wind speed of 2.7 m/s. (**a**) Before registration. (**b**) After unsuccessful registration

The case shown before and also the case shown in Fig. A.5 and Fig. A.6 with wind speed of $2.8\,\mathrm{m/s}$ represents a examples beyond the possibilities of the used image processing techniques. But they demonstrate some pitfalls in the analysis of the mean profile shape.
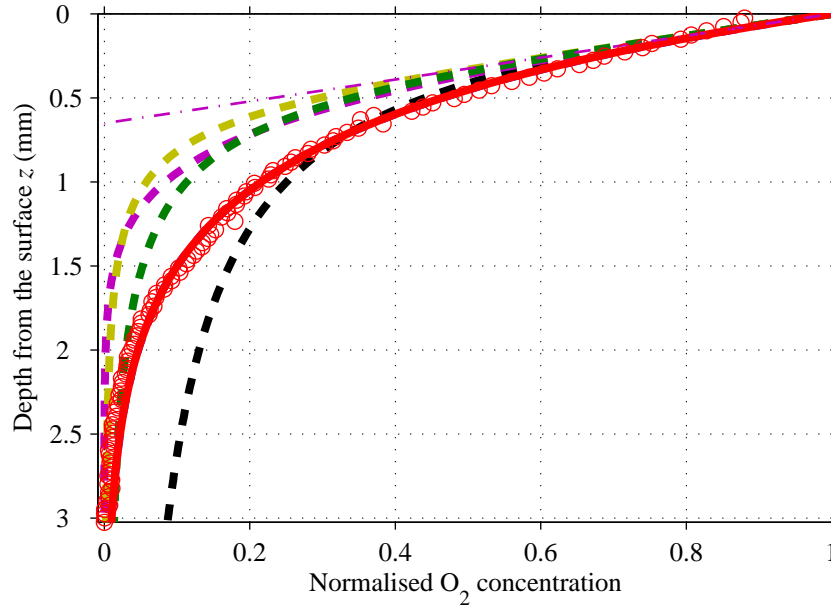
Figure A.4: Wavy surface: false mean concentration profile at $2.8\,\mathrm{m/s}$. After unsuccessful image registration the best model seem to be the surface-renewal $p = 0$. The boundary-layer thickness is overestimated ($m2$, $p0$, $m3$, $p1$, $m4$)

An interesting point in Fig. A.4 is that the profile shape changes again. With similar conditions as before, here the profile of the classical surface-renewal model $p = 0$ seems to be the best. Thus, profiles without a successful image registration do not always lead to a $m = 3$ profile as in Fig. A.1 but may also look like a $p = 0$ profile as in Fig. A.4.

In the detail of the time series in Fig. A.5, a low contrast is seen because of a high oxygen concentration. Similar problems in the detection of the surface are found as in Fig. A.2 and only very few surface-renewal events.
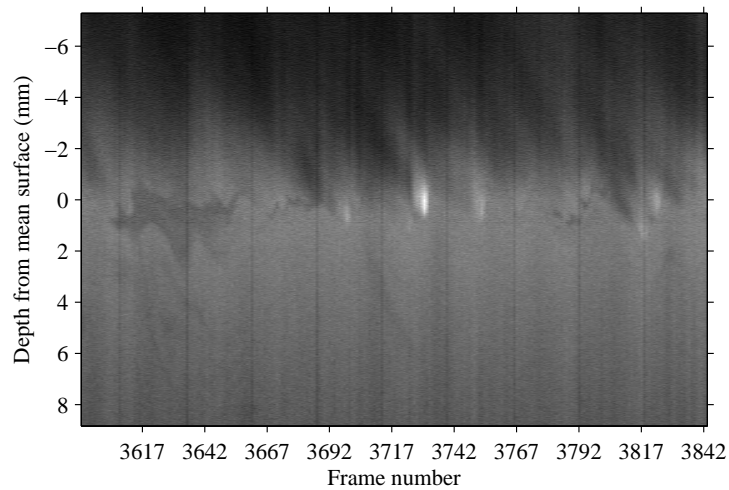
Figure A.5: Time series with small waves with few turbulence structures at 2.8 m/s wind speed. The contrast is low because of high oxygen concentrations in the water bulk
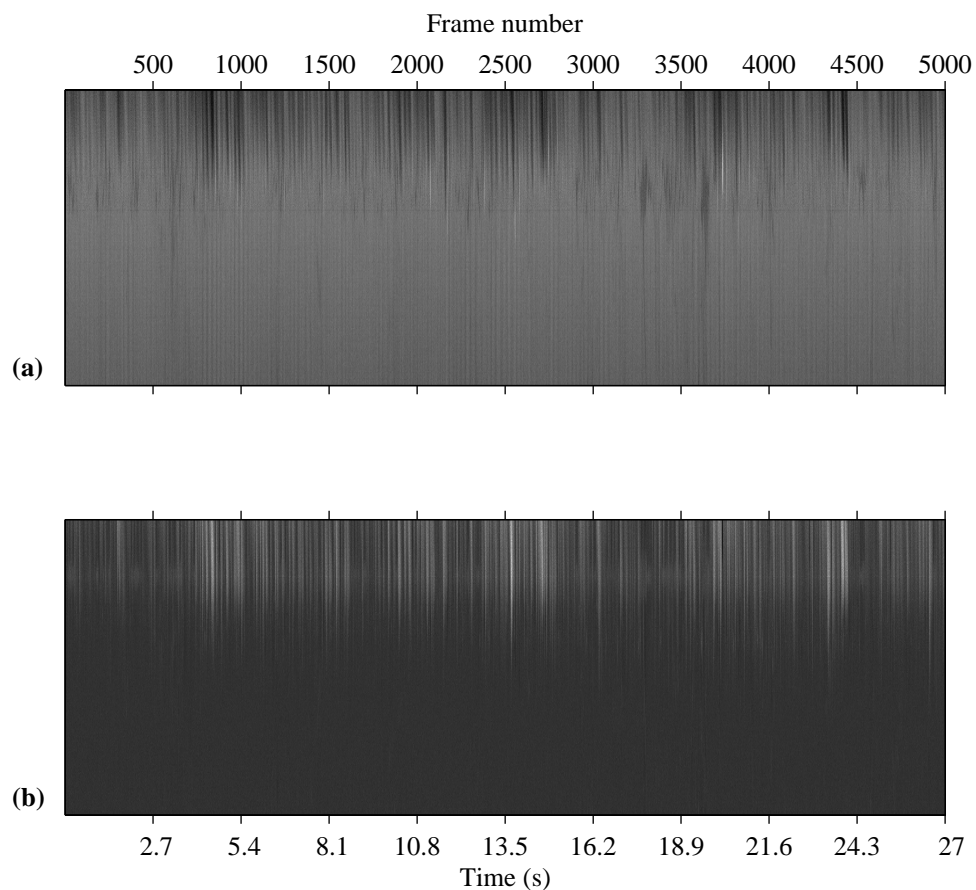
Figure A.6: Wavy surface: image registration of time series at a wind speed of 2.8 m/s. (**a**) Before image registration. (**b**) After unsuccessful image registration

Appendix B

Mathematica Script for Boundary-Layer Mathematics

The algebra programme Mathematica®5.0 (2003) was employed for solving of the differential equation Eq. 2.11. The starting point was the power law proposed by JÄHNE et al. [1989]. Some of the results are similar as in MÜNSTERER [1996].

In the study herein, the model for $m = 4$ was needed to describe the concentration profiles at a smooth surface. This model was applied in Sec. 6.1.2 for the analysis of the turbulence structure.

In the following, the complete script will be documented to give the possibility to reconstruct the deductions in Sec. 2.2.2. Maybe it is a good starting point to refine the theory on turbulence in the boundary layer.

Concentration Profiles in Boundary Layer

Small Eddy K_t Model from Eq. 2.10

```
In[1]:= Clear[c, α, c2]
```

```
In[2]:= eq10 = D[((1 + α z^m) * D[c[z], z]), z]
```

$Out[2]= \ m \, z^{-1+m} \, \alpha \, c'[z] + (1 + z^m \, \alpha) \, c''[z]$

- **Solve stationary case of Eq. 2.10**
  $m \to 2; \ \alpha \to + \frac{\pi^2}{4}; \ 1 - \frac{2}{\pi} \, ArcTan[\frac{\pi}{2} \, z] = \frac{2}{\pi} \, ArcCot[\pi \, z \ / \ 2];$

```
In[3]:= generalSol[z_] =
           c[z] /. DSolve[{eq10 == 0, c[0] == 1, D[c[z], z] == -1 /. z → 0}, c[z], z] // Simplify
```

$Out[3]= \ \left\{ 1 - z \, (1 + 0^m \, \alpha) \, \text{Hypergeometric2F1}\left[\frac{1}{m}, 1, 1 + \frac{1}{m}, -z^m \, \alpha\right] \right\}$

```
In[4]:= generalSol[z_] = Simplify[generalSol[z], m > 0]
```

$Out[4]= \ \left\{ 1 - z \, \text{Hypergeometric2F1}\left[\frac{1}{m}, 1, 1 + \frac{1}{m}, -z^m \, \alpha\right] \right\}$

```
In[5]:= FunctionExpand[generalSol[z]]
```

$Out[5]= \ \left\{ 1 - \frac{z \, (-z^m \, \alpha)^{-1/m} \, \text{Beta}\left[-z^m \, \alpha, \frac{1}{m}, 0\right]}{m} \right\}$

```
In[6]:= generalSol[z] /. m → {2, 3, 4}
```

$Out[6]= \ \left\{ \left\{ 1 - \frac{\text{ArcTan}\left[z \, \sqrt{\alpha}\right]}{\sqrt{\alpha}} \, , \ 1 - z \, \text{Hypergeometric2F1}\left[\frac{1}{3}, 1, \frac{4}{3}, -z^3 \, \alpha\right] \right., \right.$
$\left. \left. 1 - z \, \text{Hypergeometric2F1}\left[\frac{1}{4}, 1, \frac{5}{4}, -z^4 \, \alpha\right] \right\} \right\}$

- **Determine α with bounding condition c[∞]==0 to yield Eq. 2.18**

(* alph=Solve[Limit[generalSol[z],z→∞]==0,α]
    Solve::"tdep": "The equations appear to involve the variables to be solved for in an non-algebraic way." *)

(*alph=Solve[Limit[generalSol[z],z→∞,Assumptions→(m>0)]==0,α]
    Solve::"ifun": "Inverse functions are being used by Solve"*)

```
In[7]:= alphM2 = Solve[Limit[generalSol[z], z → ∞] == 0 /. m → 2, α]
```

$Out[7]= \ \left\{ \left\{ \alpha \to \frac{\pi^2}{4} \right\} \right\}$

In[8]:= **alphM3 = Solve[Limit[generalSol[z], z → ∞] == 0 /. m → 3, α]**

      Solve::ifun : Inverse functions are being used by Solve, so some
         solutions may not be found; use Reduce for complete solution information. More…

Out[8]= $\left\{\left\{\alpha \to \dfrac{8\,\pi^3}{81\,\sqrt{3}}\right\}\right\}$

In[9]:= **alphM4 = Solve[Limit[generalSol[z], z → ∞] == 0 /. m → 4, α]**

      Solve::ifun : Inverse functions are being used by Solve, so some
         solutions may not be found; use Reduce for complete solution information. More…

Out[9]= $\left\{\left\{\alpha \to \dfrac{\pi^4}{64}\right\}\right\}$

■ **Solve Eq. 2.10 with subtitution** $y = c'$ **and boundary condition** $c'[0] = -1$

In[10]:= **solY = c″[z] == $-\dfrac{m\,z^{-1+m}\,\alpha}{(1+z^m\,\alpha)}$ c′[z] /. {c' → y, c'' → y′}**

Out[10]= $y'[z] == -\dfrac{m\,z^{-1+m}\,\alpha\,y[z]}{1+z^m\,\alpha}$

In[11]:= **solYSep = $\int \dfrac{1}{y[z]}\, ⅆy[z] == -\int \dfrac{m\,z^{-1+m}\,\alpha}{(1+z^m\,\alpha)}\, ⅆz + Log[c2]$**
        (∗ c2 is the overall integration constant ∗)

Out[11]= $\text{Log}[y[z]] == \text{Log}[c2] - \text{Log}[1 + z^m\,\alpha]$

In[12]:= **solYSep = Solve[solYSep, y[z]]**

Out[12]= $\left\{\left\{y[z] \to \dfrac{c2}{1+z^m\,\alpha}\right\}\right\}$

In[13]:= **solC2 = Simplify[Solve[y[z] == -1 /. {First[solYSep]}, c2] /. z → 0, m > 0]**

Out[13]= $\{\{c2 \to -1\}\}$

■ **Find** $c[z] = \int y\, ⅆz$ **with the boundary condition** $c[0] = 1$ **yields:**
  $c[z] = \int y\, ⅆz = 1 - \int_0^z \dfrac{1}{1+\alpha\,z^m}\, ⅆz$

In[14]:= **DSolve[D[c[z], z] == y[z] /. First[solYSep], c[z], z]**
        (∗ y=c′ is the same as c[z]=∫y ⅆz and gives integration constant c[1] ∗)

Out[14]= $\left\{\left\{c[z] \to C[1] + c2\,z\,\text{Hypergeometric2F1}\left[\dfrac{1}{m},\,1,\,1+\dfrac{1}{m},\,-z^m\,\alpha\right]\right\}\right\}$

In[15]:= **solConc = DSolve[{D[c[z], z] == y[z] /. First[solYSep], c[0] == 1}, c[z], z]**

Out[15]= $\left\{\left\{c[z] \to 1 + c2\,z\,\text{Hypergeometric2F1}\left[\dfrac{1}{m},\,1,\,1+\dfrac{1}{m},\,-z^m\,\alpha\right]\right\}\right\}$

In[16]:= **solConc /. m → {2, 3, 4}**

Out[16]= $\left\{\left\{c[z] \rightarrow \left\{1 + \dfrac{c2\ \text{ArcTan}\left[z\ \sqrt{\alpha}\right]}{\sqrt{\alpha}}, 1 + c2\ z\ \text{Hypergeometric2F1}\left[\dfrac{1}{3}, 1, \dfrac{4}{3}, -z^3\ \alpha\right], \right.\right.\right.$

$\left.\left.\left. 1 + c2\ z\ \text{Hypergeometric2F1}\left[\dfrac{1}{4}, 1, \dfrac{5}{4}, -z^4\ \alpha\right]\right\}\right\}\right\}$

■ **The boundary condition** $c[\infty] = 0$ **leads to** $\alpha = \left(\dfrac{\pi}{m\ \text{Sin}[\pi/m]}\right)^m$ **with** $m \in \mathbb{N} > 1$.

In[17]:= $\alpha = \left(\text{Integrate}\left[\dfrac{1}{1 + zS^m}, \{zS, 0, \infty\}, \text{Assumptions} \rightarrow m > 1\right]\right)\ \wedge m$

Out[17]= $\pi^m \left(\dfrac{\text{Csc}\left[\frac{\pi}{m}\right]}{m}\right)^m$

In[18]:= **α /. m → {2, 3, 4}**

Out[18]= $\left\{\dfrac{\pi^2}{4}, \dfrac{8\ \pi^3}{81\ \sqrt{3}}, \dfrac{\pi^4}{64}\right\}$

In[19]:= **N[%]**

Out[19]= {2.4674, 1.76805, 1.52202}

In[20]:= **Limit[generalSol[z], z → ∞, Assumptions → m > 1]**

Out[20]= $\left\{\text{Limit}\left[1 - z\ \text{Hypergeometric2F1}\left[\dfrac{1}{m}, 1, 1 + \dfrac{1}{m}, -\pi^m\ z^m\left(\dfrac{\text{Csc}\left[\frac{\pi}{m}\right]}{m}\right)^m\right],\right.\right.$

$\left.\left. z \rightarrow \infty, \text{Assumptions} \rightarrow m > 1\right]\right\}$

In[21]:= **Limit[generalSol[z], z → ∞] /.**
        m → {2, 3, 4, 5, 90, 100, 170, 200, 2.1}(* Should be zero!*)

Out[21]= {{0, 0, 0, 0, 0, 1, 0, 1, -0.272565}}

■ **Test if solution is solution to stationary case of Eq. 2.10**

In[22]:= **DSolve[{eq10 ⩵ 0 /. m → 2, c[0] ⩵ 1, D[c[z], z] ⩵ -1 /. z → 0}, c[z], z] // Simplify**

Out[22]= $\left\{\left\{c[z] \rightarrow 1 - \dfrac{2\ \text{ArcTan}\left[\frac{\pi z}{2}\right]}{\pi}\right\}\right\}$

In[23]:= **c[z] /. DSolve[{eq10 ⩵ 0 /. m → 3, c[0] ⩵ 1, D[c[z], z] ⩵ -1 /. z → 0}, c[z], z] //**
        Simplify

Out[23]= $\left\{\dfrac{3\ \pi + 6\ \text{ArcTan}\left[\frac{1}{\sqrt{3}} - \frac{4\ \pi z}{9}\right] - 2\ \sqrt{3}\ \text{Log}\left[9 + 2\ \sqrt{3}\ \pi z\right] + \sqrt{3}\ \text{Log}\left[81 - 18\ \sqrt{3}\ \pi z + 12\ \pi^2\ z^2\right]}{4\ \pi}\right\}$

In[24]:= **c[z] /. DSolve[{eq10 ⩵ 0 /. m → 3, c[0] ⩵ 1, D[c[z], z] ⩵ -1 /. z → 0}, c[z], z] // N //**
        FullSimplify

Out[24]= {1.40806 + 0.477465 ArcTan[0.57735 - 1.39626 z] -
        0.275664 Log[9. + 10.8828 z] + 0.137832 Log[0.683918 + z (-0.826993 + 1. z)]}

In[25]:= `c[z] /. DSolve[{eq10 == 0 /. m → 4, c[0] == 1, D[c[z], z] == -1 /. z → 0}, c[z], z] //`
        `Simplify`

Out[25]= $\left\{ \dfrac{2\pi + 2\,\mathrm{ArcTan}[1 - \frac{\pi z}{2}] - 2\,\mathrm{ArcTan}[1 + \frac{\pi z}{2}] + \mathrm{Log}[8 - 4\pi z + \pi^2 z^2] - \mathrm{Log}[8 + 4\pi z + \pi^2 z^2]}{2\pi} \right\}$

In[26]:= `c[z] /. DSolve[{eq10 == 0 /. m → 4, c[0] == 1, D[c[z], z] == -1 /. z → 0}, c[z], z] // N //`
        `FullSimplify`

Out[26]= {1. + 0.31831 ArcTan[1. - 1.5708 z] -
      0.31831 ArcTan[1. + 1.5708 z] + 0.159155 Log[0.810569 + z (-1.27324 + 1. z)] -
      0.159155 Log[0.810569 + z (1.27324 + 1. z)]}

In[27]:= `eq10`

Out[27]= $m\,\pi^m\,z^{-1+m}\left(\dfrac{\mathrm{Csc}[\frac{\pi}{m}]}{m}\right)^m c'[z] + \left(1 + \pi^m z^m \left(\dfrac{\mathrm{Csc}[\frac{\pi}{m}]}{m}\right)^m\right) c''[z]$

In[28]:= `Clear[c]; c[z_] = generalSol[z]`

Out[28]= $\left\{ 1 - z\,\mathrm{Hypergeometric2F1}\!\left[\dfrac{1}{m}, 1, 1 + \dfrac{1}{m}, -\pi^m z^m \left(\dfrac{\mathrm{Csc}[\frac{\pi}{m}]}{m}\right)^m\right]\right\}$

In[29]:= `c[z] /. m → {2, 3, 4}`

Out[29]= $\left\{\left\{1 - \dfrac{2\,\mathrm{ArcTan}[\frac{\pi z}{2}]}{\pi}, \; 1 - z\,\mathrm{Hypergeometric2F1}\!\left[\dfrac{1}{3}, 1, \dfrac{4}{3}, -\dfrac{8\pi^3 z^3}{81\sqrt{3}}\right],\right.\right.$
      $\left.\left.1 - z\,\mathrm{Hypergeometric2F1}\!\left[\dfrac{1}{4}, 1, \dfrac{5}{4}, -\dfrac{1}{64}\pi^4 z^4\right]\right\}\right\}$

In[30]:= `eq10  (* should be always ZERO *)`

Out[30]= {0}

In[31]:= `D[c[z], z] /. m → {2, 3, 4}`

Out[31]= $\left\{\left\{-\dfrac{1}{1 + \frac{\pi^2 z^2}{4}}, \; -\dfrac{1}{1 + \frac{8\pi^3 z^3}{81\sqrt{3}}}, \; -\dfrac{1}{1 + \frac{\pi^4 z^4}{64}}\right\}\right\}$

In[32]:= `D[D[c[z], z], z] /. m → {2, 3, 4}`

Out[32]= $\left\{\left\{\dfrac{\pi^2 z}{2\left(1 + \frac{\pi^2 z^2}{4}\right)^2}, \; \dfrac{8\pi^3 z^2}{27\sqrt{3}\left(1 + \frac{8\pi^3 z^3}{81\sqrt{3}}\right)^2}, \; \dfrac{\pi^4 z^3}{16\left(1 + \frac{\pi^4 z^4}{64}\right)^2}\right\}\right\}$

- **postition of the boundary-layer thickness blt z_* ; c[1]**

In[33]:= `c[1] /. m → {2, 3, 4} // N`

Out[33]= {{0.360907, 0.234962, 0.174894}}

Appendix C

Software Tools

C.1 Data Acquisition with Heurisko Software

The image processing software Heurisko®5.3 distributed by Aeon-Verlag, Hanau, did the data acquisition controlling directly the CCD-camera. In a script the steps of acquisition were declared writing compressed png-files for integer images, raw-files for the sequences and tiff-files for a series of mean lines.

In another instance it automated also the synchronised data acquisition from the different sensors and devices and controlled a power supply.

C.2 Retrieving Oxygen Probe Data

The software delivered by WTW® with their oxygen probe wrote the gathered information in a log file and could export it after the measurement manually to an ASCII-file. It delivered also additional temperature information from the same sensor and added the date in a chosen format.

The graphical user interface was not very comfortable to handle. And sometimes it collected only zeros instead of the concentrations what turned to be unusable some important measurement days. The update to a new software version was not successful.

C.3 Evaluation Scripting in MatLab Language

The evaluation was done entirely with MatLab®7.2 R2006a software. The script was compatible with the version 7.1 but not with 6.5. It was tried to keep the number of used additional toolboxes small. The only additional commercial toolbox was the optimization toolbox from MathWorks that did the non-linear least square fitting.

Also all plots of data in this thesis were done with this software exporting them to eps-files with the `print` command after setting the correct figure size and fonts.

C.4   Type-Setting

LaTeX is a standard type-setting environment based on TeX for writing text projects with mathematical formulas and creating automated reference lists using BibTeX. The style of the bibliography was `natbib.sty` that was adapted to display the last names first of the references in the list and to set the names in small capitals. The parsing of the type-setting code was executed by `pdftex` that included directly the hyperrefs and bookmarks in the pdf-file and handled the bitmap pictures in jpeg- and png-format as desired.

For editing the free software TeXnicCenter for MS-Windows was used that made writing more comfortable due to its high-lighting ability and a button for the different compilation steps. Another appreciated feature was the project handling with the organisation of all related files.

GhostScript did the conversion of eps-files to pdf-graphics with the dos command `epstopdf.exe`. This command was called directly from MatLab with the command `system`.

All code is freely available from the author writing to:

Achim[at]Falkenroths.de.

List of Figures

Index

Bibliography

ANDERSON, S.; SEDDON, K. R.: -. *J.Chem.Res.*, page 74, 1979.

ANDERSON, S.; CONSTABLE, E. C.; SEDDON, K. R.; TURP, J. E.: Preparation and characterisation of 2,2'-bipyridine-4,4'-disulphonic and -5-sulphonic acids and their ruthenium(II) complexes. *J.Chem.Soc.Dalton Trans*, pages 2247–2261, 1985.

ASHER, W. E.; PANKOW, J. F.: Direct observation of concentration fluctuations close to a gas-liquid interface. *Chemical Engineering Science*, 44:1451–1455, 1989.

ATMANE, M. A.; GEORGE, J.: Gas transfer across a zero-shear surface: a local approach. In SALTZMAN, E.; DONELAN, M.; DRENNAN, W.; WANNINKHOF, R., editors: *Gas Transfer at Water Surfaces*, volume 127 of *Geophysical Monograph*. American Geophysical Union, 2001.

BANNER, M. L.; PEIRSON, W. L.: Tangential stress beneath wind-driven airwater interfaces. *J.Fluid Mech.*, 364:115–145, 1998.

BARLOW, C. H.; RORVIK, D. A.; JEFFREY, J. K.: Imaging epicardial oxygen. *Annals of Biomedical Engineering*, 26(1):76–85, 1998.

BRUMLEY, B.; JIRKA, G. H.: Near-surface turbulence in a grid-stirred tank. *Journal of Fluid Mechanics*, 183:235–263, 1987. ISSN 0022-1120.

BRUTSAERT, W.; JIRKA, G. H.: *Gas transfer at water surfaces.* Reidel, 1984.

CASTELLANO, F. N.; LAKOWICZ, J. R.: A water-soluble luminescence oxygen sensor. *Photochemistry and Photobiology*, 67(2):179–183, 1998.

CLARK, L. C.: Monitor and control of blood and tissue oxygenation. *Tr.Am.Soc.Artif.Intern.Org.*, 2:41–45, 1956.

COANTIC, M.: A model of gas transfer across air–water interfaces with capillary waves. *Journal of Geophysical Research*, 91:3925–3943, 1986.

COLEMAN, T. F.; LI, Y.: On the convergence of reflective newton methods for large-scale nonlinear minimization subject to bounds. *Mathematical Programming*, 67(2):189–224, 1994.

COLEMAN, T. F.; LI, Y.: An interior, trust region approach for nonlinear minimization subject to bounds. *SIAM Journal on Optimization*, 6:418–445, 1996.

Csanady, G. T.: The role of breaking wavelets in air-sea gas transfer. *Journal of Geophysical Research*, 95(C1):749–759, 1990.

Danckwerts, P. V.: Significance of a liquid-film coefficients in gas absorption. *Industrial and Engineering Chemistry*, 43:1460–1467, 1951.

Danckwerts, P. V.: *Gas-liquid reactions.* MacGraw-Hill, New York, 1970.

Davies, J. T.: *Turbulence Phenomena. An Introduction to the Elderly Transfer of Momentum, Mass, and Heat, Particularly at Interfaces.* Academic Press, New York; London, 1972.

Degreif, K.: *Untersuchungen zum Gasaustausch - Entwicklung und Applikation eines zeitlich aufgelösten Massenbilanzverfahrens.* PhD thesis, University of Heidelberg, 2006. http://www.ub.uni-heidelberg.de/archiv/6120.

Duke, S. R.; Hanratty, T. J.: Measurements of the concentration field resulting from oxygen absorption at a wavy air–water interface. In Jähne, B.; Monahan, E. C., editors: *Air-water Gas Transfer, Selected Papers from the Third International Symposium on Air-Water Gas Transfer*, Hanau, 1995.

Evans, D. F.: Perturbations on single–triplet transitions of aromatic molecules by oxygen under pressure. *Journal of Chemical Society*, pages 1351–1357, 1957.

Fahlenkamp, H.: *Zum Mechanismus des Stofftransports im laminar-welligen Rieselfilm.* PhD thesis, Technical University of Achen, 1979.

Falkenroth, A.; Degreif, K.; Jähne, B.: Visualisation of oxygen concentration fields in the mass boundary layer by fluorescence quenching. In Garbe, C. S.; Handler, R. A.; Jähne, B., editors: *Transport at the Air Sea Interface - Measurements, Models and Parameterizations.* Springer Verlag, 2007. http://www.springer.com/dal/home/generic/search/results?SGWID=1-40109-22-173670401-0.

Frew, N. M.: The role of organic films in air-sea gas exchange. In Liss, P. S.; Duce, R. A., editors: *The Sea Surface and Global Change*, chapter 5, pages 121–171. Cambridge University Press, Cambridge,UK, 1997.

Frew, N. M.; Bock, E. J.; McGillis, W. R.; Karachintsev, A. V.; Hara, T.; Münsterer, T.; Jähne, B.: Variation of air–water gas transfer with wind stress and surface viscoelasticity. In Jähne, e.; Monahan, E. C., editors: *Air-water Gas Transfer, Selected Papers from the Third International Symposium on Air-Water Gas Transfer*, Hanau, 1995.

Frew, N. M.; Goldman, J. C.; Denett, M. R.; Johnson, A. S.: Impact of phytoplankton-generated surfactants on air-sea gas-exchange. *Journal of Geophysical Research*, 95(C3):3337–3352, 1990.

Garbe, C. S.; Degreif, K.; Jähne, B.: Estimating the viscous shear stress at the water surface from active thermography. In Garbe, C. S.; Handler, R. A.; Jähne, B., editors: *Transport at the Air Sea Interface - Measurements, Models and Parameterizations.* Springer Verlag, 2007.

GULLIVER, J. S.: Introduction to air–water mass transfer. In WILHELMS, S. C.; GULLIVER, J. S., editors: *Air-Water Mass Transfer, selected papers from the 2nd International Symposium on Gas Transfer at Water Surfaces*, 1991.

HARRIOTT, P.: A random eddy modification of the penetration theory. *Chemical Engineering Science*, 17:149–154, 1962.

HERLINA: *Gas Transfer at the Air–Water Interface in a Turbulent Flow Environment.* PhD thesis, University of Karlsruhe, 2005. `http://www.uvka.de/univerlag/volltexte/2005/71/`.

HERLINA; JIRKA, G. H.: Application of LIF to inverstigate gas transfer near the air–water interface in a grid-stirred tank. *Experiments in Fluids*, 37:341–348, 2004.

HERLINA; JIRKA, G. H.: Turbulent gas flux measurements near the air–water interface in a grid-stirred tank. In GARBE, C. S.; HANDLER, R. A.; JÄHNE, B., editors: *Transport at the Air Sea Interface - Measurements, Models and Parameterizations.* Springer Verlag, 2007.

HIBY, J. W.: Eine Fluoreszenzmethode zur Untersuchung des Transportmechanismus bei der Gasabsorption im Rieselfilm. *Wärme- und Stoffübertr.*, 1:105–116, 1968.

HIBY, J. W.: The chemical indicator: a tool for the investigation of concentration fields in liquid. *Ann.N.Y.Acad.Sci.*, 404:348–349, 1983.

HIBY, J. W.; BRAUN, D.; EICKEL, K. H.: Eine Fluoreszenzmethode zur Untersuchung des Stoffübergangs bei der Gasabsorption im Rieselfilm. *Chemie-Ing.-Techn.*, 39:297–301, 1967.

HIGBIE, R.: The rate of absorption of a pure gas into a still liquid during short periods of exposure. *Trans.AIChE*, 31:365–389, 1935.

HO, D. T.; LAW, C. S.; SMITH, M. J.; SCHLOSSER, P.; HARVILLE, M.; HILL, P.: Measurements of air-sea gas exchange at high wind speeds in the southern ocean: Implications for global parameterizations. *Geophysical Research Letters*, 33:16611–16616, August 2006a.

HO, D. T.; SCHLOSSER, P.; HOUGHTON, R. W.; CAPLOW, T.: Comparison of SF$_6$ and fluorescein as tracers for measuring transport processes in a large tidal river. *Journal of Environmental Engineering*, 132(12):1664–1668, Decembre 2006b.

IPCC: *Climate Change 2001: The Scientific Basis. Contribution of Working Group I to the Third Assessment Report of the Intergovernmental Panel on Climate Change.* Cambridge University Press, 2001. `http://www.ipcc.ch`.

IPCC. Climate change 2007: The physical science basis. contribution of working group I to the fourth assessment report of the intergovernmental panel on climate change, 2007. `http://ipcc-wg1.ucar.edu/`.

IUPAC: *IUPAC Compendium of Chemical Terminology*. Blackwell Science, 2. edition, 1997. http://www.iupac.org/publications/compendium/index.html.

Jähne, B.: *Parametrisierung des Gasaustausches mit Hilfe von Laborexperimenten*. PhD thesis, Institut für Umweltphysik, University of Heidelberg, 1980.

Jähne, B.: Transfer processes across the free water surface. Habilitation thesis, University of Heidelberg, Heidelberg, Germany, 1985.

Jähne, B.: From mean fluxes to a detailed experimental investigation of the gas transfer process. In Wilhelms, S. C.; Gulliver, J. S., editors: *Air-Water Mass Transfer, selected papers from the 2nd International Symposium on Gas Transfer at Water Surfaces*, Minneapolis, MN, 1991. ASCE.

Jähne, B.: *Digital Image Processing*. Springer, Berlin, Germany, 6th edition, 2005.

Jähne, B.; Haussecker, H.: Air–water gas exchange. *Annual Reviews Fluid Mechanics*, 30:443–468, 1998.

Jähne, B.; Libner, P.; Fischer, R.; Billen, T.; Plate, E. J.: Investigating the transfer process across the free aqueous boundary layer by the controlled flux method. *Tellus*, 41B(2):177–195, 1989.

Jähne, B.; Popp, C.; Schimpf, U.; Garbe, C. S.: Analysis of the heat transfer process across the aqueous heat boundary layer by active thermography: Mean transfer velocities and intermittence. In Garbe, C. S.; Handler, R. A.; Jähne, B., editors: *Transport at the Air Sea Interface - Measurements, Models and Parameterizations*. Springer Verlag, 2007.

Kautsky, H.: Quenching of luminescence by oxygen. *Trans.Garaday Soc.*, 35: 216–219, 1939.

Kawaoka, K.; Khan, A. U.; Kearns, D. R.: Role of singlet excited states of molecular oxygen in the quenching of organic triplet states. *Journal of Chemical Physics*, 46(5):1842–1853, 1967.

Kearns, D. R.; Stone, A. J.: Excited-state intermolecular interactions involving paramagnetic molecules. *Journal of Chemical Physics*, 55(7):3383–3389, 1971.

Keeling, R. F.; Piper, S. C.; Heimann, M.: Global and hemispheric CO_2 sinks deduced from measurements of the atmospheric oxygen concentration. *Nature*, 1996.

Keeling, R. F.; Stephens, B. B.; Najjar, R. G.; Doney, S. C.; Archer, D.; Heimann, M.: Seasonal variations in the atmospheric O_2/N_2 ratio in relation to the kinetics of air–sea gas exchange. *Global Biogeochemical Cycles*, 12(1):141–163, 1998.

KRAKAUER, N. Y.; RANDERSON, J. T.; PRIMEAU, F. W.; GRUBER, N.; MENEMENLIS, D.: Carbon isotope evidence for the latitudinal distribution and wind speed dependence of the air-sea gas transfer velocity. *Tellus Series B-Chemical and Physical Meteorology*, 58(5):390–417, 2006.

KRAUSE, R. A.: Synthesis of ruthenium(II) complexes of aromatic chelating hererocycles: Towards the design of luminescent compounds. In *Structure and Bonding*, volume 67. Springer-Verlag, 1987.

LAKOWICZ, J. R.: *Principles of Fluorescence Spectroscopy*. Springer, 3. edition, 2006.

LEE, M.; SCHLADOW, S. G.: Visualization of oxygen concentration in water bodies using a fluorescence technique. *Water Research*, 34(10):2842–2845, 2000. `http://edl.engr.ucdavis.edu/Publications/Journals/Lee%20and%20Schladow/Lee_and_Schladow.pdf`.

LEWIS, W. K.; WHITMAN, W. G.: Principles of gas absorption. *Industrial and Engineering Chemistry*, 16:1215–1220, 1924.

MAGNAUDET, J.; CALMET, I.: Turbulent mass transfer through a flat shear-free surface. *J.Fluid Mech.*, 553:155–185, 2006.

MANNING, A. C.: *Temporal variability of atmospheric oxygen from both continuous measurements and a flask sampling network: Tools for studying the global carbon cycle.* PhD thesis, University of California, San Diego, La Jolla, 2001.

MAYER, H. J.: Entwicklung einer laserinduzierten fluoreszenz-technik zum messen von konzentrationsprofilen u. diffusionskonstanten. Master's thesis, University of Heidelberg, 1995.

McGILLIS, W. R.; EDSON, J. B.; HARE, J. E.; FAIRALL, C. W.: Direct covariance air-sea CO_2 fluxes. *Journal of Geophysical Research*, 106(C8):16729–16745, 2001.

MÜNSTERER, T.: *LIF Investigation of the Mechanisms Controlling Air–Water Mass Transfer at a Free Interface.* PhD thesis, University of Heidelberg, 1996. `http://klimt.iwr.uni-heidelberg.de/Literatur/1996/muensterer_PHD1996.pdf`.

MÜNSTERER, T.; MAYER, H. J.; JÄHNE, B.: Dual-tracer measurements of concentration profilesin the aqueous mass boundary layer. In JÄHNE, B.; MONAHAN, E. C., editors: *Air-water Gas Transfer, Selected Papers from the Third International Symposium on Air–Water Gas Transfer*, Hanau, 1995. Aeon.

MÜNSTERER, T.; JÄHNE, B.: LIF measurements of concentration profiles in the aqueous mass boundary layer. *Experiments in Fluids*, 25:190–196, 1997.

NAEGLER, T.; CIAIS, P.; RODGERS, K.; LEVIN, I.: Excess radiocarbon constraints on air-sea gas exchange and the uptake of CO_2 by the oceans. *Geophysical Research Letters*, 33(11), 2006.

Nagaosa, R.: Direct numerical simulation of vortex structures and turbulent scalar transfer across a free surface in a fully developed turbulence. *Phys.Fluids*, 11(6):1581–1595, 1999.

Narayanaswamy, R.; Wolfbeis, O. S.: *Optical Sensors: Industrial, Environmental and Diagnostic Applications*. Springer, 2004. `http://books.google.de/books?id=MmPy9p2CbxgC`.

Nightingale, P. D.; Malin, G.; Law, C. S.; Watson, A. J.; Liss, P. S.; Liddicoat, M. I.; Boutin, J.; Upstill-Goddard, R. C.: In situ evaluation of air-sea gas exchange parameterization using novel conservation and volatile tracers. *Global Biogeochemical Cycles*, 14:373–387, 2000.

Rabilloud, T.; Strub, J.-M.; Luche, S.; van Dorsselaer, A.; Lunardi, J.: A comparison between Sypro Ruby and ruthenium II tris (bathophenanthroline disulfonate) as fluorescent stains for protein detection in gels. *Proteomics*, 1: 699–704, 2001.

Rose, D.; Wilkinson, G.: The blue solutions of ruthenium(II) chloride: a cluster anion. *Journal of the Chemical Society A*, pages 1791–1795, 1970. `http://www.rsc.org/Publishing/Journals/J1/article.asp?doi=J19700001791`.

Schladow, S. G.; Lee, M.; Hurzeler, B. E.; Kelly, P. B.: Oxygen transfer across the air-water interface by natural convection in lakes. *Limnology and Oceanography*, 47(5):1394, 2002. ISSN 0024-3590.

Schlenk, W.. (1879 – 1943), schlenk flasks tubes are used as reaction vessels in air sensitive chemistry. `http://de.wikipedia.org/wiki/Schlenktechnik`.

Schröder, C. R.: *Luminescent Planar Single and Dual Optodes for Time-Resolved Imaging of pH, pCO$_2$ and pO$_2$ in Marine Systems*. PhD thesis, University of Regensburg, 2006. `http://www.opus-bayern.de/uni-regensburg/volltexte/2006/719/`.

Schröder, C. R.; Polerecky, L.; Klimant, I.: Time-resolved pH/pO$_2$ mapping with luminescent hybrid sensors. *Analytical Chemistry*, 79(1):60–70, 2007.

Siegenthaler, U.; Sarmiento, J. L.: Atmospheric carbon dioxide and the ocean. *Nature*, 365:119–125, 1993.

SOLAS. Source of Fig. 1.3: US-SOLAS science implementation strategy.

Stern, O.; Volmer, M.: Über die Abklingungszeit der Fluoreszenz. *Phys.Z*, 20: 183–188, 1919.

Takahashi, T.; Sutherland, S. C.; Sweeny, C.; Poisson, A.; Metzl, N.; Tilbrook, B.; Bates, N.; Wanninkhof, R.; Feely, R. A.; Sabine, C.; Olafsson, J.; Nojiri, Y.: Global sea-air CO$_2$ flux based on climatological surface ocean pCO$_2$ and seasonal biological and temperature effects. *Deep-Sea Research II*, 49:1601–1622, 2002. `http://www.ldeo.columbia.edu/res/pi/CO2/carbondioxide/pages/air_sea_flux_rev1.html`.

TAKEHARA, K.; ETOH, G. T.: A direct visualization method of CO_2 gas transfer at water surface driven by wind waves. In DONELAN, M. A.; DRENNAN, W. M.; SALTZMAN, E. S.; WANNINKHOF, R., editors: *Gas Transfer at Water Surfaces*, Geophysical Monograph, 2002.

VARIANO, E.; COWEN, E. A.: Quantitative imaging of CO_2 transfer at an unsheared free surface. In GARBE, C. S.; HANDLER, R. A.; JÄHNE, B., editors: *Transport at the Air Sea Interface - Measurements, Models and Parameterizations*. Springer Verlag, 2007.

VAUGHAN, W. M.; WEBER, G.: Oxygen quenching of pyrenebutyric acid fluorescence in water. *Biochemistry*, 9:464, 1970.

VOGEL, F.. Visualisierung von Gasaustauschprozessen durch Lumineszenzspektroskopie. Mini research project under the guidance of A. FALKENROTH at the Institute of Environmental Physics, University of Heidelberg, 2004.

VOGEL, F.: Spectroscopic techniques for gas-exchange measurements. Master's thesis, University of Heidelberg, 2006.

WANNINKHOF, R.: Relationship between gas exchange and wind speed over the ocean. *Journal of Geophysical Research*, 97(C5):7373–7382, 1992.

WANNINKHOF, R.: The impact of different gas exchange formulations and wind speed products on global air–sea CO_2 fluxes. In GARBE, C. S.; HANDLER, R. A.; JÄHNE, B., editors: *Transport at the Air Sea Interface – Measurements, Models and Parameterizations*. Springer Verlag, 2007.

WANNINKHOF, R.; MCGILLIS, W. R.: A cubic relationship between gas transfer and wind speed. *Geophysical Research Letters*, 26:1889–1892, 1999.

WOLFF, L. M.; LIU, Z. C.; HANRATTY, T. J.: A fluorescence technique to measure concentration gradients near an interface. In WILHELMS, S. C.; GULLIVER, J. S., editors: *Air-Water Mass Transfer, selected papers from the 2nd Int. Symposium on Gas Transfer at Water Surfaces*, pages 210–218, Minneapolis, 1991. ASCE.

WOODROW, P. T.; DUKE, S. R.: LIF measurements of oxygen concentration gradients along flat and wavy air–water interfaces. In DONELAN, M. A.; DRENNAN, W. M.; SALTZMAN, E. S.; WANNINKHOF, R., editors: *Gas Transfer at Water Surfaces*, volume 127 of *Geophysical Monograph*, pages 83–88, 2002.

ZELELOW, B.; KHALIL, G. E.; PHELAN, G.; CARLSON, B.; GOUTERMAN, M.; CALLIS, J. B.; DALTON, L. R.: Dual luminophor pressure sensitive paint II. Lifetime based measurement of pressure and temperature. *Sens.Actuators, B*, 96:304–314, 2003.

Some references contain links to web pages. They have been checked last in June 2007.

Danksagung (acknowledgements)

Eidesstattliche Erklärung

Hiermit erkläre ich, dass ich die vorliegende Arbeit selbst verfasst habe und mich keiner anderen als der ausdrücklich bezeichneten Quellen und Hilfen bedient habe.

_____ Heidelberg, im Juni 2007
Achim Falkenroth